Channel Modelling and Localisation of Capsule Endoscope Inside the Small Intestine

By

Perzila Ara

A thesis submitted to Macquarie University
for the degree of
Doctor of Philosophy
Department of Engineering, Faculty of science
November 2016

Typeset in LaTeX 2$_\varepsilon$.

Except where acknowledged in the customary manner, the material presented in this thesis is, to the best of my knowledge, original and has not been submitted in whole or part for a degree in any university.

Perzila Ara

To my dearest daughter Parmida

Acknowledgements

I would like to express my sincere gratitude and heartfelt appreciation to my supervisors, Professor Michael Heimlich and Professor Eryk Dutkiewicz for their wonderful support, advice and continuous encouragement throughout my research. This work would not have been completed without their remarkable insight, great knowledge and invaluable guidance.

Additionally, I am extremely thankful for the time and advice from Dr Kegen Yu. His invaluable insight into my research work and his outstanding support has helped me make significant improvements in this dissertation.

I also would like to extend my thanks to Dr Shaokoon Cheng, for his suggestions and support in designing the small intestine model. I am grateful to Dr Keith Imrie for his valuable advice and useful comments that improved the quality of this thesis. I am also thankful to the admirable staff in the Department of Engineering for their wonderful support.

Words would be insufficent to express my deepest appreciation to my mother and father for their endless support, motivation and encouragement through the years that made this possible. I would like to thank my husband for his love and support. Special thanks to my lovely daughter, Parmida, who is the pride and joy of my life. I love you more than anything and I appreciate all your patience and support during mum's PhD studies.

Last but not least, thanks to all my friends for giving me all the support that I needed during my study.

I wish to acknowledge the Australian Research Council for the financial support of this research work and Macquarie University for providing financial support to attend national and international conferences during this project.

List of Publications

Publications related to the field of this thesis are as follows.

1. P. Arab, M. Heimlich and E. Dutkiewicz, "Investigation of radar localization system accuracy for human gastro intestine (GI) tract," *Medical Information and Communication Technology (ISMICT), 2013 7th International Symposium on*, Tokyo, 2013, pp. 144-148.

2. P. Ara, M. Heimlich and E. Dutkiewicz, "Investigation of radar approach for localization of gastro intestinal endoscopic capsule," *2014 IEEE Wireless Communications and Networking Conference (WCNC)*, Istanbul, 2014, pp. 99-104.

3. P. Ara, M. Heimlich and E. Dutkiewicz, "Antenna performance for localization of capsule endoscope," *2014 8th International Symposium on Medical Information and Communication Technology (ISMICT)*, Firenze, 2014, pp. 1-5.

4. P. Ara, S. Cheng, M. Heimlich and E. Dutkiewicz, "Investigation of in-body path loss in different human subjects for localization of capsule endoscope," *2015 37th Annual International Conference of the IEEE Engineering in Medicine and Biology Society (EMBC)*, Milan, 2015, pp. 5461-5464.

5. P. Ara, S. Cheng, M. Heimlich and E. Dutkiewicz, "Sensitivity analysis of human phantom models for accurate in-body path-loss model development," *Personal, Indoor, and Mobile Radio Communications (PIMRC), 2015 IEEE 26th Annual International Symposium on*, Hong Kong, 2015, pp. 1328-1332.

6. P. Ara, S. Cheng, M. Heimlich and E. Dutkiewicz, "Grid sensitivity analysis of human phantom models to minimize the simulation error for capsule endoscope localization," *2015 15th International Symposium on Communications and Information Technologies (ISCIT)*, Nara, 2015, pp. 295-298.

7. P. Ara, E. Dutkiewicz, and M. Heimlich, "In-body Path-loss Model Evaluation for Localization of Capsule Endoscope," *2016 EURASIP Journal on Wireless Communications and Networking*, Submitted.

8. P. Ara, K. Yu, S. Cheng, E. Dutkiewicz, and M. Heimlich, "Derivation of CRLB for Wireless Capsule Endoscope Localization Using Received Signal Strength," *in IEEE Sensors Journal*, 2016, vol.PP, no.99, pp.1-11.

9. S. Movassaghi, P. Arab and M. Abolhasan, "Wireless technologies for Body Area Networks: Characteristics and challenges," *Communications and Information Technologies (ISCIT), 2012 International Symposium on*, Gold Coast, QLD, 2012, pp. 42-47.

Abstract

Capsule endoscopy is a relatively new gastrointestinal imaging procedure which has been used to inspect and diagnose possible abnormalities and diseases inside the human body. However one of the main drawbacks of this new technology is associating the exact location information of the capsule with the received video images to provide a clear idea of the location of any abnormalities.

In this thesis we address different challenges associated with location estimation of a capsule endoscope. First we propose a radar system as a location estimation technique and a Received Signal Strength (RSS) method for capsule localisation. We also develop a new deterministic in-body path-loss model based on the different physical properties of tissues and with several reflections and absorptions by each tissue in the abdomen region. We show that a deterministic path-loss model which is only dependent on a theoretical analysis of radio propagation inside the abdomen area cannot fully ensure the accuracy of the model. A statistical in-body path-loss model is derived based on simulating the electromagnetic wave propagation inside the abdomen region of three distinct human phantom models. Based on the developed path-loss model the 2D location of the capsule is estimated using the trilateration method as well as the Non-linear Least Squares (NLLS) algorithm. It is shown that the probability of achieving a location error of less than 15 mm is about 80% in a condition where the noise standard deviation is less than 8 dB. Moreover, using our developed statistical path-loss model and under three shadowing scenarios, we calculate the mathematical bound on the localisation precision. From the obtained results it can be concluded that a 2.4 GHz RSS-based localisation using a radar system is feasible and can reach centimetre-order precision.

Contents

List of Figures

List of Tables

1 Introduction

1.1 Background

Endoscopy is a medical procedure that has been used to inspect and diagnose possible abnormalities and diseases inside the human body. This technology has been developed for examination of various parts of the body such as the gastrointestinal (GI) tract, uterus, bladder, nose, cervix, etc. Different methods of endoscopy that can be applied for the GI tract are: Gastroscopy and Colonoscopy. Gastroscopy is one of the methods of endoscopy, which is used for the upper gastrointestinal tract such as: esophagus, stomach, and duodenum. Colonoscopy is another method of endoscopy that is used for the colon. The last remaining part of the GI tract is the small intestine, which is not accessible by conventional wired endoscopy methods. In fact the small intestine is the most challenging part of the GI tract for monitoring purposes due to its great length and complicated shape.

An increasing demand to improve diagnostic capabilities in the small intestine has resulted in the development of a new type of endoscopy, known as capsule endoscopy. Capsule endoscopy is a painless and comfortable diagnosis method, which allows patients to go back to their normal life during the procedure without any need to stay at a hospital or health care facility under supervision by a specialist. It has been known as

an inspiring technology for evaluation of suspected diseases such as bleeding, tumour, ulcer or inflammatory bowel disease. One of the greatest advantages of this technology is that the patient is not required to undergo any sedation or air insufflation, which results in no risk of sedation's side effects.

The first swallowable capsule was developed during the 1950s to measure gastrointestinal temperature, pressure and potential hydrogen (PH). After technological development the first Wireless Capsule Endoscope (WCE) was used to acquire images from the small intestine by the Given Imaging company in 1998. The early version of the capsule was able to record for six hours and the size was 11 mm $\times$ 30 mm. In 2001, the Food and Drug Administration (FDA) approved wireless capsule endoscopy as a first technique to evaluate small-intestine diseases [10].

In general a WCE system consists of three main components:

1. Capsule endoscope;

2. A sensing system which is worn and carried by patients and works to receive and record the data;

3. A workstation with proprietary software.

It is normally expected that examination of the small bowel will be finished in 8 hours. However some factors such as slow small-intestine movement, any debris in the distal small bowel or slow emptying of the gastric tract can cause an unfinished procedure. In this situation a longer battery lifetime of the capsule might provide a better visualisation of the intended organ [10].

Although wireless capsule endoscopy is considered as a safe technology, some issues are associated with it. The first and most important risk is retention of the capsule, which happens when a capsule gets stuck and remains in a GI tract for a minimum of two weeks due to tumours, surgical anastomotic constraints, Crohn's disease, compression of the GI tract because of pregnancy, etc. In this situation a patient should under go abdominal radiography to find the exact location of the capsule and an operation should then be performed to take out the capsule. In some studies, the overall retention rate has been reported to be between 1.3% and 1.4% [11, 12].

Another concern of WCE technology is with possible interference that might occur between the transmitted signal from the capsule and other implanted electronic devices such as defibrillators, cardiac pacemakers, and left ventricular assist devices [10]. Although based on some in vivo and in vitro studies, the authors in [13] claimed that there is no interference between these cardiac devices and a capsule. Another study [14]

showed that there is no interference between a capsule endoscope and a pacemaker, but some losses in acquired images were observed where the capsule was located in the close proximity of a pacemaker pulse generator. Moreover, a patient with a WCE should not undergo Magnetic Resonance Imaging (MRI), as it causes serious damage to the abdominal cavity or intestinal tract [13].

Improvements in WCE technology can be achieved by addressing several issues and limitations such as active locomotion, limited working time, high power efficiency, high data rates, high quality of images, remote powering of the capsule and accurate localisation of the capsule.

1.2 Motivation for This Research

Among the different aforementioned limitations of WCE, capsule location is a crucial parameter that needs to be estimated precisely. Associating the exact localisation information of the capsule with the received video images can provide a clear idea about the location of any abnormalities or lesions. It can reduce the time needed for assessing the images and can result in less-invasive surgery. Moreover, in the case of capsule retention, having an exact knowledge of the capsule location prevents patients from undergoing any imaging procedure and protects them against the harmful effects of ionising radiation such as x-ray or computed tomography (CT) scans. However estimating the exact location of a capsule is a challenging task for the following reasons:

1. Modelling of wave propagation inside the human body:
   This is one of the major drawbacks, since performing experiments on the real human body is quite infeasible and the RF signals encounter a high loss and a highly dynamic channel propagation environment while passing through the human body.

2. Modelling the movement of the capsule in the GI tract.

3. The complex, curly tube shape of the small intestine (Figure 1.1) which is approximately 6 m in length [15].

4. Designing a localisation algorithm to achieve real-time location estimation within mm range accuracy.

Up to now, various methods have been investigated for WCE location estimation which will be introduced in detail in Chapter 2. The most in-demand methods

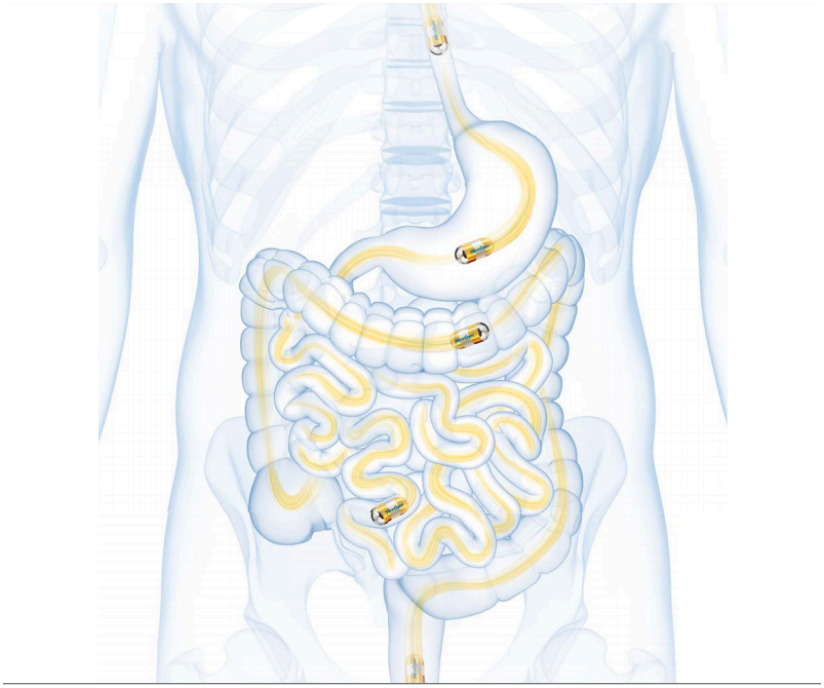

FIGURE 1.1: Small intestine [1]

are magnet-based location estimation, Time of Arrival (TOA) and Received Signal Strength (RSS). The magnetic-based and the TOA-based location estimation methods have received less attention because the first method needs extra hardware which enlarges the size of the capsule and the second method requires precise synchronisation between the transmitter and the receiver. The last method, on the other hand, is more attractive for many researchers due to its low cost and simplicity, even though it provides lower accuracy and is highly dependent on the properties of the propagation medium. In this thesis, details of an RSS-based location estimation method employing a radar system will be presented. We will focus on investigating an RSS-based location estimation method employing a radar system in front of the human abdomen. This requires less hardware complexity since there is no need to consider any extra transmitter/receiver at the capsule side, as the location can be estimated by the reflected signal from the capsule.

1.3 Research Objectives

One of the main drawbacks of applying WCE is accurate determination of the capsule endoscope location inside the small intestine at each instant. This assists us to verify the exact location of any lesions or disorders inside the small intestine and results in more accurate diagnosis procedures and medical treatments. This thesis seeks to remedy the above drawback by proposing a radar system as a technique for location estimation, using an RSS-based method for capsule endoscope localisation. The main focus is to investigate the impact of different abdomen tissue layers on wave propagation inside the body. We also provide a detailed study of a proposed new theoretical and statistical in-body path-loss model. The offered accuracy of the capsule location estimation and the precision of the system are also studied according to the proposed statistical path-loss model. It should be highlighted that this study is not investigating the difficulty in getting the hardware to work other than defining an appropriate antenna configuration. Moreover, It does not address the challenges of actually building the receivers and transmitters circuitry, antenna fabrication, calibration and hour-to-hour patient homeostasis, etc. The aim of this thesis is to serve as a gateway to enhance location estimation of WCE in the future.

1.4 Contribution

Contributions are made in different fields in this thesis, namely:

(i) Defining a suitable working frequency for the radar system to enable us to employ it for on-body to in-body communication (Chapter 4).

(ii) Selecting an optimal transmitter and receiver antenna among the two common electric and magnetic antennas for the radar system. Moreover determining the best position of the antenna on the human abdomen to provide better coverage even in critical parts of the abdomen such as the middle region (Chapter 5).

(iii) Developing a theoretical in-body path-loss model focused on the abdomen region and based on the different dielectric properties of the human tissues and several wave absorptions and reflections by each tissue and each tissue boundary. We confirm that the theoretical path-loss model might not be suitable for some applications such as developing a precise location estimation algorithm. This issue is even more crucial at higher frequency, where a smaller antenna size is used and the object lies closer to the near-field region (Chapter 6).

(iv) Performing a comprehensive sensitivity test analysis on adjusting the best possible voxelling for the human models prior to performing any simulations on them. We then show the significant impact of an accurate voxel setting on overall system performance (Chapter 7).

(v) Developing and implementing a generic small-intestine model which can be embedded inside the abdomen of the human phantom models, since the intestines of the phantom models lack the desired resolution, making it impossible to properly perform different experiments on a capsule endoscope moving inside the small intestine (Chapter 8).

(vi) Proposing a statistical path-loss model for three different anatomical human models. The proposed path-loss model is a good approximation to model in-body RF propagation, since real measurements are quite infeasible for the capsule endoscopy subject (Chapter 8).

(vii) Investigating the achievable location estimation error for the RSS-based localisation method as the capsule endoscope passes through the small intestine. The impact of different noise standard deviations on location error was also studied in detail (Chapter 9).

(viii) Investigating the potential precision limits for RSS-based localisation for the wireless capsule endoscope using the Cramér-Rao Lower Bound (CRLB) method. The theoretical localisation precision limit is studied under three different shadowing scenarios by assuming standard deviation of the shadowing with constant variance, parameter dependent variance or correlated and parameter dependent variance. Analytical formulas are derived for the CRLB for capsule positioning when distance and azimuth angle measurements are employed to estimate the location of the capsule (Chapter 9).

1.5 Thesis Outline

The thesis is organised as follows:

- **Chapter 2:** Background Literature Review

  This chapter presents the physical layout of the WCE. It then provides the necessary background of the most conventional location estimation methods for a

free-space scenario. It aims to provide an insight into the characteristics of commonly used localisation methods and techniques. Then it presents an overview and preliminary study of WCE location estimation in the GI tract, its related challenges and the accuracy provided. The desired outcome of this chapter is a clear comparison between each localisation technique and its suitability for in-body applications. Moreover we will choose a location estimation technique which has never been studied for WCE localisation.

- **Chapter 3:** Literature Review On In-body Path-loss Models

  This chapter presents a brief review of different in-body path-loss models which are proposed mainly for the GI tract, since the accuracy of RF-based localisation techniques depends on the propagation channel characteristic. These path-loss models are carefully categorised based on their development methods. Then a discussion on the challenges and benefits of each model is given in detail.

- **Chapter 4:** Radar Technique for In-body Localisation

  This chapter begins with a brief introduction to and description of 60 GHz milimetre-wave wireless technology due to its growing demand for communication services in this frequency band. Then follows a discussion on whether or not this frequency band can be applied to the radar system to estimate the location of the capsule endoscope. It will then move on to present a discussion on investigating the suitability of UWB and a 2.4 GHz frequency for WCE localisation. At the end of this chapter we will select the most appropriate working frequency from the aforementioned frequencies for the radar system to make it possible to estimate the location of a WCE.

- **Chapter 5:** On-Body Antenna at 2.4 GHz

  This chapter provides background information of different antenna types that can be used for WCE localisation using a radar system. It then presents an investigation of the performance of the two common antenna types (a half-wavelength dipole antenna and a loop antenna) in front of the human abdomen. Furthermore, different polarisations of the half-wavelength dipole antenna are studied to find out the best possible position for the antenna for higher performance. The aforementioned studies assist us to choose and apply the most appropriate antenna for WCE localisation.

- **Chapter 6:** Evaluation of General In-body Path-Loss Model

In this chapter we will propose a new theoretical path-loss model for in-body applications, mainly focused in the abdomen area. The proposed model explains the dependence of the abdomen loss on the different dielectric properties of the human tissues, and on the several wave absorptions and reflections by each tissue and each tissue boundary. This model is further compared with existing electromagnetic simulation models using the Finite-Difference Time-Domain (FDTD) method for performance evaluation as well as a theoretical near-field path-loss model. At the end of this chapter we will explain why a deterministic path-loss model, which is only dependent on a theoretical analysis of radio-wave propagation inside the abdomen area, cannot fully address the accuracy of the model for each capsule location inside the abdomen.

- **Chapter 7:** Sensitivity Test Analysis

  In this chapter we will present a sensitivity test analysis on selecting the best possible voxelling for the human phantom models prior to performing any simulations on them. It provides a detailed analysis of RF signal propagation in the abdomen region of different human phantoms at 2.4 GHz and shows how setting the best possible grid size can affect the accuracy of the loss and distance measurements and improve the overall system performance.

- **Chapter 8:** Statistical Abdomen Path-loss Model for Different Human Subjects

  In this chapter we develop a statistical path-loss model for three different anatomical human models when applying electromagnetic simulations, using the FDTD method at 2.4 GHz. A mathematical expression for the path-loss model is proposed based on the analysis of the measured loss at different capsule locations inside the small intestine. The proposed model explains the dependence of the loss on the radial dictance and the angle of the capsule from the receiver antenna. Furthermore, in order to perform a comprehensive study on the abdomen region and construct a realistic framework, we design a generic small-intestine model to be embedded inside the abdomen cavity of the phantom models.

- **Chapter 9:** Location Estimation of Wireless Capsule Endoscope

  In this chapter the achievable location estimation error and the potential precision limits for RSS-based localisation are investigated for the wireless capsule endoscope as it passes through the small intestine, using the Cramér-Rao Lower Bound (CRLB) method. Moreover the impact of different noise standard deviations on the location error is studied. The results demonstrate that the system

precision greatly depends on the shadowing condition as well as the distance and angle between the capsule and the receiver antennas. We find that, by employing the radar system for location estimation of the WCE and applying the RSS-based method, it is possible to achieve accuracy in the order of centimetres.

- **Chapter 10:** Conclusion and Recommendations for Future Work

  Finally, a conclusion of the thesis and an indication of future research directions will be provided in this last chapter.

2

Background Literature Review

2.1 Introduction

Determining the physical location of a WCE and its received images at each instant of time is crucial in both diagnostic and treatment procedures. However position determination for a WCE is a challenging task because of the complex physical shape of the small intestine, which folds upon itself many times and has an uncontrollable movement inside the abdomen cavity. Positioning is normally conducted in two main steps: (i) the first step is parameter estimation where several measurements are needed to extract the required position-related parameters; (ii) In the second step the acquired parameters in step 1 need to be processed to determine the position of the target. In this chapter, we first introduce the physical layout of common WCEs. To provide the reader with a general picture of the localisation of a mobile node we begin our discussion with an overview of conventional localisation methods and measurement types which have been applied in free-space scenarios. Then we present an overview of capsule-endoscope localisation systems and their related challenges.

2.2 Physical Layout of a Wireless Capsule Endoscope (WCE)

Most wireless capsule endoscopes have common components. The external shell of the capsule is made of biocompatible material, which is resistant to any fluid inside the digestive tract, and with the size of a large antibiotic pill (11 mm in diameter and 26 mm in length). Inside the capsule shell is normally a vision module, wireless communication unit and energy source. The most common components are depicted in Figure 2.1.

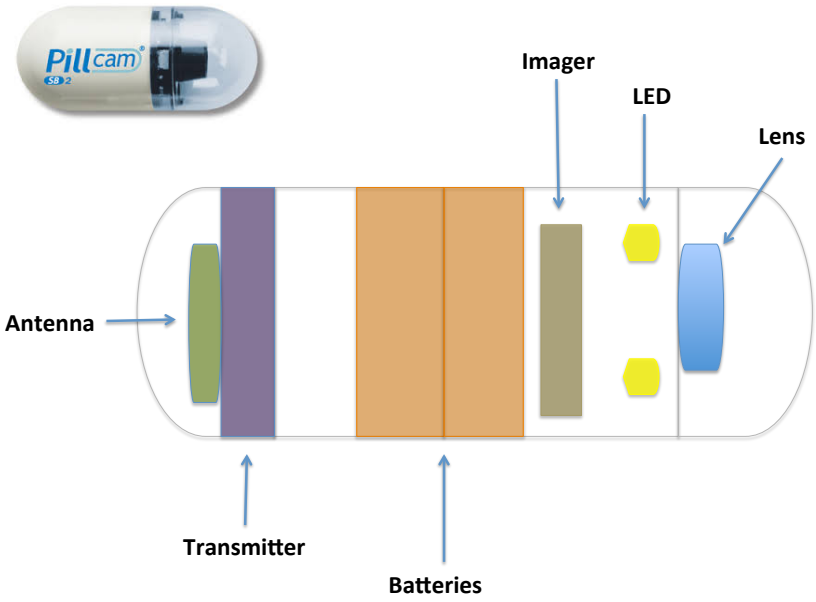

FIGURE 2.1: Diagram of WCE components [2]

The vision module consists of a camera with LED-based illumination and an optical lens which defines the field of view. An RF transmitter and antenna are included in the communication unit. A battery is also used, as the energy source of the WCE [2]. In addition to the aforementioned modules a complete WCE is normally also equipped with three more modules: locomotion, localisation and diagnosis/tissue manipulation tools. However most developed capsules have only some subset of these modules due to space constraints [16].

The capsule is able to take 5000 images during an average eight-hour journey through the gastrointestinal tract with an average movement rate of 1-2 cm in minutes.

The obtained images have normally a magnification of 1:8; with a depth view of 1-30 mm. In general, small objects with a size of the order of 10 mm can be detected by the capsule. The images taken by the capsule are transmitted to the sensors, which are attached to the abdomen, to be saved and recorded. The obtained images can then be downloaded and reviewed by a specialist to investigate any lesion inside the abdomen. Normally the capsules are excreted after 24-28 hours. Nowadays various wireless video capsules are commercially available for different GI-tract applications. They are mainly different in numbers of cameras, battery lifetime, frame rate, purpose of use and image quality. Table 2.1 outlines various WCE specifications, which are mainly focused on small-bowel visualisation [8].

Most of these capsules transmit their data through Radio Frequency (RF) transmission from an integrated antenna inside the capsule to a sensor array which is carried by the patient, except for Microcam and CapsoCam capsules. In the MicroCam capsule, human body communication has been chosen as a method of data transmission. The capsule uses the human body as a conductor to transmit data via an exterior bipolar case to a sensor electrode which is attached to the patient's skin. The benefit of this method compared to RF transmission is that the capsule utilises less power to perform data transmission [17]. On the other hand, CapsoCam capsules are equipped with an EPROM, so they do not transfer any images and store all the data in their EPROM. After the procedure, the patient needs to send the capsule back to a gastroenterology unit for further assessment. Therefore it is not possible to perform real-time visualisation with this type of capsule [18, 19].

Table 2.1: Technical Specification of Various Capsule Endoscopes for Small Bowel [8]

	PillCam		**MicroCam**	**EndoCapsule**		**CapsoCam SV1**	**OMOM Capsule**
	SB2	***SB3***		***EC1***	***EC-S10***		
WCE Company	Given Imaging		Intromedic	Olympus		CapsoVision	Chongqing Jinshan Science & Technology
Length (mm)	26	26	24	26	26	31	28
Diameter (mm)	11	11	11	11	11	11	13
Weight (g)	2.9	1.9	3.4	3.8	3.3	4	<6
No. of Cameras	1	1	1	1	1	4	1
Frame rate (frame/s)	2	2/6	3	2	2	12/20	0.5/1/2
Image Sensor	CMOS	CMOS	CMOS	CCD	CMOS	CMOS	CMOS
Viewing Angle	156°	156°	150°	145°	160°	4*90°	140°
Minimum Recording Time (h)	11	11	11	8	12	15	8±1

2.3 Anatomy of the Small Intestine

Before giving any description of the small intestine anatomy it is necessary to briefly describe the abdomen. The abdomen is the largest cavity in the body, and has an oval shape. The upper extremity of the abdomen is shaped by the diaphragm and the lower extremity is shaped by the bony parts of the pelvis. In general, for convenience of description, the abdomen is artificially classified into 9 regions [20].

1. Epigastric region (epigastrium)
2. Left hypochondrium (LHC)
3. Right hypochondrium (RHC)
4. Umbilical region
5. Left lumbar region
6. Right lumbar region
7. Hypogastric region
8. Right iliac fossa (RIF)
9. Left iliac fossa (LIF)

It should be mentioned that "hypo" refers to "below", "epi" refers to "above", "chond" refers to the cartilage of the rib and "gast" is in reference to the stomach [3]. These regions can be seen in Figure 2.2.

The small intestine or small bowel is one of the organs in the gastrointestinal tract, and is located in the abdomen cavity, lying between the stomach and the large intestine. The main functions of this organ are absorbing nutrients from digested food and moving food along the digestive tract. Anatomically the small bowel can be divided into three parts: duodenum, jejunum and ileum as shown in Figure 2.3.

The duodenum is the widest, shortest and the most fixed part of the small intestine, with a length of about 25 cm. It has a C-shaped structure, which starts from the end of the stomach, wraps around the head of the pancreas and joins to the next part of the small intestine. From the end of the duodenum, the next part of the small intestine, which is called the jejunum, begins. The jejunum has a reddish colour and is wider, thicker and more vascular than the last part of the intestine (ileum). It occupies

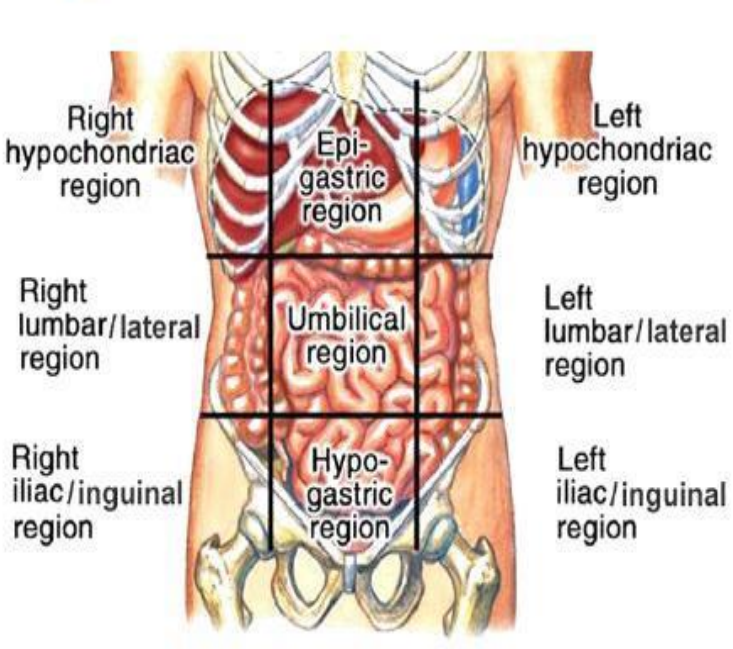

FIGURE 2.2: Regions of the abdominal area [3]

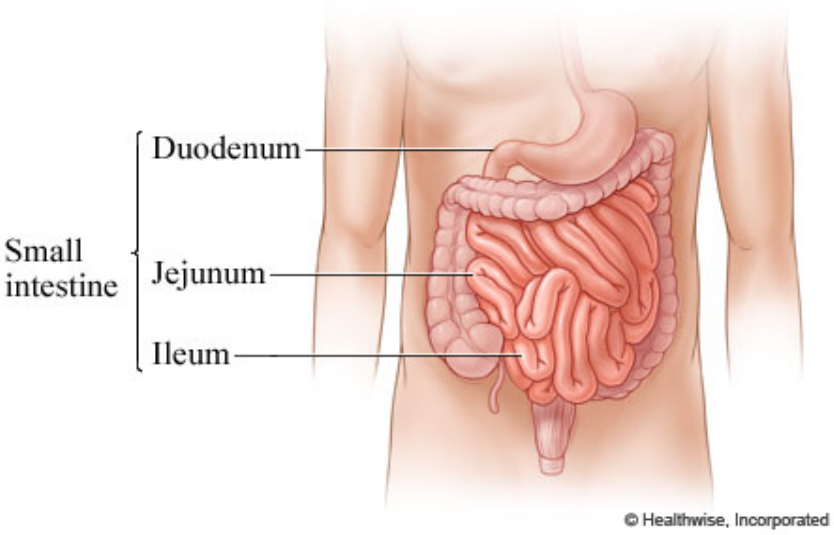

FIGURE 2.3: Anatomical divisions of the small intestine [4]

mainly the umbilical and left iliac regions and is about 2.4 m in length. The last part of the small intestine is the ileum which mainly occupies the central and right lower abdomen and pelvis. It is a narrow tube with a diameter of about 3.75 cm and a length of about 3.6 m, with a pinkish colour. It has a thinner coat and is less vascular than the jejunum. In general there is no morphological line between these three parts, although at the same time the characteristic of the intestine gradually changes from the commencement to the end of each part [20].

2.4 Position Estimation Approaches

Real-time, accurate and reliable position estimation and position-based services and protocols are essential in the future of communication networks. A position system allows a mobile device to discover its position. This makes the position of the device available for a positioning-based system such as tracking, monitoring and navigating purposes. In general the location information of a mobile node can significantly improve the performance of a wireless system, network planning, network adaptation, etc. In point of fact, position estimation of a target node in a wireless network involves a signal exchange between the target and a number of reference nodes. Depending on where the position estimation is happening, we can have two types of positioning as follows [21]:

1. **Self-Positioning:** when the position can be estimated by the target node itself.
2. **Remote-Positioning:** or remote-centric positioning, when the position can be estimated by the central unit that takes the information via the reference nodes.

Furthermore, depending on whether the position estimation is performed directly from the signal travelling between nodes or not, two different position-estimation schemes can be defined as:

1. **Direct-Positioning:** In this scheme the position will be calculated directly from the signals travelling between nodes;
2. **Two-Step Positioning:** In this second scheme some signal parameters will be extracted from the signals and then the position will be estimated according to those parameters.

Although the two mentioned schemes have a quite similar performance with high signal-to-noise ratios (SNRs), the latter scheme has a lower complexity than the direct approach [22]. For this reason, the two-step approach is the technique normally used in

most positioning systems. Figure 2.4 illustrates the principal stages of the two-step positioning method. Each aspect of this flowchart will be discussed in the following sections.

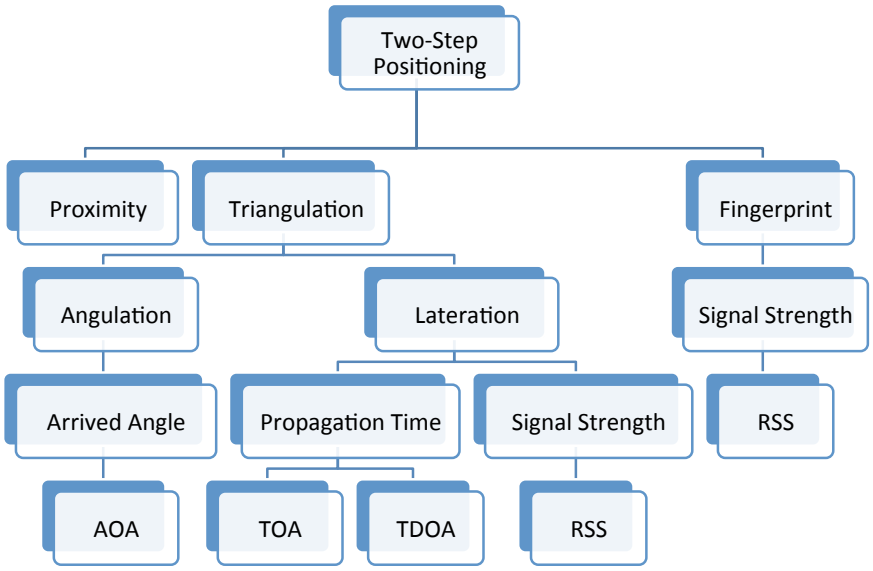

FIGURE 2.4: Stages of Location System

2.5 Estimation of Position-Related Parameter

To estimate the location of a target by a two-step positioning algorithm, some parameters of the signal travelling between the target node and reference nodes should be extracted in the first step. Some of the main signal parameters which are used in the first phase are: Time of Arrival (TOA), Received Signal Strength (RSS) and Angle of Arrival (AOA). These parameters can be employed in a positioning system to obtain information about the target node as shown in Figure 2.4. In some systems a hybrid scheme which includes two or more position parameters is employed to obtain target-related information. In this section, first three traditional techniques of localisation will be introduced, then follows a discussion of the pros and cons of each technique.

2.5.1 Time of Arrival (TOA)

The time of arrival or time of flight (TOF) is a signal parameter that can be extracted by measuring the one-way signal propagation time between a reference node of R_1, R_2 or R_3 and a target node of T. Then the distance can be calculated based on the obtained measured time (Figure 2.5).

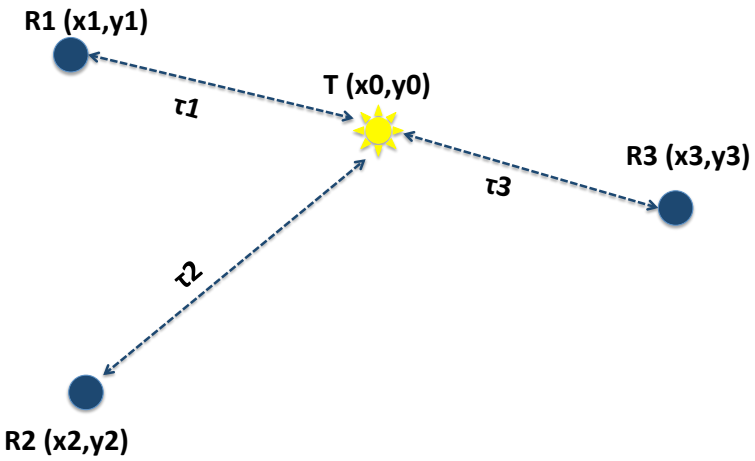

Figure 2.5: Positioning with TOA Technique

To estimate the 2-D location of a target node by the TOA method, assume that three reference nodes are employed in a system to receive the signal at the target (Figure 2.6). The time of flight t_i between the target and each reference node can be applied to compute the distance d_i between them using the following equation:

$$d_i = (t_i - t_0)c \tag{2.1}$$

where t_0 is the actual time at which the target node starts transmission, t_i is the time of flight between the target and the i^{th} reference node and c is the speed of the signal in the medium. To find each coordinate of the target node we can use the

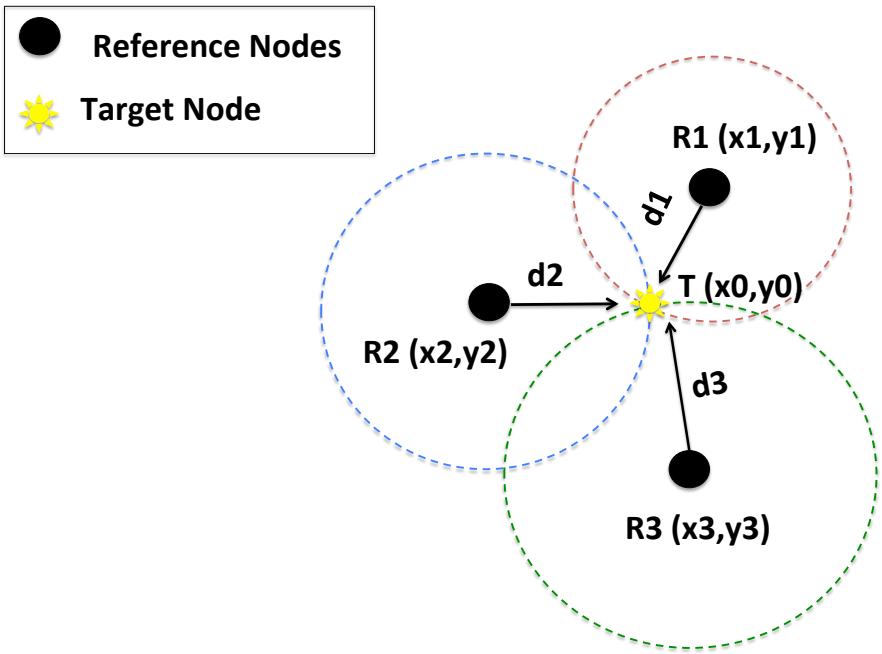

FIGURE 2.6: 2D Positioning with TOA Techniques

Euclidean distance equation:

$$d_i^2 = (x_i - x_0)^2 + (y_i - y_0)^2 \tag{2.2}$$

where i is the number of the reference node, (x_i, y_i) is the coordinate of the reference node and (x_0, y_0) is the coordinate of the target node. The related equations for calculating d_i can be solved using the least-square approach.

2.5.1.1 Advantages and Disadvantages of the TOA Method

By applying the TOA method we can expect to achieve high accuracy in location estimation of a target node. Moreover increasing distances between reference node and target node would not influence the accuracy of location estimation as do other methods such as RSS and AOA.

However, this method has two main problems. The first important problem is synchronisation. To estimate an accurate position, a system's transmitter and receiver have to be synchronised. The second issue is related to the time stamp, which must be labelled in the transmitted signal. The time stamp helps the measuring unit to recognise the transmitted signal [23].

Without synchronisation between a target node, and a reference node another

method known as the Time Difference of Arrival (TDOA) can be used. In this method, first TOA is estimated for each signal travelling between the target node and the reference node. Then, the difference between the arrival times of the two-way signal is calculated. The calculated time gives the position of the target node [21].

2.5.2 Received Signal Strength (RSS)

Similar to the TOA technique, RSS is another signal parameter which makes it possible to estimate the location of a target node. Distance information can be extracted from the energy or power of a signal between two nodes (Figure 2.7). For this purpose, the relation between distance and signal energy should be considered. This relation is normally defined by a theoretical or empirical path-loss model, so the parameters in this method are highly site-specific and environment-dependent.

After extracting the distance between the target node and each of the reference nodes (d_i) from the path-loss model, the coordinate of the target can be obtained according to the euclidean distance equation using Equation 2.2. Just as with the TOA method, the obtained equations for calculating the target coordinates (x, y) can be solved by the least-square method

.

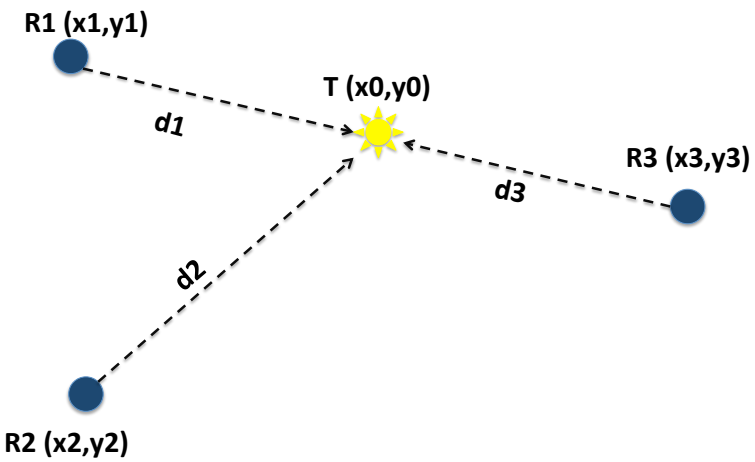

Figure 2.7: Positioning with RSS Techniques

2.5.2.1 Advantages and Disadvantages of the RSS method

In general we can expect to achieve a highly accurate position estimation using the RSS method in LOS and short-range communication. Another significant characteristic of this method is that no extra hardware is needed for either the target or reference nodes. So the implementation of this method is cheaper and easier than the other methods like TOA and AOA [24]. Moreover, in this method the strength of a received RF signal can be measured during normal data transmission. RSS-based methods are also less affected by the bandwidth limitation, but the measurement variability due to the dynamic channel conditions has a significant impact on their accuracy. Unlike the TOA method, this method does not need any time synchronisation between target and reference nodes. On the other hand, RSS needs at least three reference nodes to estimate the 2-D location of a target. Moreover this method cannot provide highly accurate result for Non line of sight (NLOS). This is mainly because of multipath interference. Overall, in this method the strength of the received signal depends strongly on the propagation channel characteristics, which are easily influenced by factors such as path loss, shadowing, fading, reflection, scattering, etc. that should be carefully considered in distance estimation. Overall, the RSS technique is not able to supply very accurate range estimation because of its extreme dependence on the channel characteristics [22].

2.5.3 Angle of Arrival (AOA)

Angle of Arrival is another position-related parameter that specifies an angle between two nodes by estimating the AOA parameter of a signal between the nodes (Figure 2.8). Generally, array antennas have been employed for estimating the AOA of the received signal at the node [21]. To achieve a precise result in position estimation, the process of measuring the angle should be accurate, but high accuracy in a wireless network always will be limited by some parameters such as shadowing, multi-path or the directivity of the measuring aperture [23].

To estimate the location of a target by the AOA technique, let us suppose that our target node is located at coordinates (x, y) and some reference nodes at coordinates (x_i, y_i) where i represents the i^{th} reference node (Figure 2.9). The line between the target node and the reference point intersects the x-axis at an angle of arrival θ_i which

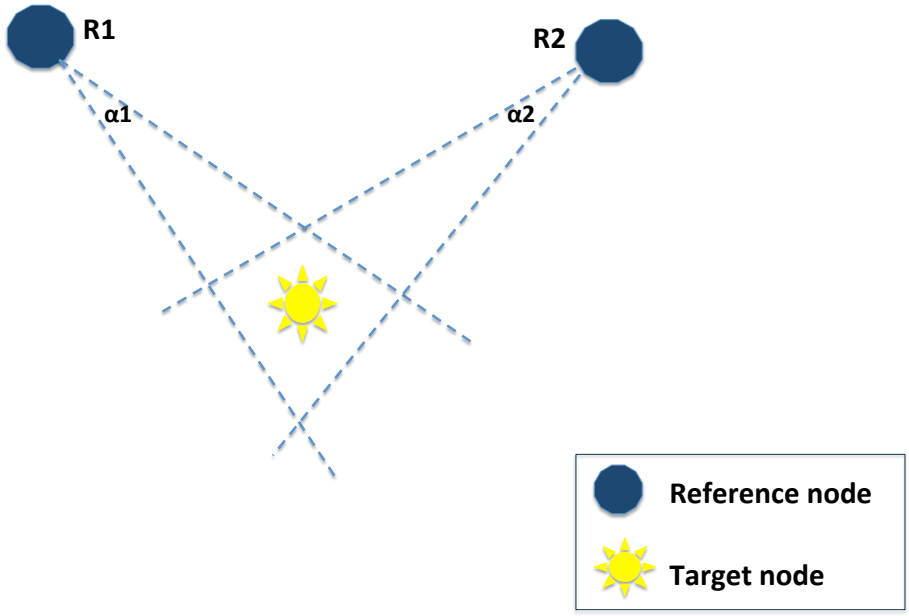

Figure 2.8: Positioning with AOA Technique

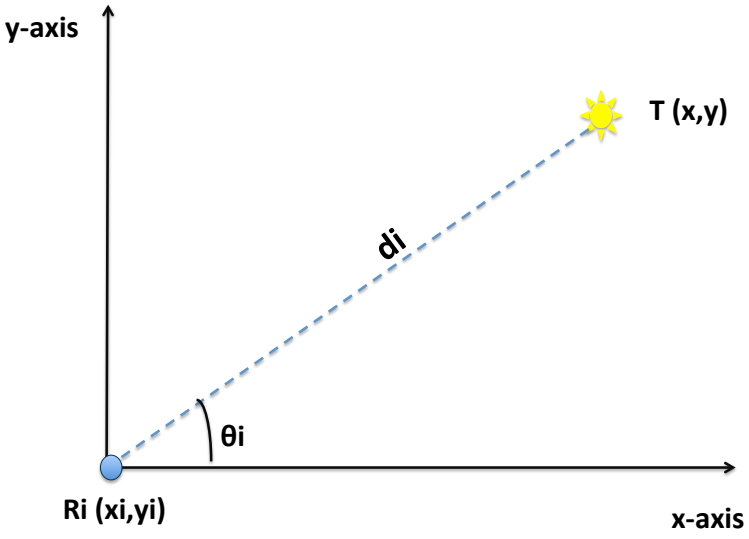

Figure 2.9: The AOA Principle

can be defined as

$$\tan\theta_i = (\frac{y - y_i}{x - x_i}) \tag{2.3}$$

Therefore the coordinate of the target node can be computed using Equation 2.4.

$$\begin{aligned} x &= \frac{d\tan(\theta_2)}{\tan(\theta_2) - \tan(\theta_1)} \\ y &= \frac{d\tan(\theta 1)\tan(\theta_2)}{\tan(\theta_2) - \tan(\theta_1)} \end{aligned} \tag{2.4}$$

where d_i is the distance between the target node and reference node i, θ_1 and θ_2 are the angles of arrival at reference nodes R_1 and R_2 respectively.

2.5.3.1 Advantages and Disadvantages of the AOA Method

Compared to the RSS and TOA schemes, which need to have at least three reference elements, the AOA method requires only two position measuring elements to achieve location estimation. Therefore this method is easy to implement. Moreover, unlike TOA and TDOA no time synchronisation is needed between the measuring units in this method, which is one of the main advantages of AOA [23].

The main disadvantage of the AOA method is related to the changing propagation characteristics for the received signal. For a distant object, this can produce some errors in AOA parameters that result in a degradation of accuracy in the obtained result [25].

2.5.4 Other Position-Related Parameters

In addition to the aforementioned target parameters, other parameters such as Power Delay Profile (PDP), Channel Impulse Response (CIR) and Angular Power Profile (APP) which are related to the received signal can also be employed in location estimation. The PDP gives the intensity and the arrival times of the different ray-paths between the selected transmitter and receiver. Multipath APP information can be estimated using an antenna array in the nodes' locations. On the other hand CIR, which completely characterises the multipath channel, can be considered as another parameter choice. To estimate the location of a target from the aforementioned parameters a database consisting of previous measurements of PDP, APP or CIR at some known locations are commonly needed. Although these parameters can increase the

complexity of the two-step scheme compared to the other schemes, they can significantly increase the accuracy of the position estimation, specifically in a challenging environment [26–29].

2.6 Position Estimation Methods

The second phase in two-step positioning is to estimate the position of the target node from the position-related parameters obtained in the first phase. In general, methods for positioning estimation can be divided into three general categories, summarised as follows.

2.6.1 Proximity

This is a range-free technique that provides a symbolic and relative location information of a target instead of its exact location. It employs a set of detectors at fixed positions, so it can estimate the location of a target relative to a known position or area. Referring to Figure 2.10, assume that T1 and T2 are our target nodes and D is the detector at the known position. A proximity area of the detector is shown by the square. Hence the location of T1 and T2 can be estimated according to whether they are in the proximity area of the detector or not. It can be seen that the target T2 is out of the proximity area of the detector and can not be recognised while the position of T1 can be easily estimated, so the proximity technique can not provide an absolute position estimation. This technique can be used only in certain cases such as a mobile cell acquisition system. The accuracy of this technique is quite low, in the range of 50-200 m, and strongly depends on the cell size (radio coverage by a base station) [25, 30].

2.6.2 Triangulation

Triangulation is a range-based technique which applies the geometric properties of a triangle to estimate the location of a target. This technique can compute the exact location of the target from some reference nodes of known location. In fact, this technique uses signal parameters such as AOA, TOA or RSS to estimate the position of the target node. It has two derivations known as *angulation* and *lateration* methods. Angulation is the technique which locates a target by computing the angles or bearings relative to multiple reference-node positions, whereas in the lateration technique the

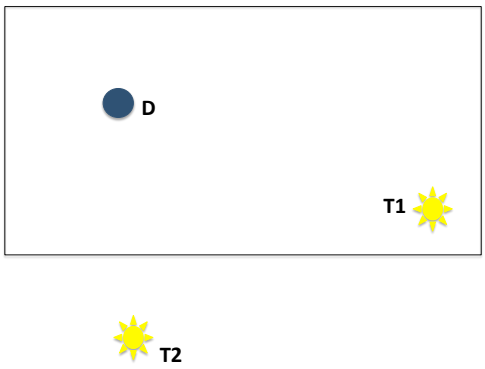

FIGURE 2.10: Proximity Positioning Technique

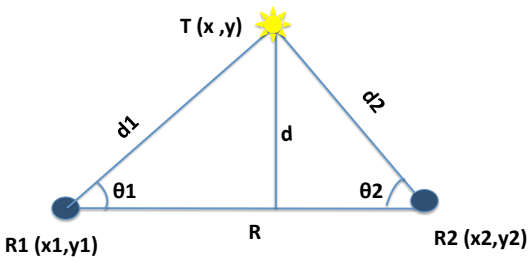

FIGURE 2.11: Angulation Positioning Technique

location of a target can be measured by its distance from multiple reference node positions [31]. Generally, this technique has an accuracy of 3-5 m in an indoor environment [30].

2.6.2.1 Angulation

The basic principle of the angulation technique for a 2-D position estimation is demonstrated in Figure 2.11.

If the geographical coordinates (x_i, y_i) of two reference nodes are known, the absolute position of the target node can be computed by using trigonometric functions as:

$$R = \frac{d}{\tan\theta_1} + \frac{d}{\tan\theta_2} \tag{2.5}$$

$$d = \frac{R\sin\theta_1 \sin\theta_2}{\sin(\theta_1 + \theta_2)} \tag{2.6}$$

$$\begin{aligned} \theta_1 &= \tan^{-1}\left(\frac{y_1 - y}{x_1 - x}\right) \\ \theta_2 &= \tan^{-1}\left(\frac{y_2 - y}{x_2 - x}\right) \end{aligned} \tag{2.7}$$

where R measures the line between the two reference nodes and d measures the perpendicular line between the target node and R. The coordinates of the target can be obtained from the following equations:

$$y = x_1 \tan\theta_2 + (y_2 - x_2 \tan\theta_1) \tag{2.8}$$

$$x = \frac{y_2 - y_1 - x_2 \tan\theta_2 + x_1 \tan\theta_1}{\tan\theta_1 - \tan\theta_2} \tag{2.9}$$

2.6.2.2 Lateration

The basic principle of the lateration technique for a 2-D position estimation is demonstrated in Figure 2.12.

In this technique the location of a target can be obtained by measuring its distance from multiple reference nodes using the RSS, TOA or TDOA method. Assume that the three reference nodes are located at coordinates (x_i, y_i) where i represents the i^{th} reference point. The distance of the target from these three reference nodes using TOA measurement can be calculated as:

$$\begin{aligned} d_1 &= (t_1 - t_0)c \\ d_2 &= (t_2 - t_0)c \\ d_3 &= (t_3 - t_0)c \end{aligned} \tag{2.10}$$

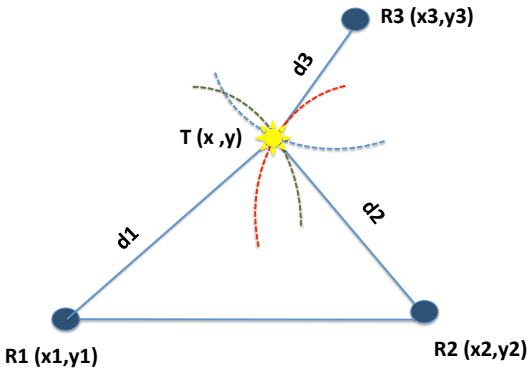

FIGURE 2.12: Lateration Positioning Technique

where t_1, t_2 and t_3 are the times of arrival of a signal sent from target T to reference nodes R_1, R_2 and R_3 respectively and t_0 is the starting time for the target to send the signal. Each estimated distance can be considered as the radius of a circle centred around the anchor node and the unknown location of the target node obtained from the intersection of all the circles. Therefore the coordinates of the target node can be calculated from the following equations:

$$\begin{aligned} x &= \frac{x_2^2 + d_1^2 - d_2^2}{2x_2} \\ y &= \frac{x_3^2 + y_3^2 + d_1^2 - d_3^2 - 2x_1x_3}{2y_3} \end{aligned} \tag{2.11}$$

2.6.3 Fingerprinting

This technique provides accurate position measurement by pre-measuring the location-related data. It uses a database that consists of former estimated signal parameters for a known position. It has two phases: an offline training phase and an online position determination phase. In the offline phase the location data are measured for different places in the position estimation area. In the online phase the location-related data are measured and compared with pre-measured data from the offline phase to estimate the position of the target node [22, 25].

It should be noted that the triangulation and fingerprint techniques are able to provide absolute and relative position information. However, the proximity positioning

technique can only provide proximity of position information. Also, in some cases a combination of these positioning techniques is possible to compensate for the limitation of a single positioning technique [25].

2.7 Capsule Endoscope Location Estimation

Development of an effective localisation system for a WCE represents a significant contribution in the advancement of this technology. Having the information and knowledge of the orientation and position of a WCE inside the GI tract allows better vision of lesions and pathological areas and greatly assists in diagnosis and future treatment. In general, appropriate location system requirements should be carefully selected for medical applications to respond to different needs and environments. Some of these requirements are as follows:

- **Accuracy:** Most medical applications need a highly accurate system (in the range of mm) to enhance the accuracy of the diagnostic process.
- **Security and privacy:** The location information needs to be stored and transferred securely, and only authorised people should have access to it.
- **Sensing time and rate:** The proposed system should provide the real-time location of the target. Hence employing an appropriate sensing time and sampling rate enables us to achieve accurate target detection.
- **Computing time:** There is always a trade-off between computing time and energy consumption that should be taken into account in designing the process.
- **Robustness and fault tolerance:** The developed system should be isolated from any errors. Moreover, it should be able to recover after failure.
- **Cost:** The developed system should have a low cost.
- **Complexity:** The designed system should have a low complexity. In fact the low-complexity issue is associated with low cost. To provide a low-cost system, designing and implementing the system should be done with minimal complexity.

So far two main methods have been proposed to determine the location of a capsule in the digestive tract. These can be categorised as magnetic-field-strength and electromagnetic-wave based methods [32] which will be explored in the following sections. Furthermore some other possible methods for WCE location estimation such as Imaging, Ultrasound, MRI and Radar based positioning systems are discussed.

2.7.1 Magnet-based Positioning System

The magnet-based localisation technique for tracking a capsule in the GI tract has been proposed in [33–37]. This method attracts more attention due to its significant characteristics. The first prominent characteristic is that the low-frequency magnetic signals can easily pass through human tissues without any attenuation. This is due to the fact that the magnetic permeability of human tissues is very similar to air, therefore the magnetic flux cannot be influenced by human tissues. The second important characteristic is that magnetic tracking is considered as a non-line-of-sight method, so it is not necessary that the capsule to be in the line of sight of the magnetic sensor in the detection procedure. On the other hand a growing interest in designing an actuation system to control the movement trajectory, orientation and position of the endoscopic capsule makes using magnet-based localisation even more popular among researchers. In general, a magnetic source and a sensor module are two important devices that are used in the magnet-based localisation method. In the case of a passive capsule endoscope where there is no added actuation system, depending upon whether the capsule acts as a sensing module or a field generator and how the magnetic source is created, the localisation system can be divided into three categories: utilisation of a permanent magnet inside a capsule, utilisation of a 3-axis magnetoresistive sensor mounted inside a capsule, and utilization of a secondary coil embedded in a capsule [32]. It has been shown that the probable precision that magnet-based localisation can offer is in the order of mm [33–35]. Despite its high accuracy, this method is not quite practical, since it needs extra hardware to be embedded in the capsule, significantly increasing the capsule size. It also requires special infrastructure, which limits its application to medical settings.

2.7.2 Electromagnetic-based Positioning System

The other proposed method for capsule localisation is electromagnetic-wave based localisation. Various traditional techniques using Radio Frequency (RF) are: received signal strength (RSS), Time of arrival (TOA), Angle of Arrival (AOA) and Radio Frequency Identification (RFID), which have been explored in several studies [38–41]. The precision of RF localisation depends very much on the adopted technology.

2.7.2.1 Radio Wave

The accuracy of the RF-based localisation technique is highly influenced by the radio propagation environment. The human body is a challenging medium for RF signal

propagation. It has several types of tissues varying in thickness, impedance and dielectric constant. The human body causes different radiation pattern disruptions, power absorption and shift of the central frequency depending on the selected frequency of operation. Power absorption can vary according to the characteristics of the tissue [42]. The human body channel also experiences fading and multipath effects that impact on the accuracy of the localisation method.

Shah et al. in [38] proposed a tracking algorithm for capsule endoscopy, using an RSS localisation method. They also proposed a localisation algorithm based on a lookup table. Since the transit time of the capsule through each GI organ is different, they separated the tract into two regions. Although the authors did not mention how much accuracy they achieved throughout their experiments, they claimed that the accuracy depends on the ability of the algorithm to compare the offline data with the real-time data. Also the accuracy can be improved if the lookup table has gathered a complete set in the offline mode. The result shows that system performance can be significantly improved if a human phantom model had been used for the offline data collection.

In [39], the RSS method was also selected to perform capsule positioning from several access points. In the end, the acquired position data were analysed by a trilateration algorithm to estimate the real-time position of the capsule. An average error of 25% was achieved in most of the measurements. The writers claimed that parameters such as receiver and transmitter sensitivity, antenna orientation, multi-path fading, shadowing and frequency of sample measurement have a significant effect on the received signal strength. For example in the case of the sample measurement time, they increased the measurement time from 5 minutes to 10 minutes and a 4% decrease was observed in the error.

In another study [43], the authors assessed the factors that influence capsule localisation accuracy inside the GI tract to find the localisation accuracy bounds for various digestive organs. The simulation was done with two different sensor configurations, in which a 4×4 sensor array was placed in front of the human body, or one array sensor was in front of the body surface and the others on the back of the body. The location error for the stomach was around 52 millimetres by using one 4×4 sensor array, whereas the error decreased to 40 millimetres by applying two 4×4 sensor arrays. Overall, by using one 4×4 sensor array the location error in the small intestine was below 48 mm in 90% of their experiments, whereas it reached 50% in the large intestine. Moreover, a location error of 38 mm was achieved in 50% of their experiments in three organs, by deploying another 4×4 sensor array. These results show that the large intestine has

a greater location error than the other organs in the presence of the same number of sensors. In principle, the performance of the system in terms of location accuracy will improve if more sensors are employed in a system.

The authors in [40] proposed a localisation system for the capsule endoscope scenario based on the RSSI technique. The location of the capsule was calculated based on the measured RSSI and applying the maximum-likelihood (ML) or Least Squares (LS) location estimation method after each receiver received the packets from the transmitter. The result showed that the RMS location estimation error in the ML method was below 4 cm, whereas it was about 7 cm for the LS method. Overall, the RMS location estimation errors for both methods were less than 8 cm, and this was steadily decreased by increasing the number of transmitted packets.

In [44, 45], the authors have done some experiments to localise a WCE based on the RSS method and claimed that the achieved average position error was 37.7 mm with a maximum error of 114 mm.

In the TOA technique, the ranging resolution is easily degraded by a limited bandwidth. Also, the accuracy of the estimated range is highly impacted by the GI filling and emptying cycle and GI movement [43]. Furthermore, the propagation velocity inside the human tissue is not constant. Therefore, when designing a TOA-based localisation system, the propagation velocity inside the human body must be estimated based on the average permittivity of the human organs and tissues [46]. Likewise, AOA is not a reliable technique for localisation of an object, even in indoor environments, and it is not considered an appropriate technique for localisation of a WCE, since the human body is a more complex environment than any other indoor environments [38].

Since RSS and TOA are two common localisation techniques, the authors in [42] presented a comparison between the accuracy of these localisation methods for the inside of the human body. Overall, the highest error of 3.5 cm was observed for measurements using the TOA method whereas the highest distance measurement error was 5.1 cm in the RSS method. This result confirms that the TOA method is more accurate than the RSS method.

2.7.2.2 RFID Positioning System

RFID is another RF-based technique which has been considered as a candidate method for localisation in capsule endoscopy. RFID technology is able to store and retrieve data through electromagnetic transmission to an RF-compatible integrated circuit. By the aid of this technology flexible and low-cost identification of a node is possible. This system is expected to be used in complex indoor environments such as offices, hospitals,

etc. [25, 47]. The performance of RFID was evaluated for the capsule endoscopy scenario in [48–50], where the capsule detection can be achieved by tracking an RFID tag which is embedded inside the capsule. In these studies a 3D algorithm for location estimation of a WCE was developed. and they achieved approximate deviations of 0.5 cm in the x and y directions and 2 cm in the z direction. Hou et al. [50] proposed a high-resolution localisation system based on an RFID system in the UHF band. A mean location estimation error of less than 2 cm was achieved when the antennas were placed at a 3 cm distance in a 3D antenna array. The authors pointed out that the location estimation error can be increased by adding more antennas into the system or locating antennas closer to each other. Hence, optimal accuracy is achievable by improving the location estimation algorithm or deploying a better directional pattern for the tag antenna. In general, unstable signal strength, environmental interference and signal variation of RFID can reduce positioning accuracy. Moreover, the number of RFID tags can influence the positioning precision. In general employing more tags results in better positioning precision but at high cost [51].

2.7.3 Image-based Positioning System

2.7.3.1 Computer Vision

Using computer vision to process and analyse the images received from the capsule endoscope to determine the location of a capsule is another method which has been investigated in some studies [52, 53]. In these studies the MPEG-7 visual content descriptor and Homogeneous Texture descriptors were used to analyse the recorded images, including features like colour, textures and shapes. However the accuracy of the obtained result was not mentioned in these articles. In another study it was shown that, by using computer vision and an event-boundary detection algorithm, it is possible to report events such as intestinal bleeding or when the capsule is leaving one organ and entering another [54]. According to the obtained results the authors claimed that an accuracy of 51% was achieved by this method, although using this method can just provide us basic information.

2.7.3.2 X-ray

X-radiation is a form of electromagnetic radiation at frequencies in the range from 30 petahertz to 30 exahertz. X-rays are widely used in medical imaging and airport security. They are a type of ionising radiation that due to its high energy can easily

ionise atoms. So a very high radiation dose over a short time can be harmful, and increases the chance of developing radiation-induced cancer.

Fluoroscopy is an imaging technique based on x-ray radiation which is normally used to acquire real-time 2D images of the body. In [55], the authors have developed a robotic magnetic navigation system that can control the capsule movement with an omnidirectional steering accuracy of 1°. Moreover, by integrating a fluoroscopy technique, real-time tracking of the capsule was achieved with an error of 1 mm. The drawback of the proposed method lies in acquiring visual information of the capsule instead of obtaining its actual position and orientation. Aiming at solving this problem the authors in [56] proposed a method to automatically determine the orientation and position of a capsule endoscope using both X-ray and image processing techniques. In this method if the geometry of the capsule is known, then depending on its shadow produced in images the position can be calculated with the aid of image processing. Although applying X-rays in location estimation of a capsule might deliver highly accurate results, the health hazard for patients exposed to a high dose of X-rays is not negligible. Despite all the X-ray hazards, using a hybrid location estimation system which includes the X-ray method with another method of localisation might provide better results, while the radiation dosage would be less.

2.7.3.3 Gamma-ray

Gamma radiation (or gamma rays) is extremely high-frequency electromagnetic radiation (above 10 exahertz) with high energy. It can be generated by radioactive atoms and by nuclear explosions. It is generally known as an ionising radiation so is potentially harmful. In medical applications, gamma rays are sometimes used to treat cancerous cells and tumours through the body by damaging the DNA of the tumour cells. Moreover the gamma scintigraphy technique takes advantage of gamma rays to estimate the position of an Enterion capsule which has been designed for delivery of a wide range of different drug formulations into any region of the gastrointestinal tract [57, 58]. In spite of the fact that gamma rays have been used in an enterion capsule for drug delivery purposes they have never been studied for localisation of a capsule endoscope. So they can be considered as a possible candidate for location estimation of a capsule and need more studies to investigate the performance in terms of harmfulness and suitability.

2.7.4 Ultrasound-based Positioning System

Ultrasound is a non-invasive procedure that provides quick visualisation to assess internal organs within the human body or blood flow inside the arteries. A sound wave at a frequency range between 1-50 MHz is sent out toward the body tissues using a device called a transducer. The sound waves which bounce off the organs return to the transducer and then images of the organs can be created by processing the reflected waves and converting them into an image. In general, the speed of sound waves inside the body varies and depends strongly on the type of tissue which is encountered. Therefore different types of tissue can be recognised according to these important facts: how much of the sound waves are returned with at speed as well as how they can be translated and analysed by the transducer.

On the other hand, ultrasound is known as a diagnostic imaging technique which can provide us with location information in soft tissues with minimal adverse health effects. There are two possible approaches to estimate the capsule location inside the gastrointestinal tract using ultrasound. The first, straightforward, approach is by measuring the time of flight between ultrasonic pulses emitted from the transducer toward the capsule and reflected by the capsule. The accuracy provided by this approach depends strongly on the speed of sound through different human tissues. Moreover the location estimation accuracy can be easily degraded if the capsule moves outside of the sensing region [59, 60]. To improve the location estimation performance and eliminate the requirement of the sensing region another approach was proposed. In this approach a new version of the capsule endoscope needs to be designed, equipped with small on-board ultrasonic emitters. Moreover, some receivers need to be located around the abdomen of the patient to receive the sound wave [61]. However in none of the studies has the accuracy of capsule location estimation been reported, but has been expected to be accurate location information despite the fact that the gas and air inside the GI tract and bones and ribs act as strong reflectors of the sound wave [62].

2.7.5 MRI-based Positioning System

Magnetic resonance imaging (MRI) is another diagnostic imaging technique widely used in medical applications. The authors in [63] claimed that they had a novel development to access prostate tissue by tracking MRI guided needles for therapeutic procedures and biopsy of the prostate. In this way the spatial position of the needle can be determined by having some miniature RF coils in the needles which are able to sense the MRI pulse sequence. In [64] the authors claimed that by using three micro-tracking coils in the

needle they can achieve a mean position error of 0.2 mm. According to the author's knowledge no study has been reported in terms of using MRI in capsule endoscope positioning, however this technology can still be considered as a candidate technique for determining capsule position.

2.7.6 Radar-based Positioning System

Radio Detection and Ranging (Radar) is a method that is traditionally used to determine the range, altitude, direction, or velocity of an object. The basic principle of radar operation is simple. A Radio-Frequency wave is sent by a transmitter towards a target. At the receiver the detection of the target is effected when the antenna receives the reflected wave from the target. Deployment of a radar system in the medical field is another solution to diagnose various diseases of the human body. Several studies have investigated the usefulness of this technology in diagnosis procedures [65–67]. To the best of our knowledge, this technology has never been studied for capsule localisation. In this project the main aim is to verify the performance and applicability of a radar system in position estimation in capsule endoscopy. Therefore in the following section we provide a general overview of a radar system and its requirements.

A comparison of positioning accuracy offered by the different aforementioned positioning methods for capsule localisation is presented in Table 2.2.

2.8 Radar System

Radar technology has been used for military purposes since the 1930s. Through subsequent development of Radar, it has been used in a wide range of applications such as: meteorology, transport, astronomy, geophysical radar and medicine. The most important functions of radar are: search for the object, target detection, measurement of the target position and velocity [68].

The basic principle of radar operation is very simple. A Radio-Frequency (RF) wave is sent by a transmitter toward a target. The target reflects a portion of the transmitted RF energy toward a receiver. On the receiver side, the detection of the target is effected when the antenna receives the reflected wave from the target at an energy level sufficiently large to be discriminated from noise. Figure 2.13 illustrates the basic principle of radar operation.

Table 2.2: A comparison of positioning accuracy offered by different positioning methods for capsule localisation

	Localisation Methods	Reference	Capsule Position Error
Magnet-based Positioning System	Permanent Magnet	[35] [36]	error <2 mm
	HF alternating Magnetic Field	[37]	error <2 mm
Electromagnetic-based Positioning System	Radio Wave	[43] [40] [44] [45] [42]	error >20 mm
	RFID	[48] [49] [50]	error >20 mm
Image-based Positioning System	Computer Vision	[52] [54]	error >20 mm
	X-ray	[55]	error <2 mm
	Gamma-ray	[58]	NA
Ultrasound-based Positioning System	-	[60] [61]	NA
MRI-based Positioning System	MRI	[63] [64]	error <2 mm

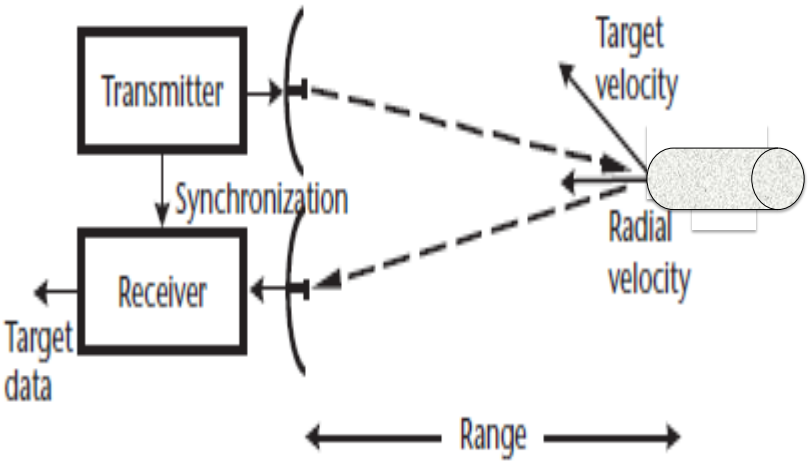

FIGURE 2.13: Concept of radar operation

In our work the target (assumed to be an endoscopic capsule) is in motion, therefore radar technology can be also a suitable candidate technique for object localisation. Moreover, based on radar performance, there is no need to consider any extra transmitter/receiver at the target side since the location of the target can be calculated from the signal reflected from the target. Thus, no extra hardware needs to be designed for the capsule node, resulting in a low-complexity system. However, since the transmitted and reflected waves should pass through the high-attenuation human body medium, a sensitive receiver is a crucial requirement. Also, the dielectric properties of each tissue layer are highly frequency dependent, so it is important to deploy a radar system at a frequency which permits both less attenuation and high resolution.

Modelling and analysing of radar at the system level needs consideration of several parameters like radar components such as transmitter, receiver, antenna, operating frequency, as well as operating environment and condition. Moreover, the characteristics of a target which is going to be searched or localised by a radar system also influence the radar performance. One of the most important target characteristics is the Radar Cross-Section (RCS) which is discussed in the next section.

2.8.1 Radar Cross-section

One of the important concepts in radar systems is the Radar Cross-Section. RCS is a measure that shows the detectability of an object by a radar system. In general, an object can be detected based on the amount of energy that is reflected from it, and the RCS of a target shows how much of the incident power is intercepted, reflected or directed back toward the receiver. Thus, a target with a larger RCS can be more easily detected by a radar system. There are various factors that affect the amount of reflected energy to the source and RCS respectively. They are listed as follows [68, 69].

1. **Size:** A larger object reflects a larger amount of the energy, so the RCS would be greater in this case and the object can be more easily detected.

2. **Material:** Materials such as plastic, fibreglass, cloth or wood are less reflective, whereas a metal, with a strong reflection characteristic, can be a good choice to produce a strong reflected signal. Some experiments prove that even a thin layer of metal can change the reflective behaviour of an object.

3. **The incident angle:** This is the angle at which the radar beam meets a target. This angle strongly depends on the shape of the target.

4. **Reflected angle:** This is the angle at which the reflected signal leaves a target and depends on the incidence angle.

5. **Polarisation:** In regard to the position and location of a target the polarisation of transmitted and received signals can influence the RCS.

In this study we assume that the capsule endoscope has a simple cylindrical shape with a size of 11 mm × 26 mm, so the related cross-section can be calculated from the following equation:

$$\sigma = \frac{2\pi r h}{\lambda^2} \tag{2.12}$$

Here, r and h are the radius and the height of the capsule, respectively and λ is the wavelength, which is a function of the material in which the cylinder is embedded. On the other hand, from Maxwell's equations the velocity of the electromagnetic wave in a medium can be given as [70]

$$v = \frac{1}{\sqrt{\mu\epsilon}} \tag{2.13}$$

where ϵ and μ are the absolute permittivity and permeability of the medium respectively and can be written as:

$$\epsilon = \epsilon_r \epsilon_0 \tag{2.14}$$

$$\mu = \mu_r \mu_0 \tag{2.15}$$

where ϵ_r and μ_r are the relative permittivity and permeability and ϵ_0 and μ_0 are the permittivity and permeability of free space. Since most of the media that we are working with, such as human tissues, are non-magnetic, then $\mu_r = 1$ and by substituting Equations 2.14 and 2.15 in Equation 2.13 the velocity of the wave in a medium can be obtained by

$$v = \frac{1}{\sqrt{\mu_0 \epsilon_r \epsilon_0}} = \frac{c}{\sqrt{\epsilon_r}} = \frac{c}{n} \tag{2.16}$$

where n is the refractive index of the medium.

Since the propagation velocity through the human body is different from that in free space, the velocity can be calculated based on a simplification made by taking the average permittivity of the human tissues. This permits a rudimentary working model, forming the basis of comparison with FDTD results.

Before any design can be attempted for our radar system it is necessary to select an appropriate operating frequency. In the next section this fundamental concept of the radar will be discussed.

2.8.2 Radar Frequency Bands

Radar systems have been operated at a wide range of frequencies. It is apparent that the appropriate frequency selection for a radar system depends on the application. The assigned frequency bands for radar systems and specific applications are summarised in Table 2.3. As can be seen in Table 2.3 certain requirements of an application and its environment lead to the choice of an appropriate frequency. On the other hand, for medical purposes certain applications are legislated to operate in specific frequency bands. Devices such as capsule endoscopes, which are used inside the human body for some diagnosis procedures of gastrointestinal diseases, are also considered as part of a Body Area Network (BAN). Therefore the selected operating frequency for our radar system should be matched with BAN requirements as well.

Table 2.3: Assigned Frequency Bands for Radar

Radar Band	***Frequency Range***	***Characteristics***	***Applications***
HF	3-30 MHz	Reflects off ionosphere	OTH radar
VHF	30-300 MHz	Very large antennas Ionosphere distorts propagation	Search radar
UHF	300-1000 MHz	Very large antennas Ionosphere distorts propagation	Search radar
L Band	1-2 GHz	Large antennas	Search radar
S Band	2-4 GHz	Moderate size antennas Moderate measurement precision	Multifunction radar
C Band	4-8 GHz	Moderate size antennas Moderate measurement precision	Multifunction radar
X Band	8-12 GHz	Small antennas Precision measurement	Tracking radar Airborne radar
Ku Band	12-18 GHz	Very small antennas Good measurement precision	Tracking radar Airborne radar Short-range radar Precision-guidance radar
K Band	18-27 GHz	Very small antennas Good measurement precision	Tracking radar Airborne radar Short-range radar Precision-guidance radar
Ka Band	27-40 GHz	Very small antennas Good measurement precision Atmospheric and rain loss	Short-range radar Precision-guidance radar
V Band	40-75 GHz	Severe atmospheric and rain loss	Space-to-space radar
W Band	75-110 GHz	Severe atmospheric and rain loss	Space-to-space radar
Millimetre waves	110-300 GHz	Severe atmospheric and rain loss	Space-to-space radar

TABLE 2.4: Frequency band and bandwidth of different PHY layers of IEEE 802.15.6 [9]

Human-Body Communication	
Frequency	**Bandwidth**
16 MHz	4 MHz
27 MHz	4 MHz
Narrowband Communication	
Frequency	**Bandwidth**
402 - 405 MHz	300 KHz
420 - 450 MHz	300 KHz
863 - 870 MHz	400 KHz
902 - 928 MHz	500 KHz
950 - 956 MHz	400 KHz
2360 - 2400 MHz	1 MHz
2400 - 2483.5 MHz	1 MHz
UWB Communication	
Frequency	**Bandwidth**
3.2 - 4.7 GHz	499 MHz
6.2 - 10.3 GHz	499 MHz

In general, BANs are able to provide a short-range (2 to 5 m), low-power, high data rate (up to 10 Mbps) and highly reliable wireless communication that can be used in the close vicinity of or inside the human body. The IEEE 802.15.6 standard defines a number of physical-layer modes of operation for different BAN scenarios including: narrowband, ultra wideband (UWB) and human-body communication (HBC) which are briefly discussed here. In addition a summary of these different physical layers and their operating frequency bands are given in Table 2.4.

- **Human-body Communication:**
  Human-Body Communication (HBC) is a non-RF based communication technique which uses the human body as a communication channel. It is a promising candidate for data transmission and operates in two frequency bands centred at 16 MHz and 27 MHz. Both of these frequency bands are supported in the United States, Korea and Japan, whereas the second only is supported in Europe.

- **Narrowband Communication:**
  Narrowband (NB) communication is suitable for more health-care applications because it has a lower carrier frequency which results in less attenuation through

the human body. It supports various modulation schemes and bit rates. In general seven different frequency bands are employed in this communication technique. Medical Implant Communication Service (MICS) in the range of 402-405 MHz is the first licensed band for NB communication and is mostly used for implant communication such as capsule endoscopy. The Wireless Medical Telemetry Service (WMTS) and Industrial, Scientific and Medical (ISM) bands at 2360-2400 MHz and 2400-2483.5 MHz are the next frequency bands used in NB communication. Among these frequency bands the ISM band alone supports a high data rate.

- **Ultra-wideband Communication:**
  Ultra-wideband (UWB) has attracted more attention in recent years as a promising air interface for short-range and high-data-rate communication, originally used in sensing, radar, military communication and some niche applications. Based on the definition of the Federal Communications Commission (FCC), UWB can refer to any radio technology with a transmission bandwidth larger than 500 MHz or 20 percent of the centre frequency [71]. The FCC regulates the use of UWB in a licence-free band in the range of 3.1-10.6 GHz, which supports low-power spectral density emission. This aids the enhancement of UWB in short-range, indoor environments, and environments sensitive to RF emissions [72].

  Shannon's channel capacity theorem has shown the huge bandwidth of UWB to be capable of supporting a large channel capacity without the need of high transmission power. Hence UWB is applicable for use in existing technologies without leading to any harmful interference. Furthermore, the classic Cramér-Rao Bound (CRB) analysis has shown UWB to have a high timing resolution and more accurate ranging and location capability, due to its huge bandwidth [73]. The aforementioned characteristics of UWB make it an ideal technology for precise localisation which can compete with GPS performance in BAN tracking [71].

  The main propagation mechanism of UWB outside the human body is diffraction, where as reflections and surface waves are minimal. As this radio technology uses short pulses for radio transmission, its transmitter can be designed without any complexity. Thus extremely low energy consumption and a remarkable increment in battery lifetime are achieved. However, a lot of challenging issues need to be faced before their wide adoption, such as: the tradeoff between operating rate

and range via multi-user access, multi-antenna UWB techniques for coverage and throughput enhancement, equalisation or reception techniques in multipath environments, and the coexistence of UWB with existing systems [73].

In the medical environment, several conventional methods such as X-ray, Computed Tomography (CT), Mammography or Magnetic Resonance Imaging (MRI) are widely used to facilitate the diagnosis procedure by providing images from inside the body. However all of these technologies can seriously jeopardise the health of patients due to exposing them to ionising radiations or high magnetic fields. Recently, ultra-wideband radar has been proposed for medical imaging and diagnosis purposes due to its lower cost and higher safety in terms of exposure to ionising radiation as compared to MRI, X-ray and CT [74]. Another main specific characteristic of UWB radar is its high spatial resolution, which assists users to perfectly distinguish targets from clutter.

Due to the particular applications of UWB radar in medicine, it is essential to make sure that the field radiated by UWB radar is within the safety guidelines. In [75], the main feature of UWB is stated to be the low electromagnetic radiation from the low-power radio pulses, of less than -41.3 dBm/MHz in indoor environments. The safety issues regarding human body exposure to the UWB electromagnetic field can be assessed and evaluated according to the International Commission on Non-Ionizing Radiation Protection (ICNIRP) guidelines [76]. On the other hand, according to the FCC regulations emission masks are defined based on the measurement of Effective Isotropically Radiated Power (EIRP) on a particular bandwidth. So for the case of UWB medical imaging systems, where the radiation is between 3.1-10.6 GHz and uses a resolution bandwidth of 1 MHz, the EIRP should not exceed -41.3 dBm/MHz [72]. The authors in [77] discussed safety issues related to UWB radar. According to their obtained results the safety guideline of ICNIRP will be satisfied if the UWB radar's emitted field meets the requirements of the spatial and/or ground emission masks. Hence, UWB would be safe for the human body even at short distances and can be easily used for medical applications due to its low radiation strength.

In general the choice of an appropriate operating frequency can have a big effect on network performance. Ultra-wideband frequencies offer higher data rates and higher throughput, whilst lower frequencies experience less shadowing and attenuation from the body [78]. In Chapter 4 we discuss some analysis performed to select the best possible frequency for a radar system for WCE location estimation.

2.9 Chapter Summary

In this chapter we review the layout of common wireless capsule endoscopes as well as the anatomy of the small intestine. The review is followed by discussion on the conventional localisation methods and estimation techniques for wireless positioning. We further discuss a number of possible methods for localisation of a WCE. Among the methods discussed we have selected a radar system as our localisation method and a brief discussion was presented on a radar system and its requirements. This is mainly because based on radar performance, there is no need to consider any extra transmitter/receiver at the target side since the location of the target can be calculated from the signal reflected from the target. Thus, no extra hardware needs to be designed for the capsule node, resulting in a low-complexity system.

3

Literature Review On In-body Path-loss Models

3.1 Introduction

Propagation of Radio-Frequency waves inside the human body presents different characteristics compared to wave propagation in indoor or outdoor environments. This is mainly because waves propagate through different tissues and organs with different electronic characteristics, attenuating the signal significantly.

On the other hand, optimal results in localisation depend on accurate knowledge of the propagation-channel characteristics. Recently, several studies have been devoted to investigating the biological effect of implantable wireless devices and their propagation characteristics through the human body. Since the human body is a lossy medium, precise knowledge of the in-body propagation channel and path-loss model is required to design a competent wireless communication system. The main objective of this chapter is to present and recap the existing path-loss channel models proposed specifically for the GI tract.

3.2 Importance of In-Body Path-loss Model

Prior to developing any optimised system for in-body wireless communication, it is required to have a deeper understanding of wave propagation inside the human body due to the different characteristics of the human body as a propagation environment from any other environments. In general the path loss is defined as the attenuation of electromagnetic waves propagating through an environment. Determination of an accurate path loss is necessary.

Several studies on wave propagation inside the human body have been carried out for an efficient telecommunication system design in different implant medical applications. Scanlon et al. [79] investigated the radiation performance of an implanted source at 418 MHz and 916.5 MHz for the human vagina. Khaleghi et al. [80] proposed an in-body path-loss model for the human chest at UWB frequency. A path-loss model for the homogeneous tissue of the human brain, muscle, fat and skin at 2.45 GHz was proposed by Kurup et al. [81, 82]. In another study [83], the authors developed a simplified generic in-to-out path-loss model which can apply for a heterogeneous human model at 2.45 GHz. The authors claimed that the novelty of the proposed model is its independence from the antenna characteristics. Hence the model is no longer antenna specific. The authors in [84] developed an empirical path-loss model for a multi-implant scenario and studied the communication links between implants in organs such as the liver, heart, spleen and kidneys. However, in the case of capsule endoscopy, a proper and efficient in-body channel model for the abdominal region is necessary to design the communication interface. Therefore, this section will focus on current path-loss models for the abdominal region.

In general a path-loss model can be classified as follows:

- Deterministic model
- Empirical model
- Semi-empirical model

We tried to allocate each developed path-loss model to its own appropriate loss category in order to be able to easily compare these models.

3.3 Empirical Model

Most of the developed path-loss models for different wireless applications use empirical models. Empirical models, which are also called statistical or stochastic models, are

mostly based on measurements and observation procedures, with less reliance on a detailed knowledge of the measurement's environment. The model's accuracy depends on the measurements [85]. In this section we focus on empirical path-loss models, mainly for the GI tract.

3.3.1 IEEE 802.15 TG6 In-body Path-loss Model at 403.5 MHz

Sayrafian-pour et.al. [86], from the National Institute of Standards and Technology (NIST), investigated the electromagnetic propagation from a medical implant through the human body and developed an in-body path-loss model. The proposed path-loss model has also been adopted by the IEEE802.15 task group TG6 for BAN. A 3D visualisation platform and 3D full-wave electromagnetic simulator (HFSS) were deployed for this purpose. Simulations were done at a frequency of 403.5 MHz in the Medical Implant Communication Service (MICS) band for near-surface and deep-tissue implant devices. Therefore the developed path-loss model consists of two channel models: implant to body surface and body surface to the external node channels.

The deep-tissue scenario can be applied to capsule endoscopy when the capsule is positioned in the upper and lower part of the stomach at 95 mm and 118 mm below the body surface respectively.

The proposed statistical path-loss model was described as:

$$PL(d) = PL(d_0) + 10n \log(\frac{d}{d_0}) + S \quad d \geq d_0 \tag{3.1}$$

where

$$S \sim N(0, \sigma_s^2)$$

Here S is the random scatter, with zero mean and variance of σ_s^2, and n is the path-loss exponent, which depends on the propagation environment. The reference distance of d_0 was 20 mm from the body surface in this study.

Table 3.1 summarises the extracted parameters of the statistical path-loss model, which are based on simulation data. To calculate the path loss in an environment without any objects and obstacles, the free-space path loss can be added as an additional loss to the above model. However, in the presence of any objects or obstacles

TABLE 3.1: Parameters of the statistical path-loss model [86]

Channel model	Implant location	PL(d_0)(dB)	n	σ_s(dB)
Implant to Body Surface	Deep Tissue	47.14	4.26	7.85
	Near Surface	49.81	4.22	6.81
Implant to Implant	Deep Tissue	35.04	6.26	8.18
	Near Surface	40.94	4.99	9.05

in the surrounding body environment, a further loss should be included into the aforementioned model. However, one of the objections to this path-loss model is that the model just considers the distance between the transmitter and a receiver antenna and the environmental noise. Moreover in extracting the loss model it just assumes that the receiver and the transmitter antenna have an omni-directional radiation pattern, whereas the radiation pattern of an antenna can be easily distorted when the antenna is located in different complex environments such as the human body.

3.3.2 In-body Path-loss Model at 2.4 GHz

The authors in [87] proposed an in-body empirical path-loss model for the heterogeneous medium, using the anatomical model of a 6-year-old male child from the virtual family together with the 3D electromagnetic solver SEMCAD X to perform the FDTD simulation. For this purpose, an implantable dipole antenna was designed to suit muscle dielectric properties. The operating frequency was chosen at the licence-free 2.45 GHz of the ISM band, due to its large bandwidth, high-bit-rate support and the small size of the antenna.

The simulations were performed 162 times for a homogenous medium of human muscle tissue and then in a heterogeneous medium with four different scenarios including: esophagus, stomach, small intestine and large intestine. In each scenario the path loss was measured while the transmitter and receiver were set at different positions and locations. The study focused on deep tissue implants with a maximum distance of 8 cm from the body surface. Then the path-loss model was derived with respect to the simulation results and defined as

$$PL|_{dB} = \left(10\log_{10} e^2\right)\alpha_n d + C_n|_{dB} + X_n|_{dB} \tag{3.2}$$

Table 3.2: Parameters for the heterogeneous medium for in-body path loss [87]

n	Scenario	$\alpha_n(1/cm)$	C_n(dB)	σ(dB)
1	Homogenous muscle tissue	0.69	14.71	–
2	Esophagus	0.67	14.24	1.31
3	Stomach	0.68	13.40	1.22
4	Small intestine	0.89	12.36	2.25
5	Large intestine	0.89	11.48	4.14

where $n = 1, 2, \cdots, 5$ denotes the muscle, esophagus, stomach, small and large intestine tissues respectively. α_n is the effective attenuation constant in each body region, C_n is a constant and X_n is a random-error term with a zero mean, a normal distribution and standard deviation of σ. The values of α_n, C_n and σ for each scenario are listed in Table 3.2.

Overall, a variation in path loss was observed when the assumed implant (capsule) went from one tissue to another, since the dielectric properties of each tissue are different from the others. For instance the small intestine and large intestine have a higher conductivity than the other tissues, hence they produce higher attenuation.

3.3.3 Implantable WBAN Channel Model for Digestive Organs

Aoyagi et al. [88] developed a path-loss model based on simulation and measurement analysis of a wave through the digestive tract. The SEMCAD solver and a human model of a Japanese adult male were used for electromagnetic simulations at 403 MHz. The implant node (Capsule endoscope) was placed in different locations of the digestive tract, such as the esophagus, stomach, duodenum, small intestine and large intestine, while a quarter-wavelength dipole antenna (as the receiver) was placed over the navel at a distance of 1.5 cm from the body surface. The path loss was given by

$$PL(d, \theta) = a.d + b + P(\theta) + N[dB] \tag{3.3}$$

where a and b are the gradient and intercept coefficients respectively. d is the distance between the implant and receiver. N defines a stochastic fluctuation which has a normal distribution with zero mean and standard deviation of σ_N. θ is the angle between the

TABLE 3.3: Estimated parameters of the Implantable WBAN channel model

Parameter	Value
a (dB/ cm)	1.92
b (dB)	39.85
σ_N	6.59
X_c	0.145

receiver and transmitter antennas and $P(\theta)$ in dB is a fluctuation due to the capsule direction and can be expressed as:

$$P(\theta) = -20log_{10}\left((1.0 - X_c)\cos(\theta) + X_c\right) \tag{3.4}$$

where X_c is an antenna direction fluctuation defined as the difference between the main (z) and cross (x, y) electric field directions. To evaluate the simulation results some measurements were carried out using a liquid human phantom, with the dielectric properties of human muscle. The path-loss model and its parameters were then developed by combining the simulation and the experimental results. Table 3.3 summarises the estimated parameters of the path-loss model.

The authors emphasised the dependence of the path loss on the type of antenna by explaining that the loss would be varied by changing the receivers's antenna to a printed-chip antenna. This is mainly because of the difference in the two antennas' gains. They also stated that their results were contributed to Task Group six (TG6) of IEEE 802.15 (Wireless Personal Area Network) standardisation.

3.3.4 Path-loss Model at UWB Frequency

The authors in [89] presented at UWB channel model for propagation of UWB pulses in the GI tract in the 3.4-4.8 GHz frequency band, since none of the proposed narrow-band path-loss models of implanted sensors are applicable to UWB channel modelling. The most promising feature of the proposed model is its taking into consideration the effect of antenna orientation and tissue absorption for driving the path-loss model. The electromagnetic simulation was performed by employing a voxel anatomical model of the National Library of Medicine (NLM), with the several dielectric properties of human tissue. To solve Maxwell's equations for the numerical simulation the finite integration technique (FIT) was used. Furthermore, a grid of field probes were set in intestine locations within the human model. The space between the probes was 10 mm

and 20 mm along the horizontal and vertical axes respectively. Throughout the entire simulation the effect of body reflections was ignored, since a perfectly matched layer (PML) was applied to the simulation.

In the capsule endoscope scenario, the transceiver moves through the GI tract, so its position and depth inside the human body vary from time to time. To consider the mobility of the capsule, the proposed channel model calculates the average path loss with respect to different receiver positions located around the body. The position of each receiver was defined by its height and angle with respect to a reference location. For this purpose, 12 antennas with equal angular spacing were located on a horizontal plane 30 mm above the navel. This horizontal plane was considered as the reference height. To define the reference angle an imaginary line was considered from the centre of the body to the navel. The positions of all the antennas were also set at a 10 mm distance from the skin. A UWB Gaussian pulse shaped by a Hamming window was transmitted toward the human body by a centre-feed elliptical dipole antenna. The operating frequency of the transmitter antenna was 2-6 GHz with a return loss of less than 10 dB and transmit power of 0 dBW.

The path loss was measured for various angles and heights around the body by averaging the obtained attenuation at the receiver probes. A path-loss divergence was obtained around the average, since each receiver probe was set at a different distance from the skin inside the digestive tract. The average path-loss model can be expressed as a Fourier sine and cosine series, since it gives excellent fitting. To take into account both the angle and the height between the transmitter and receiver, the Fourier series can be converted into a double series, so the average path loss with respect to the reference angle θ and height H can be obtained from the following formula:

$$\begin{aligned} L_{[dB]}(\theta, H) =& c_0 + \sum_{i=1}^{I}\sum_{j=1}^{J} c_{i,j} \times \sin\left(\frac{i\pi\theta}{p_\theta} + \frac{\pi}{4}\right) \\ & \times \sin\left(\frac{j\pi H}{p_H} + \frac{\pi}{4}\right) \end{aligned} \tag{3.5}$$

where p_H and p_θ are scaling constants and $c_{i,j}$ is the fitting coefficient, whose value is given by Table 3.4. The main advantages of the proposed model is that it gives the designer a clear idea about the deviation in path loss at various points around the human waist.

TABLE 3.4: Coefficient values for Fourier double series [89]

c(θ,H)	c(θ,1)	c(θ,2)	c(θ,3)	c(θ,4)
c(1, H)	-1986.1652	1398.9216	89.4395	-288.0136
c(2, H)	1876.8755	102.9257	-2333.7691	1310.1936
c(3, H)	-562.7475	-1837.829	3439.0036	-1610.6079
c(4, H)	281.9745	225.708	-773.7729	430.382
c(0,0)	55.2556	-	-	-

3.3.5 Phenomenological In-vivo Path-loss Model

Liu et al. in [90] proposed a model focused on the dependence of loss on distance and frequency, following their studies on developing an in-vivo path-loss model (Part 3.4.4). The authors performed different simulations on an adult male human body of the ANSYS HFSS which had more than 300 organs, by using ANSYS HFSS simulation software. The selected working frequency was in the range of 0.4-6 GHz. Six different dipole antennas which worked at different frequencies were designed and employed to cover the wide range of selected frequencies. A transmit antenna was fixed and located behind the small intestine while the receiver antenna was located at different locations along the x-axis inside, outside and on the body model. In this case they were able to perform a number of loss measurements to develop a mathematical path-loss model for three different in-body, out-body and on-body applications.

According to their study the developed in-body path-loss model is

$$PL_{in-body} = PL_{on-body} + K(d - 78) \tag{3.6}$$

where

$$PL_{on-body} = 22.4f + 31.4 \tag{3.7}$$

Parameter K is the slope of the path loss at each frequency and can be calculated as

$$K = 0.271f + 0.1782 \tag{3.8}$$

From their studies they showed that the in-body path loss increases linearly with distance and frequency, except for the near-field region. In general their model was not

an adequate fit to the measured data in the near-field region.

3.3.6 Statistical Path-loss Model at 400 MHz

Anzai et.al. [40], developed a statistical path-loss model based on FDTD simulation data on a numerical human model in the 400 MHz MICS band to propose a localisation system for the capsule endoscopy scenario. They used a NICT-developed human model with a height and weight of 1.73 m and 65 kg respectively. A transmitter with a dipole antenna with a length of 4 mm was placed at 30 locations inside the human body such as the large and small intestine, stomach and esophagus. Seven dipole receiver antennas with a length of 20 mm were also located on the human body. From the FDTD simulation results, the following two-layer model was extracted to represent the variation in the received signal strength.

$$p(P_r|d) = \frac{1}{\sqrt{2\pi}\sigma P_r} \exp\left[-\frac{\{\log P_r - \mu(d)\}^2}{2\sigma^2}\right] \tag{3.9}$$

where

$$\mu(d) = \log \bar{P}_r \quad ; \quad \bar{P}_r = \alpha d^{-n} \tag{3.10}$$

and α is a constant coefficient which depends on the propagation environment, σ is the standard deviation, d is the distance between the transmitter and receiver and n is the path-loss exponent.

3.4 Deterministic Model

In contrast to the empirical model, a deterministic model, also called the Site-Specific model, is developed based on a theoretical model of radio-wave propagation. These models are more dependent on the propagation environment and need to accurately consider all objects in the propagation area. Thus this model was expected to provide more accurate estimation of path loss than the empirical method [85]. In this section some of the theoretical in-body path-loss models which were proposed for the digestive tract will be reviewed.

3.4.1 Azimuth Angle and Distance Based Path-loss Model

The authors in [91] improved the empirical pass-loss model for the human digestive organs by taking into account the influence of both the distance dependence of signal strength and the orientation of the receiver and the transmitter antennas in their proposed compensated path-loss model. To derive a propagation model, they assumed that a transmitter and receiver using Hertzian dipole antennas were located at distance d from each other. It was assumed that the receiver was just affected by the far-zone field, due to its distance from the transmitter. The proposed propagation model of the Received Signal Electricity (RSE) based on the theoretical analysis can be expressed as

$$\begin{aligned} RSE(d,\theta) = RSE(d_0,\theta_o) - 20n_d \log\left(\frac{d}{d_0}\right) \\ + 20n_\theta \log\left(\frac{\sin\theta}{\sin\theta_0}\right) + S_\sigma \end{aligned} \tag{3.11}$$

where θ denotes the angle between the orientation vectors of the receiver and transmitter antennas, and n_θ and n_d, are the azimuth and distance path-loss parameters respectively. Shadowing is defined by S_σ, which is a Gaussian random variable with a zero mean and variance of σ^2.

The FDTD technique in the SEMCAD simulator was deployed for the numerical analysis of the proposed propagation model and evaluation of the path-loss parameters. The simulation was done at various frequencies including 434 MHz, 868 MHz and 2.4 GHz in the ISM band. Using simulation data of signal attenuation at different frequencies and an empirical propagation model the path-loss exponent n_d was obtained for some tissue layers: Skin, Bone, Fat, Stomach, Lung, Small Intestine and Muscle. The obtained results showed that the path-loss exponent in a given tissue was increased by increasing the frequency.

To further examine the performance of the proposed model in the human body some simulations were also done on the adult male model of the National Institutes of Health (NIH) in SEMCAD at 434 MHz, when an implant source was located at the bottom of the stomach and a transmitter sensor was located in the close vicinity of the phantom's abdomen. The results showed that the minimum error in loss can be achieved when the azimuth path-loss parameter (n_θ) is set to 3. More importantly, the average error RSE for the empirical model was 40 dB, whereas the error was about only 20 dB for the proposed model. In general, simulation results proved that the proposed propagation model had a superior performance to the empirical propagation

model since, in this novel model, including the azimuth parameter can provide more accurate results, particularly for the gastrointestinal region.

3.4.2 RF Absorption Based Path-loss Model

Wang et al. [92] studied the RF absorption characteristics in the human body to achieve a highly accurate RSS-based localisation system. They claimed that the traditional propagation loss model is inadequate for loss estimation inside the human body in the fading channels situation. For this purpose, they proposed an EM propagation model and compared it with FDTD measurement simulation to examine the proposed model. The novelty of their model was in considering, not only the distance dependence of the signal strength and the impact of antenna orientation, but also taking into account the tissue absorption to built an attenuation model.

To analyse radio propagation inside the body, the Specific Absorption Rate (SAR) was first calculated at four different frequencies: 434 MHz, 868 MHz, 1.2 GHz and 2.4 GHz of the ISM band. The SAR is the amount of absorbed power per mass of tissue. Therefore the total loss between a transmitter and a receiver can be obtained by calculating the average SAR over the entire selected tissue mass. In order to calculate the average SAR in a high-loss medium, one can benefit from Maxwell's H-field and E-field equations. The SAR in the Near-field and Far-field cases can be calculated by the following formula.

In the near-field condition

$$SAR = \frac{\sigma}{\rho} \frac{\mu\omega}{\sqrt{\sigma^2 + \epsilon^2\omega^2}} \frac{I^2 l^2}{16\pi^2 R^4} \sin^2\theta \tag{3.12}$$

where ρ is the density of the medium, I is the effective current through the transmitted antenna, l is the length of the antenna, R is the length of the vector from P_t to P_r, θ is the angle between the orientation vectors of the transmitter antenna and the R vector. μ, ϵ and σ are respectively the permeability, permittivity and conductivity of the medium at a frequency of ω.

In the far-field condition

$$SAR = \frac{\sigma}{\rho} \frac{\beta^2\eta^2 I^2 l^2}{16\pi^2 R^2} \sin^2\theta \tag{3.13}$$

$$\beta = \frac{2\pi}{\lambda} \qquad \eta = \sqrt{\frac{\mu}{\epsilon}}$$

where ρ is the density of the medium, β is the phase constant and η is the medium's intrinsic impedance.

Hence, in the proposed EM propagation wave model, the amount of power absorbed by each tissue can be calculated from the power-loss density as follows:

In the near-field condition

$$\bar{S} = \bar{E} \times \bar{H} = \frac{1}{\omega\epsilon} \frac{I^2 l^2}{16\pi^2 R^5} \sin^2\theta \boldsymbol{a_r} \tag{3.14}$$

and in the far field condition

$$\bar{S} = \bar{E} \times \bar{H} = \frac{1}{\omega\epsilon} \frac{I^2 l^2}{16\pi^2 R^2} \sin^2\theta \boldsymbol{a_r} \tag{3.15}$$

Then RSS can be obtained from the EM propagation model from

$$P_R = S - K \cdot \frac{dP_R}{dV} \tag{3.16}$$

where V is the volume of the tissue and K denotes a constant that depends on the absorption tissue length.

To evaluate the in-body propagation loss for an implant source inside the human body, FDTD simulations were performed with the SEMCAD simulator in homogeneous and heterogeneous media at the aforementioned frequencies. The assumed medium for homogeneous tissue simulations were fat, small intestine and stomach. Hertzian-dipole antennas were used for the transmitter and receiver, fed with a sinusoidal voltage of 1 V. The amounts of power attenuation obtained from the FDTD simulation were then compared to the numerical results of the EM propagation model. The root-mean-square error (RMS) calculation of the two methods reveals that the proposed model error is less than 6 dB.

The simulations were also done in the heterogeneous medium of an adult male model using Visible Human Body. In this case, the source was placed near the bottom of the stomach in the digital phantom. However, the proposed EM model was not

quite accurate for plane estimation, so the evaluation was performed in one slice only. The RMS result for this step also revealed an error of less than 4 dB for the proposed EM model. Overall, the suggested EM model was in correspondence with the FDTD measurement simulation.

3.4.3 Adaptive Path-loss Model

Ramezani et al. [93] derived a novel in-body path-loss model for the GI tract by considering the permittivity, conductivity and thickness of different tissue layers of the abdominal wall. For this purpose the abdominal wall was modelled as a multilayer medium and then the time-average power at each location inside the medium was derived as well as the total reflected power. The time-average power can be calculated as

$$P_{av}(z) = \frac{1}{2Re(\eta)} |E_{+}(Z)|^2 = \frac{1}{2Re(\eta)} e^{-2\alpha z} \tag{3.17}$$

where $\eta(z)$ is the characteristic impedance of the nonmagnetic material and α is the attenuation constant. Therefore PL can be obtained from

$$PL_{dB} = 10 \log P_{av}(d) - 10 \log P_{av}(d_0) \approx -20 \log e^{-2\alpha d} \tag{3.18}$$

where d is the distance between the transmitter and receiver and the power at distance d_0 was assumed to be 0 dB.

Further the performance of the Adaptive path-loss model was evaluated by Monte Carlo simulation. According to their obtained results, the standard deviation of the error in the path-loss model is 50% smaller than for existing channel models. According to their study on different tissue thicknesses they claimed that the fat layer has the greatest influence on the total attenuation, therefore they modified their proposed model accordingly.

3.4.4 In-Vivo Path-loss Model

The authors in [94] proposed a theoretical in-vivo path-loss model focused on the abdominal cavity. The path-loss model was expressed in spherical coordinates. They believed that because the in-vivo environment is a heterogeneous medium, it needs to be analysed in a Spherical coordinate system rather than other coordinate systems.

The path loss can be calculated as

$$PL_{(r,\theta,\phi)} = 10\log_{10}\left(\frac{|E|^2_{r=0}}{|E|^2_{r,\theta,\phi}}\right) \tag{3.19}$$

where r, θ and ϕ are the radius, polar angle and azimuth angle in spherical coordinates respectively. $|E|^2_{r=0}$ and $|E|^2_{r,\theta,\phi}$ represent the magnitudes of the E field at the origin and the measuring point respectively.

The authors performed several simulations on the male human body of ANSYS HFSS 15.0.3 using ANSYS HFSS simulation software, with a hertzian dipole and monopole antennas, to investigate the dependence of the loss on parameters such as r, θ, ϕ and operating frequency. However the performance of the proposed model was not compared with any obtained data from the simulations. The authors stated that this is a preliminary work in building an in-vivo channel model.

Moreover, Liue et al. in [90] developed a different path-loss equation in Cartesian coordinates. The developed path-loss model is based on the fact that the return loss of antennas which are being employed for body applications varies with location and working frequency. Therefore in their developed model the effect of antenna gain was ignored. The proposed model is

$$\begin{aligned} PL(dB) = -S_{21} &+ 10\log\left(1 - 10^{\frac{S_{11}}{10}}\right) \\ &+ 10\log\left(1 - 10^{\frac{S_{22}}{10}}\right) \end{aligned} \tag{3.20}$$

where S_{21} represents the power gain between transmitter and receiver antennas, and S_{11} and S_{22} are the return losses of the two aforementioned antennas. As with the previous path-loss model in Equation 3.19, the authors did not evaluate the performance of the proposed path-loss model.

3.5 Semi-deterministic Model

A semi-deterministic model, also known as a Semi-empirical model, can be derived by performing some empirical modification to the deterministic models to improve the agreement of model with measurement. In fact this model suggests a fundamental trade-off between deterministic and empirical models; the semi-deterministic models are more accurate than the empirical models due to considering some deterministic factors [85, 95].

3.5.1 Tissue Dielectric Properties Path-loss Model

In [96], the authors took different approaches to develop a path-loss model for capsule endoscopy. In this study a set of X-ray images from Computed Tomography (CT) was deployed to determine the thickness and dielectric parameters of the patients' tissues. In fact, in this method human tissue properties based on CT values were categorised into five groups: Air, Fat, Tissues, Bones and Water. Thus a single-layered model can be assumed for the human body instead of its multi-layered characteristic. Also an average conductivity and relative permittivity need to be assigned in the loss equations. Then the path loss can be easily calculated by assuming a two-layer model (air and body layer) and tissue dielectric parameters acquired from the CT images.

To develop a path-loss model and be able to do the measurements, a fabricated small-signal generator (SG) with a diameter of 11 mm $\times$ 18 mm was placed in the esophagus and duodenum of a human volunteer. The test was done at two working frequencies, 403 MHz (MICS band) and 2.4 GHz (ISM band). An appropriate body-worn antenna was also used as a receiver for each frequency, separated 15 mm from the body surface. In the next step, a set of CT images was taken with different positions of the body-worn antenna. The main purpose of exposing patients to X-rays is to obtain the content of the human tissue by counting the CT values in pixels along a line between the in-body source and the external antenna. The propagation loss can then be calculated through a simple two-layer model that includes body layer and air layer. The dielectric values for the in-body layer can be extracted from these formula:

$$\bar{\epsilon_r}(f,p) = \frac{1}{N}\sum_{i=0}^{4} \epsilon_{ri} N_i(f,p) \tag{3.21}$$

$$\bar{\sigma_r}(f,p) = \frac{1}{N}\sum_{i=0}^{4} \sigma_i N_i(f,p) \tag{3.22}$$

where $N_i(f,p)$ indicates the number of pixels of each category in its specific position p and frequency f. N is the total number of pixels in the CT image. The thickness of the in-body layer can be obtained from the CT image, whereas the thickness of the out-body layer (air) was set to 15 mm. Based on this model the path loss can be calculated as follows.

$$L_{air} = 20\log_{10}\exp(-\alpha_{air}.d_{air}) \tag{3.23}$$

$$L_{body} = 20\log_{10}\exp(-\alpha_{body}.d_{body}) \tag{3.24}$$

where α_{air} and α_{body} are the attenuation coefficients for the air and human body tissue layers respectively. Moreover the reflection loss caused by the tissue boundary should be calculated as well. The reflection loss can be obtained from

$$L_r = 10\log_{10}\left|\left(\frac{2\alpha_{air}}{\alpha_{body}+\alpha_{air}}\right)^2\frac{Z_{body}}{Z_{air}}\right| \tag{3.25}$$

where

$$Z_{air} = \frac{j\omega\mu}{\alpha_{air}} \qquad Z_{body} = \frac{j\omega\mu}{\alpha_{body}}$$

To evaluate the proposed path-loss model, some loss measurements were done with similar scenarios and then the results of the calculated loss by the two-layer method were compared to the results of the path-loss measurements. Although some errors were observed in this comparison, generally the two-layer method results were in good agreement with the measured results. The errors mostly happened when the propagation medium included more tissues, since in CT categories tissues are dedicated a single relative permittivity and conductivity, whereas in reality each tissue has its own characteristics. Overall, a difference of less than 6 dB was achieved for the measured and estimated results.

3.5.2 Semi-empirical Path-loss Model at 402 MHz

In [97], the authors made a comprehensive numerical analysis of the path loss for in-to-out body communication focused on capsule endoscopy at 402 MHz. They conducted several simulations on a homogeneous medium and three human phantom models (named Duke, Thelonius, Fats) using the SEMCAD X solver and applying the FDTD method. A spiral antenna that was fitted inside a capsule endoscope and a half-wave dipole antenna were used as the transmitter and receiver antennas respectively. According to their simulation setup with two-port circuits the path loss, which

is defined as the ratio of the input power (P_{in}) in port 1 to the received power (P_{rec}) at port 2, can be expressed as :

$$PL_{|dB} = \frac{P_{in}}{P_{rec}} = -10\log|S_{21}|^2 = -|S_{21}|(dB) \tag{3.26}$$

The authors applied the semi-empirical path-loss equation, which is based on the Friss formula, into their analysed data to model the path loss between transmitter and receiver antennas.

$$PL_{dB}(d) = PL_{0,dB} + 10n\log(\frac{d}{d_0}) = -|S_{21}|(dB) \tag{3.27}$$

where $PL_{0,dB}$ is the path loss at a reference distance of d_0, equal to 259 mm in their study, and n is the path-loss exponent and is strongly dependent on the medium through which the propagation takes place. It should be mentioned that the authors considered the antennas part of their channel model because, when the human body is located in the near field of an antenna, a single radiating system would be created by charges on both the human body and antenna. Therefore it is not possible to ignore the impact of the antenna and human body on each other [98].

The values of n and PL_0 which were obtained by using linear regression fitting (Equation 3.27) on simulated data are listed in Table 3.5.

Table 3.5: Parameters for path-loss models for heterogeneous phantoms

Configuration	**PL_(0,dB)**	**n**	σ
Thelonius (child)	49.77	7.91	1.97
Duke (adult)	56.83	7.1	2.99

In addition, they studied the effect of misalignment between antennas and the rotation of the antenna on the path loss. They observed an increase in loss when there is a misalignment between transmitter and receiver antennas as well as with rotation of the antenna.

3.5.3 Biotelemetric Path-loss Model

The authors in [99] conducted a comprehensive numerical and experimental analysis of radio channel and attenuation on a human subject with ingested implants at frequencies of 402 MHz, 868 MHz and 2.4 GHz. For this purpose the Computer Simulation Technology (CST) Microwave Studio solver with Finite Integral Technique (FIT) was

employed to perform several simulations on an adult male model from the National Institutes of Health (NIH) Visible project which had a 3-mm resolution. The focus of this study was on the stomach region in two specific cases: empty and full stomach models. For the measurements, a human phantom with a height of 1.7 m and width of 0.35 m was used while animal (sheep) organs such as liver, lungs and heart were applied inside the human phantoms. A sheep's heart was used instead of a human stomach since its dielectric properties are so close to those of the human stomach.

The authors stated that in many theoretical studies the average received signal decreases logarithmically with distance. So the path loss between a transmitter and receiver as a function of distance can be expressed as

$$PL(d) \propto \left(\frac{d}{d_0}\right)^{\gamma} \tag{3.28}$$

Therefore the path loss in dB can be calculated as:

$$PL_{dB}(d) = PL_{0,dB} + 10\gamma \log(\frac{d}{d_0}) + X_{\sigma} \tag{3.29}$$

where X_{σ} is a zero-mean Gaussian distributed random variable with a standard deviation of σ. The path-loss exponent of γ was obtained from experimental and numerical analysis by applying an empirical linear power law and least-square fitting techniques to the obtained data. Table 3.6 summarises the value of γ at each frequency.

As can be seen in Table 3.6, the path-loss exponents obtained by measurements and numerical analysis are slightly different at each frequency because the dielectric properties of the human and animal are not completely similar.

TABLE 3.6: Simulated and measured path-loss exponents at different frequencies

Frequency	**Simulated γ**	**Measured γ**
402 MHz	1.85	1.9
868 MHz	1.9	2
2.4 GHz	2.60	2.80

3.6 Challenges of In-body Path-loss Modeling

The aforementioned proposed in-body path-loss models focused on the GI tract are summarised in Table 3.7. Modelling an accurate radio channel for in-body communication is a challenging task. This is because the human body has a complex structure and each human tissue has its own electrical properties which highly impact the propagation of electromagnetic waves. Another important issue for in-body path-loss modelling is related to the distribution of tissues. Tissue distribution is not uniform in the entire human body and is also greatly dependent on the age, sex and size of the human. On the other hand, body posture and body movement are other factors that can significantly degrade the in-body communication link. Moreover, there is still a lack of physical measurements and analysis on a real human body due to technical and ethical issues. Therefore most studies are focused on numerical simulations of electromagnetic wave propagation through the human body by applying different digital anatomical human phantom models. One controversial issue about different human phantom models is that they are mainly developed from MRI images with different resolutions. Thus in some parts of the human body like the small intestine those models are not able to provide the desired resolution and full details of such a complex organ. This can impose some constraints and inaccuracies on the obtained data from the simulations. Although in some studies the authors claimed that the simulation results can be considered as a good estimation, in some performance analysis such as localisation accuracy the error in the path-loss model can highly affect the system performance. Overall, performance evaluation of each method, identification of their fundamentals and knowledge of their theoretical limits will open up a deeper insight into the issues and challenges of current and future studies in this area and give a new direction to take advantage of existing techniques to achieve a highly accurate capsule localisation system.

3.7 Chapter Summary

In this chapter we reviewed a number of proposed channel models focused on the abdomen area. The discussion about their development methods and characteristics as well as their drawbacks is also provided. This study can be significantly beneficial for developing a location estimation system based on the RSS method, since the improvement of the accuracy of RF-based localisation techniques in the GI tract depends critically on the radio propagation inside the human body, specifically in the human

Table 3.7: Summary of proposed in-body path-loss models mainly for GI tract

Reference	Model Category	Simulation Software	Frequency	Phantom Type	Model Dependency	Concerns
[86]	Empirical	HFSS	403.5 MHz	-	Distance	-Just considers the distance between transmitter and receiver -Omnidirectional radiation pattern was assumed -No discussion on loss in near-field case
[87]	Empirical	SEMCAD X	2.45 GHz	6-year child from virtual family	Distance	-Maximum distance of implant was 8 cm -No discussion on loss in near-field case
[88]	Empirical	SEMCAD X	403.5 MHz	-Japanese male -Liquid Phantom	Distance and angle	-No discussion on loss in near-field case
[89]	Empirical	-	3.4-4.8 GHz	Voxel anatomical model of NLM	Distance and angle	-No discussion on loss in near-field case
[90]	Empirical	HFSS	3.4-6 GHz	Adult male	Distance and frequency	-The model not adequately fitted to the data in near field
[40]	Empirical	-	400 MHz	NICT human model	Distance	
[91]	Deterministic	Verified by SEMCAD X	434 MHz 868 MHz 2.4 GHz	Adult male from NIH	Distance and angle	-Far-field was the only assumption
[92]	Deterministic	Verified by SEMCAD X	434 MHz 868 MHz 1.2 GHz 2.4 GHz	Adult male from visible human body	Distance, angle and tissue absorption	-
[93]	Deterministic	-	-	-	Thickness of tissue layer	-Dependence of the model on the different layers' thicknesses
[94]	Deterministic	HFSS	-	Male human model of Asys HFSS 15.0.3	Radial distance and angle	-The performance of the model was not compared with simulation results
[90]	Deterministic	-	-	-	S_{11} & S_{22}	-
[96]	Semi-deterministic	-	403 MHz 2.4 GHz	-	Distance, frequency and tissue absorption	-
[97]	Semi-deterministic	SEMCAD X	402 MHz	Three human models (Duke, Thelonius and Fats)	Distance	-
[99]	Semi-deterministic	CST	402 MHz 868 MHz 2.4 GHz	Adult male solid phantom from NIH (visible project)	Distance	-No discussion on loss in near-field case -Animal organs with different dielectric properties were used inside the phantom

abdomen area.

4

Radar Technique for In-body Localisation

4.1 Introduction

As discussed in Chapter 2, a radar system has been selected for our location estimation method to determine the capsule position in the GI tract at each instant. Selecting the optimum working frequency for our radar system is not straightforward, since the system should work in the vicinity of the human body. Therefore the right working frequency should be chosen to address both the safety issue for the human body and providing higher resolution in terms of location estimation. Apparently each operational frequency has its own specific characteristics and can behave differently depending on the propagation condition. Using these characteristics can help us to determine the best possible working frequency to suit our application. This chapter aims to provide a detailed analysis of the selected frequencies to investigate their suitability in radar performance for in-body application.

The growing demand for communication services requires various wireless networking technologies to be developed. In general, any wireless technology can be used in eHealth (electronic management of health information) depending on the specific application, its safety, data rate and quality of service (QoS). However, in the last few years

high-data-rate wireless technologies, such as ultra-wideband (UWB) and millimetre-wave (mmWave), have attracted more attention. The unlicensed 60 GHz mmwaves provide one of the largest bandwidths, making this technology attractive for medical applications. It will also make it possible to perform a high level of miniaturisation for the antennas and transceiver circuits and will have low interference effects on other wireless systems in the same environment. Therefore at the beginning of this chapter we provide a brief review of 60 GHz mmwaves and their suitability for radar systems for WCE location estimation. Then we will continue our discussion on investigating the most suitable and appropriate frequencies in the range of UWB for radar operation as 3.4 GHz, 4.8 GHz and 5.8 GHz. We also compare the results of radar performance against a narrow-band radar operating in the 2.4 GHz ISM band.

4.2 60-GHz Millimeter-Wave Wireless Technology

Recently the requirement of supporting a high data rate in several different radio communication applications has encouraged employing the extra-high-frequency band. In this case the 60 GHz frequency band has been recognised the most appropriate band for supporting short-range applications due to its specific propagation characteristics. Moreover the high data rate that can be achieved in this frequency band can be considered as a proper replacement of fibre optics in some applications. One of the most important propagation characteristics of the 60 GHz band is its high level of absorption and attenuation by atmospheric gases such as oxygen and water vapour. On the other hand systems at 60 GHz are absolutely vulnerable to rain attenuation. This is mainly because the size of raindrops is nearly the same as the wavelength that causes scattering of a radio signal [6]. Figures 4.1 and 4.2 show the specific attenuation of a signal due to atmospheric gases and rain as function of frequency.

As can be seen in Figure 4.1 there is a peak in oxygen absorption near 60 GHz. Based on the ITU-radiowave propagation report (Rec. ITU-R P.676-10), the sea-level attenuation is generally around 16 dB/km. In Figure 4.2 it can be also seen that during heavy rain (over 150 mm/h) the specific attenuation can exceed 40 dB/km. Even though these effects strongly limit the range of communication at this frequency, it supports a considerable level of frequency re-use, which is tempting for a variety of short-range applications.

Owing to the specific characteristics of radio propagation at 60 GHz and its supporting data rate the regulatory bodies arranged to use this frequency band in different

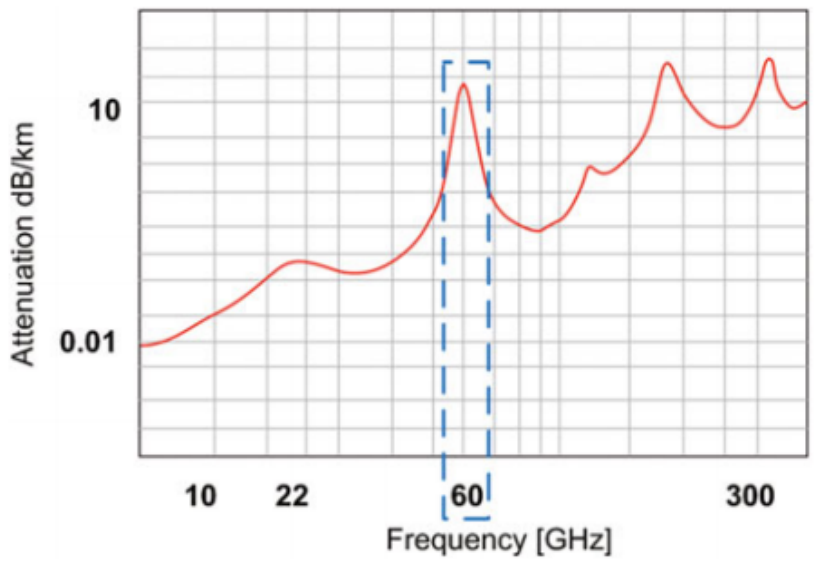

Figure 4.1: Attenuation due to oxygen absorption in 60 GHz band [5]

countries. According to the Federal Communications Commission (FCC) the frequency band from 59-64 GHz is assigned as an unlicensed band due to the limited potential for interference [100]. Some potential applications using the 60 GHz frequency band can be listed as high-speed file exchange, multimedia and entertainment systems, security, surveillance and biomedical applications.

In the last few years some interest has been raised regarding deploying 60 GHz wireless technology for health-care applications because of some significant advantages that this frequency can offer, such as the largest bandwidths, low electromagnetic interference (EMI) effects in the medical environment, small antennas, and high-data-rate communication. According to the spectrum allocation, the band 61.0-61.5 GHz is nominated for non-radio communications in industrial, scientific and medical (ISM) applications subject to special authorisation by the administration concerned.

For this purpose some studies have been conducted to identify the possibility of using this band in medical applications as well as its related challenges and restrictions. The authors in [101, 102] reported significant results for implementation of BANs at 60 GHz for on-body and off-body scenarios. Interestingly it was stated in [102] that the antenna performance was not influenced by the presence of the human body, even though there was a small distance between the antenna and the body. In [103] and [104] a channel model for on-body application has been investigated .Some primary results of path gain have been presented in [105]. The authors in [106] and [107] have

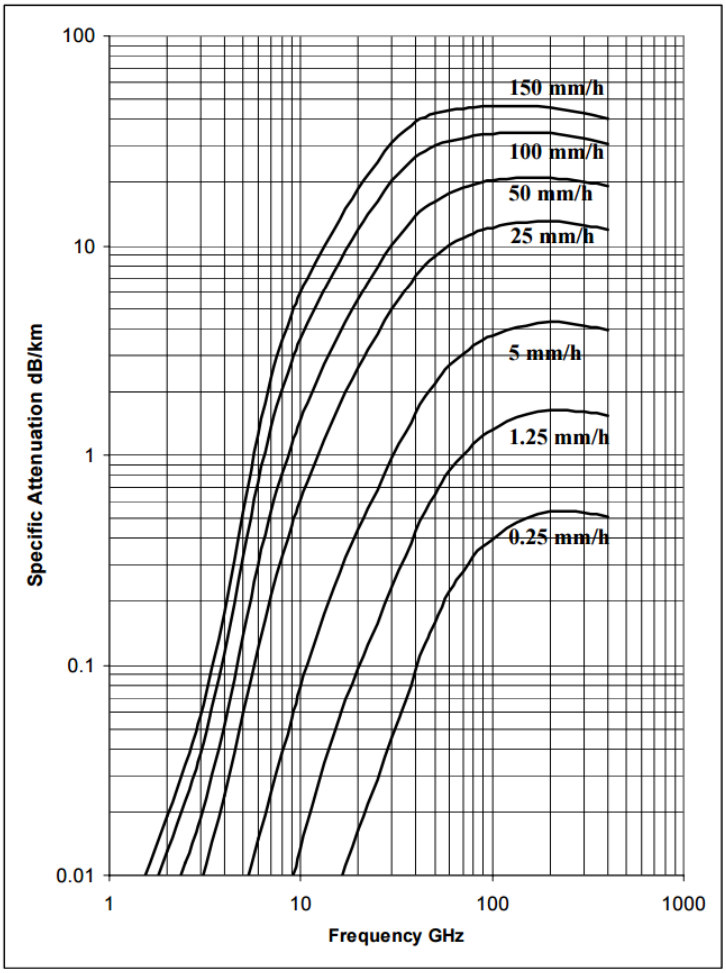

FIGURE 4.2: Rainfall attenuation vs frequency [6]

studied the static propagation model for off-body and on-body communication at 60 GHz. To be able to verify any plane-propagation models at 60 GHz a skin phantom model has been proposed in [108]. Based on the author's knowledge no studies have been reported regarding applying 60 GHz frequency for in-body applications. In this work I have also investigated the possibility of using 60 GHz in localisation of a capsule endoscope inside the small intestine.

4.3 Suitable Frequency for a WCE Radar Localisation System

Finding the best possible working frequency is one of the most important factors in designing a radar system. Although working at a higher frequency for in-body applications encounters higher signal attenuation by different tissue layers, higher resolution in location estimation of the capsule can be achieved at these frequencies. Therefore we should emphasise the importance of compromise between signal attenuation and higher resolution in location estimation at higher frequencies.

To explore the radar performance, a detailed analysis has been done to investigate the effect of varying thicknesses of the body tissues on the signal attenuation and the received power at the aforementioned frequencies.

The interior of the human abdomen is considered as the propagation channel since the signal should pass through the abdomen area to reach its desired target in the small intestine. A layered planar model as shown in Figure 4.3 was used to demonstrate the propagation channel of the abdomen area.

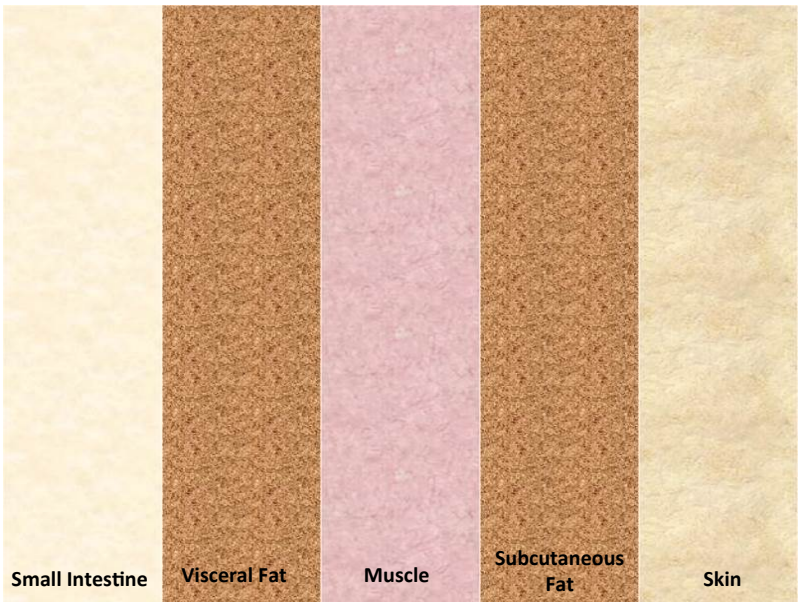

Figure 4.3: Multilayer planar human tissue model

As can be seen in this figure, two types of fat are considered for the propagation channel. Visceral fat refers to the fat in the abdomen cavity and between the organs, whereas subcutaneous fat refers to the fat found just beneath the skin. These layers

have different thicknesses and can vary by age and sex. Table 4.1 tabulates the thickness of these different layers in a female subject. In this table the tissue is divided into low, mid and high tertile categories based on visceral fat [109–112].

TABLE 4.1: Abdomen Tissue Thickness

Tissue	Range of thickness (mm)		
	Low tertile	Mid tertile	High tertile
Visceral fat	15-36	37-47	47-98
Subcutaneous fat	17-34	17-34	20-33
Abdomen muscle	8-16	8-16	8-16
Skin	1.1-1.6	1.1-1.6	1.1-1.6

Table 4.2 summarises the dielectric characteristics of the different tissue layers at these frequencies. These properties have been obtained from [113]. It can be seen that the small intestine and the abdomen muscle have the largest relative permittivity at all frequencies. We assume that the radar transmitter is located above the hip (Figure 4.4).

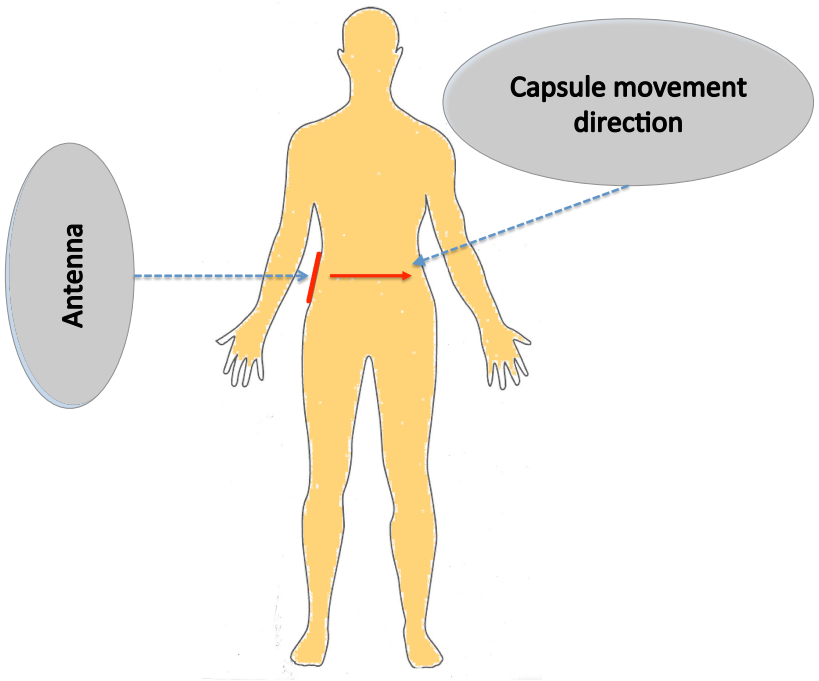

FIGURE 4.4: Antenna position on the human body

Table 4.2: Properties of human abdomen tissue at different selected frequencies [113]

Frequency	Tissue name	Conductivity [S/m]	Relative permittivity	Loss tangent	Wavelength [m]	Penetration depth [m]
2.4 GHz	**Fat**	0.10235	5.2853	0.14503	0.054193	0.11956
	Muscle	1.705	52.791	0.24191	0.017069	0.022785
	Skin Dry	1.4407	38.063	0.2835	0.02005	0.022956
	Small Intestine	3.1335	54.527	0.43042	0.016553	0.012785
3.4 GHz	**Fat**	0.15028	5.1839	0.15326	0.038615	0.080667
	Muscle	2.4709	51.568	0.25333	0.012183	0.01555
	Skin Dry	1.9655	37.092	0.28016	0.01434	0.016607
	Small Intestine	4.0128	52.66	0.40287	0.01192	0.009786
4.8 GHz	**Fat**	0.22993	5.048	0.17058	0.027698	0.052061
	Muscle	3.8279	49.8	0.28785	0.008762	0.0098858
	Skin Dry	2.9076	35.936	0.30299	0.010304	0.011067
	Small Intestine	5.5166	50.306	0.41067	0.0086327	0.0069623
5.8 GHz	**Fat**	0.29313	4.9549	0.18335	0.023125	0.040481
	Muscle	4.9615	48.485	0.31715	0.0073337	0.0075413
	Skin Dry	3.717	35.114	0.32807	0.0086106	0.0085735
	Small Intestine	6.7459	48.672	0.42955	0.0072505	0.0056102
60 GHz	**Fat**	2.8152	3.1324	0.26925	0.0027983	0.0033671
	Muscle	52.826	12.856	1.231	0.0012255	0.00040973
	Skin Dry	36.397	7.9753	1.3673	0.0015245	0.00047805
	Small Intestine	51.996	12.005	1.2976	0.0012556	0.00040629

It transmits a nominal 1 mW (0 dBm) reference power level, which needs to pass through the human abdomen until it reaches the capsule endoscope inside the small intestine. The incident signal will then be reflected through the human body, and a receiver, which is also co-located with the transmitter, will collect the reflected signal. Then the capsule location can be computed with respect to the received signal strength, and an appropriate tracking algorithm correlates the change in signal strength with the capsule distance. The algorithm itself is beyond the scope of this chapter.

To calculate the relative power at receiver, the absorption and reflection loss are considered as the dominant mechanism of signal attenuation. The transmitter and receiver are assuming to be co-located on the human body for simplicity (Figure 4.4). So, there is no need to calculate the free space loss. The two main losses can be computed as follows using basic wave propagation theory.

$$P_L(d) = e^{-\alpha d} \tag{4.1}$$

$$PL(n) = 20log\,|\Gamma| \tag{4.2}$$

Here α is the absorption coefficient, d is the traveled distance in the tissue and Γ is reflection coefficient, Figure 4.5 shows the calculated power loss at the receiver side versus different locations of the capsule, at 60 GHz. As can be seen the power loss is significantly high, which confirms that the high-frequency signals can be dramatically attenuated by human tissues. Moreover, since the focus of the radar signal is capsule endoscopy inside the GI tract, the signal passes through different tissues such as muscle and fat which have a significant signal attenuation. Furthermore, the existence of water and gas inside the GI tract can be another reason for such an attenuation inside the body. Therefore this frequency is not necessarily applied for in-body applications due to extreme attenuation by different tissues layers.

Figure 4.6 demonstrates the relative power at different UWB and ISM band frequencies. As can be seen, the relative power with a 2.4 GHz radar system is higher than at other frequencies. This result is not far from our expectation, since human tissues have higher dielectric values at higher frequencies and so produce a larger loss. The received power variation due to the small movement of the object is an important

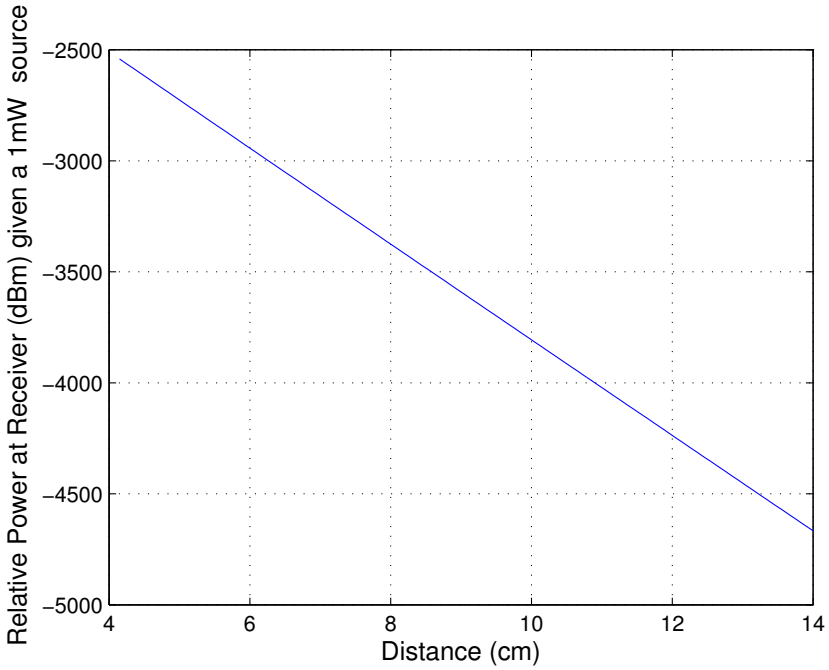

Figure 4.5: Calculated power loss at receiver versus distance at 60 GHz

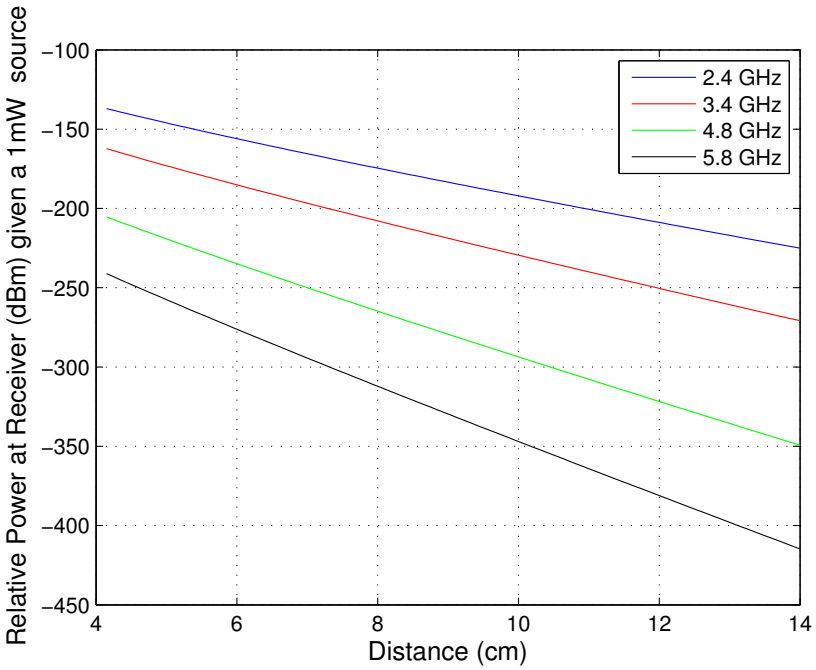

Figure 4.6: Calculated power loss at receiver versus distance

factor in localisation, since it can provide higher resolution in a localisation system. Basically the resolution quantifies the closest locations of the capsule that can be resolved by the receiver. To compare the desirability of the selected frequencies in the GI localisation system and evaluate the system performance, the received power-loss variation with respect to a 1 mm movement of the capsule was plotted for the four frequencies (Figure 4.7).

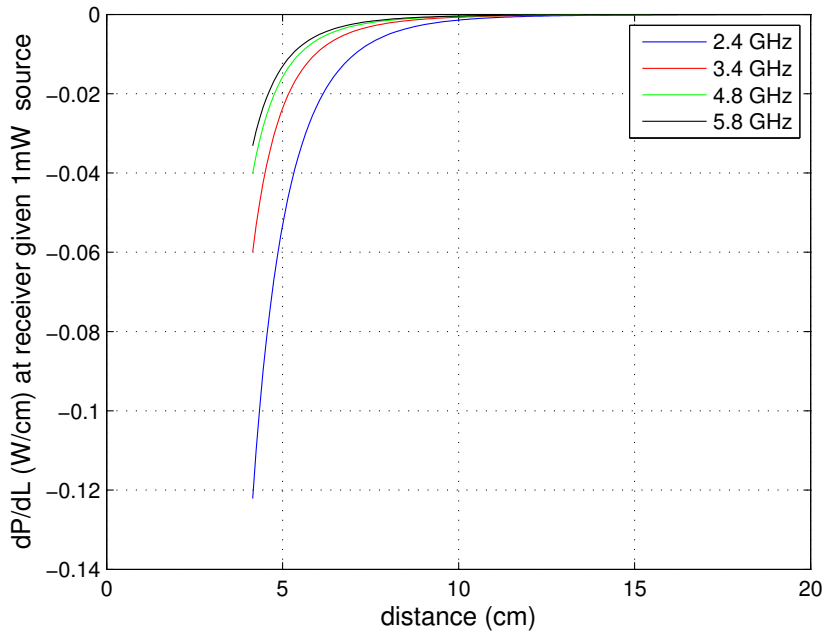

FIGURE 4.7: Power variation due to 1 mm movement of capsule endoscope

It can be seen from Figure 4.7 that the variation of power in response to capsule movement is more significant at 2.4 GHz, followed by 3.4 GHz, 4.8 GHz and 5.8 GHz. On the other hand, far from the antenna the received power variations decrease dramatically, with the loss increasing with distance. To simplify the discussion, the data were extracted from the above plots for 1 cm of capsule movement. Table 4.3 presents the obtained variation of power with respect to a 1 cm movement of the capsule.

Table 4.3 shows that, for the 1 cm movement of the capsule at 2.4 GHz, the received power variation is more likely to be recognised by the receiver than at the other frequencies. However, the probability of detection can be improved by deploying a highly sensitive receiver. Overall, the system at 2.4 GHz can provide better resolution, since it has a higher detectable fluctuation in the received power with a small amount of

Table 4.3: Received power variation at different frequencies

Frequency	Received power variation with respect to the 1cm movement (W/cm)
2.4 GHz	0.0757
3.4 GHz	0.0395
4.8 GHz	0.0265
5.8 GHz	0.0218

capsule movement.

4.4 Performance Consideration of the Radar System

As can be seen in Figure 4.6, the attenuation of the signal is high at all frequencies. Since a radar system is going to be used, the two-way attenuation needs to be considered. To detect such a noiselike signal, the employed receiver needs to have a sensitivity of about -150 dbm. GPS receivers are a good example of highly sensitive receivers [114]. However there is a trade-off between the high sensitivity and the positioning accuracy for GPS receivers [115].

In a radar system, the receiver sensitivity can be obtained from the following equation:

$$S_{min} = kTB \times F \times SNR \tag{4.3}$$

Here k is the Boltzmann constant, B is the system bandwidth in Hz, T is the room temperature (around 300 Kelvin) and F is the noise figure (about 6 dB). Also, according to FCC regulations at 2.4 GHz, if the frequency-hopping spread spectrum technique is applied then each channel can have a 1 MHz bandwidth. Therefore, the resulting SNR would be -42 dB. To increase the detection probability of such a low-SNR signal, coherent or non-coherent pulse integration can be used in the receiver. In coherent integration the return signals from the target are added in the receiver before the envelope detection process, whilst in the non-coherent method integration is performed after the envelope detection process or demodulation. In practice coherent integration can provide better performance than non-coherent integration. However, having an accurate knowledge of the target radial velocity, high phase stability in the transmitter,

the propagation path and the reflected signal is a crucial requirement for this method. Therefore, if any of these conditions are not met then non-coherent integration is a possible choice, with a lower processing gain and simpler implementation [68].

In addition, the SNR can be calculated from the following equation:

$$SNR = \frac{PGA\tau\sigma}{(4\pi)^2 R^4 kTB} \tag{4.4}$$

Here P is the transmitted peak power, A is the effective aperture area of the receiver antenna, G is the gain of the antenna, R is the range from the radar to the target, σ is the radar cross-section and τ is the transmitted pulse width. This equation shows the dependency of the SNR on several parameters. Among those parameters τ plays an important role in radar performance. Increasing the pulse width not only improves the SNR but also can increase the radar range resolution ($\triangle R = c\tau/2$) [68].

4.5 Chapter Summary

In this chapter, the possibility of using a radar system for capsule localisation is investigated at frequencies of 2.4 GHz, 3.4 GHz, 4.8 GHz, 5.8 GHz and 60 GHz. Before any deployment of a radar system we need to consider the existing challenges in the system. One of the most important challenges is selecting an appropriate operating frequency. The choice of a suitable working frequency usually is a tradeoff among several aspects such as atmospheric attenuation, transmitted power and physical size. Moreover a suitable frequency not only needs to provide a higher accuracy in terms of location estimation, but also to encounter less loss for in-body communication. This chapter first presented an overview of the 60 GHz frequency, which has recently attracted more interest for different medical applications and was one of our candidate frequencies for the radar system. It then explored the best possible frequency for our radar system. Our study shows that the system at higher frequencies faces higher loss, since the absorption loss in different tissues is significant at high frequency. Among the studied frequencies, 2.4 GHz has lower loss, however the received power loss even at this frequency will fall below the expected noise floor. To address this issue, deploying a highly sensitive receiver should be considered. Our results also show that the system at 2.4 GHz can provide better resolution for localisation purposes, since the variation in the received power is much more significant for a small movement of the capsule than for the other frequencies.

Publications pertaining to this chapter:

- P. Arab, M. Heimlich and E. Dutkiewicz, "Investigation of radar localization system accuracy for human gastro intestine (GI) tract," *Medical Information and Communication Technology (ISMICT), 2013 7th International Symposium on*, Tokyo, 2013, pp. 144-148.

- P. Ara, M. Heimlich and E. Dutkiewicz, "Investigation of radar approach for localization of gastro intestinal endoscopic capsule," *2014 IEEE Wireless Communications and Networking Conference (WCNC)*, Istanbul, 2014, pp. 99-104.

5

On-Body Antenna at 2.4 GHz

5.1 Introduction

One of the major challenges in a WBAN is designing an antenna which can perfectly address the requirements of different communication links. In general, WBAN communications can be divided into three main categories:

1. Intra-WBAN Communication
2. Inter-WBAN Communication
3. Beyond-WBAN Communication

Therefore to provide a robust and satisfactory level of communication in a WBAN, an efficient antenna should be designed according to the characteristics of each communication link. In general, antennas for WBANs can be classified into two groups: In-body antennas and On-body antennas. Antenna design for any WBAN application can be a challenging task as the antenna needs to be small, efficient and not influenced by the user's body. One of the challenges in designing a WBAN antenna is in adjustment of the designed antenna according to the shape of the human body. Since most

antennas are built on top of a substrate, it is not easy to adjust the antenna, suggesting a flexible or textile antenna [116].

The electromagnetic interaction between the antenna and the human body is another major challenge in designing an antenna in a WBAN. Unlike the standard communication in free space, the human body is a heterogeneous object that causes severe signal attenuation. The dielectric properties of biological tissues can highly influence the performance of an antenna located in close proximity to or inside the human body [117]. This is mainly because the specific dielectric characteristics of each tissue layer bring about different RF interactions. For example the liquid structure of the body causes RF attenuation while the skeleton structure causes wave diffraction and refraction [118].

Moreover in antenna design particular consideration must be given to some other important parameters such as weight loss, effect of aging on skin properties, body movement and body posture. In the case of an in-body antenna, an in-depth exploration should be made of the design, type selection and bio-compatibility of the material, shape and size of the antenna based on its location and most importantly the heating effect of the antenna on human tissues. Existing WBAN antennas are normally classified into two groups [119]:

- *Magnetic antenna:*
  Magnetic antennas such as loop antennas produce an E field which is usually tangential to the human body tissue. This characteristic of magnetic antennas makes them less able to actively couple to the body, resulting in less overheating in the fat than with an electric antenna.

- *Electric antenna:*
  In contrast to the magnetic antenna, an electric antenna such as a dipole generates a larger amount of E field, which is normal to the human tissue. This results in absorption of the wave as well as a temperature rise of the human tissues.

In general the signal propagation inside the human body and the performance of the localisation system can be influenced by the deployed antenna type, antenna radiation pattern and antenna orientation. Therefore it is essential to select an antenna type that meets the location-estimation requirements.

This chapter presents a study of different antenna types that can be used for capsule localisation based on a radar system. The investigation was performed with two antenna types: a half-wave dipole antenna and a loop antenna. Since the position of the antenna and its polarisation play an important role in system design, knowing different

antenna polarisations and how to maximise their benefits can significantly improve the performance of the system. Thus different polarisations for a half-wave dipole antenna have been studied to find out the best performance for our radar system. Furthermore we compared the performance of the selected antennas to select the one best suited to the localisation requirements.

5.2 Half-Wavelength Dipole Antenna

A half-wavelength dipole antenna is considered as a special case of a dipole antenna, with a length of a half-wavelength at the operating frequency. According to the obtained results from Chapter 4 we decided to choose 2.4 GHz as our working frequency, so a half-wave dipole antenna to work at 2.4 GHz was designed, with a height of 54 mm and radius of 1.5 mm. Perfect Electric Conductors (PEC) are assumed to be the material of the dipole's arms. The reference and the source impedance were set to 138 Ω to optimise the return loss (S_{11}). The achieved return loss for this antenna in free space is -32 dB (Figure 5.1). In our study, to contemplate a realistic situation and also to prevent the deteriorative effect of the human body on the antenna performance, the antenna was attached in wool fibre and positioned in front of the human abdomen. The 0.62 mm wool fabric has a conductivity of 0.00723207 S/m and relative permittivity of 1.3 at the selected frequency [120]. However, by putting the antenna next to the abdomen of the human model, the performance deteriorated and needed to be optimised again for the new environment. In this step the reference impedance was set to 82 Ω, which resulted in S_{11} of around -25 dB (Figure 5.2).

5.3 Choice of Dipole Antenna's Direction for Tracking Capsule Endoscope

The position and direction of the antenna can influence the received signal at different locations of the capsule. To find the best position for the designed half-wave dipole antenna the antenna performance was investigated at three different positions: vertical, horizontal and at a 45-degree position. Figures 5.3(a), 5.3(b) and 5.3(c) illustrate these positions respectively. It should be noted that we assumed that our radar system is a single-transceiver based system with a single antenna.

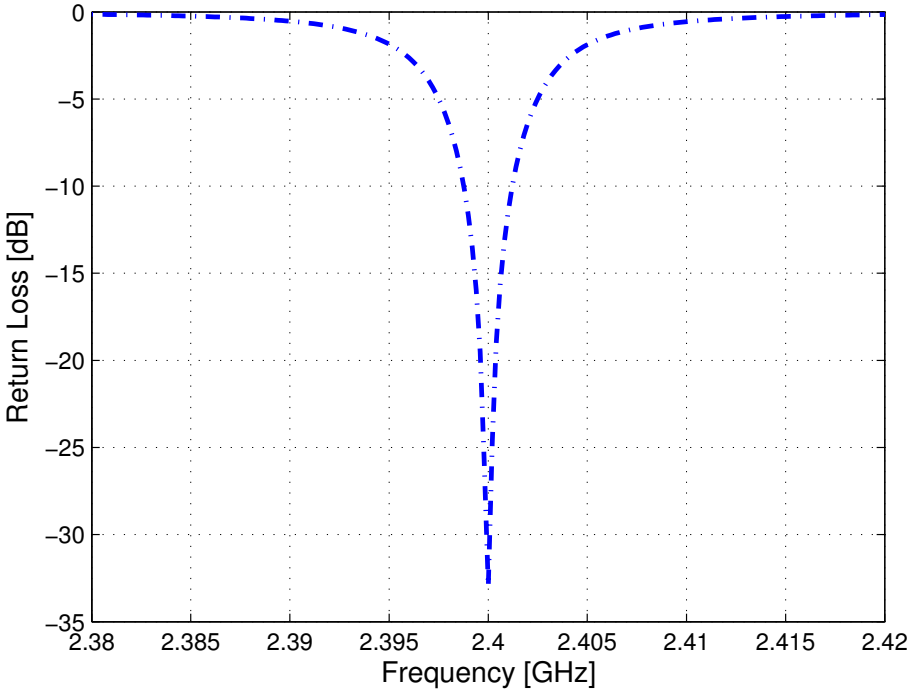

Figure 5.1: Reflection coefficient of the half-wave dipole antenna in free space

Figures 5.4, 5.5 and 5.6 show the attenuated signal at these three different positions. Since the antenna was located at the middle of the abdomen at distance 100 mm, all simulated plots are nearly symmetrical with respect to this point.

As can be seen from Figure 5.4, in the vertical position of the antenna the attenuation in the central area of the abdomen is lower than when the antenna is positioned horizontally. The antenna at a 45-degree position has a similar performance to in the horizontal position.

The discrepancy between results reveals that the position of the antenna and the polarisation of the transmitted wave can easily influence the received signal strength.

In general, antenna polarisation shows the direction of the transmitted electrical field vector. It can be classified into three categories: linear, circular and elliptical polarisation, while linear polarisation can be subdivided into horizontal, vertical and 45-degree polarisations.

According to the vertical or horizontal position of the receiver it can receive vertically or horizontally polarised waves. Therefore, the received signal level can change if there are any changes in polarisation. However, the best signal in a line-of-sight link

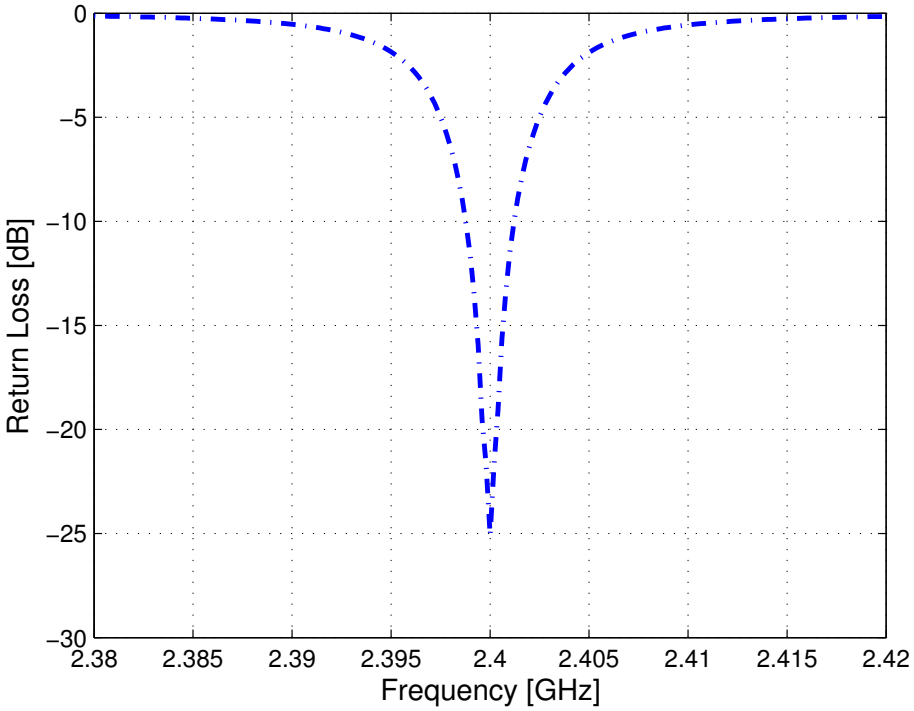

Figure 5.2: Reflection coefficient of the half-wave dipole antenna placed next to the human abdomen

will be achieved when the receiver and transmitter antennas have a similar polarisation.

Because our transmitter and receiver are co-located, the receiver antenna is co-oriented with the transmitting antenna and consequently the maximum pickup will be achieved.

The simple dipole antenna has a linear polarisation, so it is important to know in which antenna alignment the maximum signal strength is achievable. The results show that the vertical antenna with a vertically polarised wave can provide a more accurate result in the central area, whilst the horizontal and the 45-degree antennas have a poorer performance in the same area of the bowel. Also, the performance of the antenna on the two sides of the abdomen are quite similar in all three positions.

The small intestine can be divided into three portions: the duodenum, the jejunum and the ileum. The jejunum mostly occupies the umbilical and left iliac regions whereas the ileum is situated mostly in the umbilical, right iliac, hypogastric and pelvic regions [20]. So it seems that the umbilical region, which is the middle region of the human abdomen, is the most compacted region in terms of the small intestine (Figure 2.2). Therefore tracking the capsule in the centre of the abdomen is more complicated than in

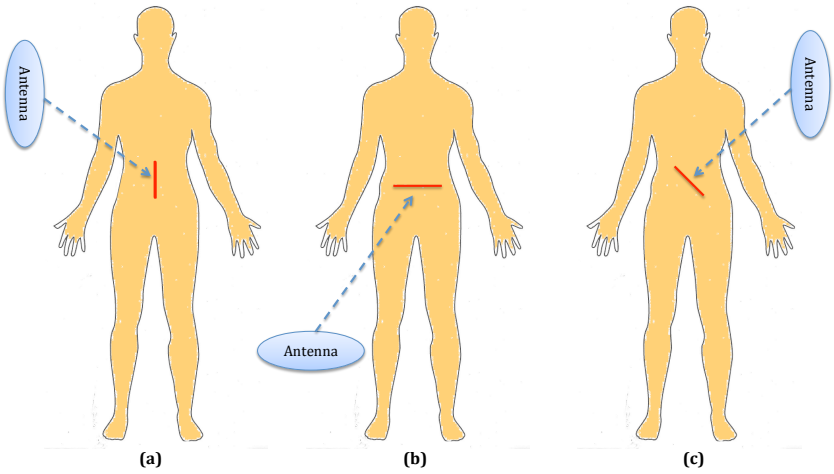

Figure 5.3: Three different antenna positions on the human body

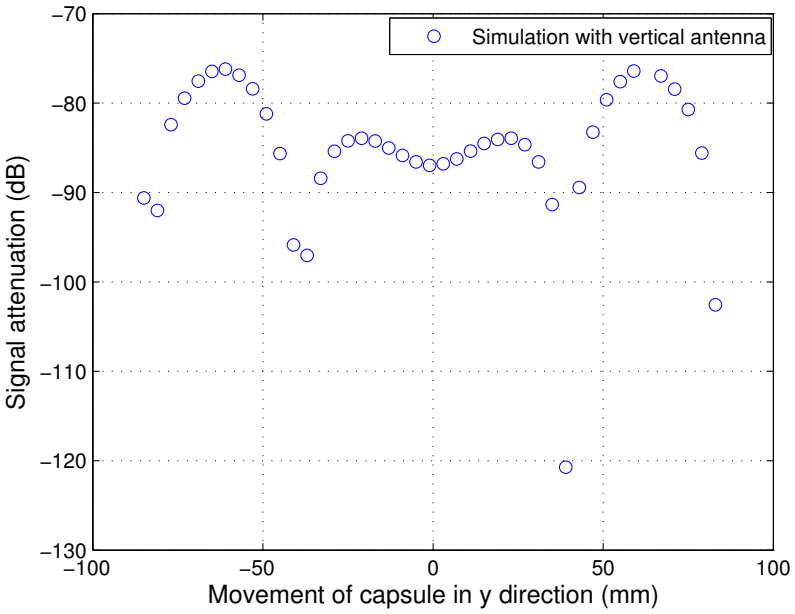

Figure 5.4: SEMCAD simulated power loss by vertical antenna

the other areas. Since, of the different antenna positions, the vertical position provides a better result in the centre of the bowel, this position can be used as a reference for future studies.

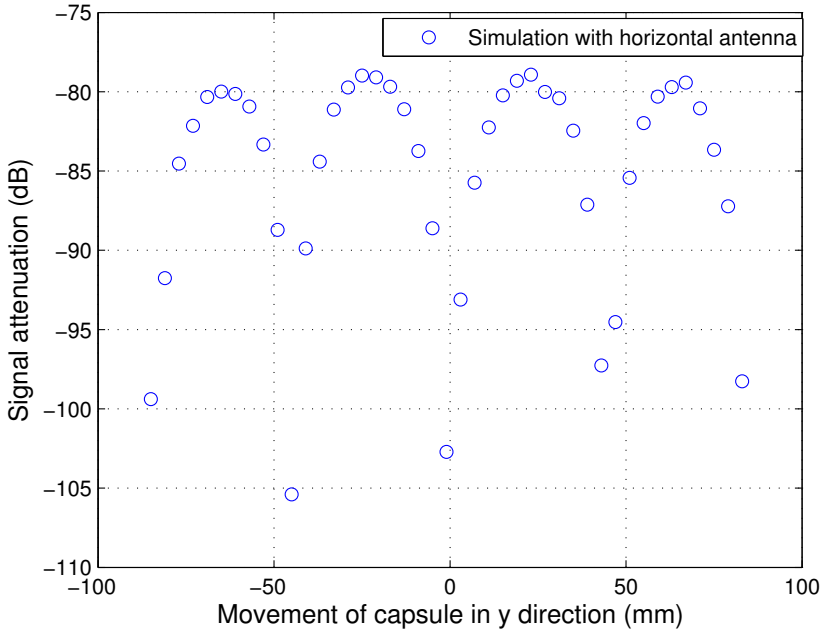

Figure 5.5: SEMCAD simulated power loss by horizontal antenna

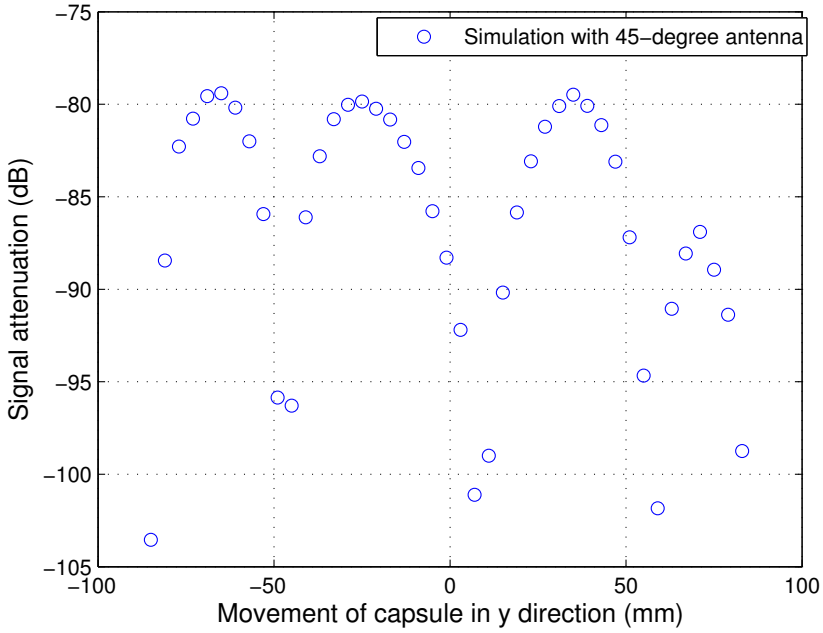

Figure 5.6: SEMCAD simulated power loss by 45-degree antenna

In reality, the capsule moves through the small intestine, that has a complicated shape, thus movements and rotations can happen in different axes. These movement variations can easily influence the reflected wave by changing the phase of the signal, which results in changing the polarisation of the reflected wave. On the other hand, the human body is a non-homogeneous medium for the RF transmission that caused depolarisation of the wave. So the reflected wave from the target inside the body can have a different polarisation from the incident wave. In this case the deployed receiver antenna should have the capability to receive multiple simultaneous polarisations. In practice a simple dipole antenna cannot provide the best coverage on its own due to its inability to manage the depolarisation of the reflected wave. However, for studies similar to our own, which use a simple planar model of the human abdomen, without considering any rotation or vertical movement of the capsule, the simple vertically positioned dipole antenna can work perfectly.

5.4 Loop Antenna

A simple and flexible antenna type is the loop antenna. Loop antennas can be seen in different shapes like: circle, square, rectangle, triangle, ellipse etc. In this section, a printed loop antenna with the size of 70×40 mm^2 was used to evaluate its performance for capsule localisation. Since the designed antenna [121] was a dual-band antenna that is supposed to work in WLAN frequency bands, we optimised it for the single frequency of 2.4 GHz. The achieved return loss for this antenna is -27 dB. Figure 5.7 shows the loop antenna package.

5.5 Comparative Performance of Loop and Dipole Antennas

The loop antenna was subsequently mounted in front of the abdomen cubic model in a specific way; the loop part of the printed antenna was placed at the centre of the model with the vertically polarised wave similar to the dipole antenna. As can be seen in Figure 5.8, because of the geometric shape of the antenna and its feed line, this antenna cannot provide a symmetrical performance in the three upper and lower parts of the abdomen. The path loss measurements were done for all the six sections of the small intestine.

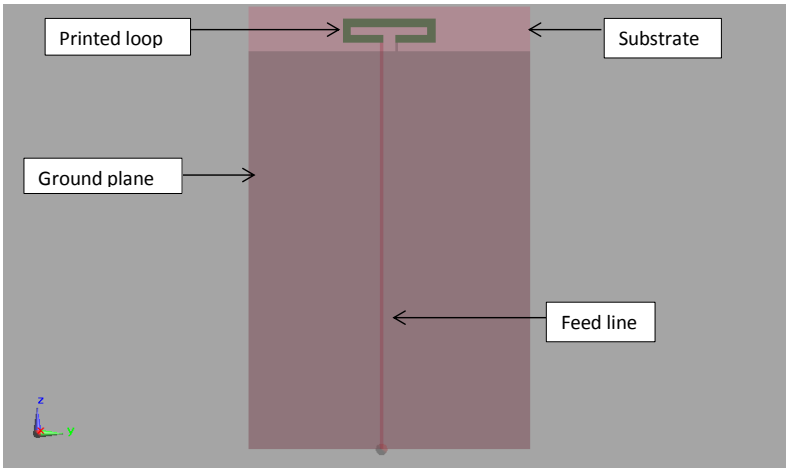

Figure 5.7: Front view of the loop antenna package

Since the diameter of the small intestine varies between 2.5 and 3.5 cm, it is possible to assume the placement of 6 sections (part 1 to part 6) of the whole small intestine with a 2.5 cm diameter inside the cubic abdomen shape. It should be noted that the distance of the antenna source from each track of part 1 to part 6 of the small intestine is 62.5 mm, 37.5 mm, 12.5 mm, -12.5 mm, -37.5 mm and -62.5 mm respectively. Figure 5.9 illustrates different parts of the intestine and the antenna position. The simulations have been done by moving the capsule along the y-axis from 0 to 200 mm. To determine the path loss at different capsule positions, we also manually moved the capsule 4 mm each time in different intestine sections and repeated the simulation a multiple number of times.

The obtained data from the simulations were processed using MATLAB. Figures 5.10 - 5.15 show the simulated loss at the six parts of the small intestine when using the half-dipole and loop antennas. Since both antennas were located at the middle of the abdomen at a distance of 100 mm, all the simulated plots are symmetrical with

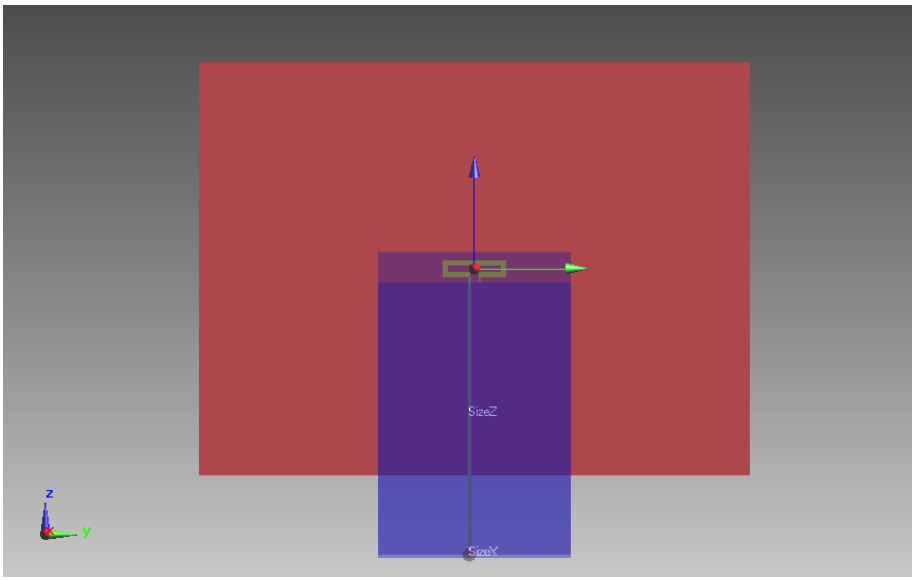

Figure 5.8: Front view of the abdomen and the loop antenna location

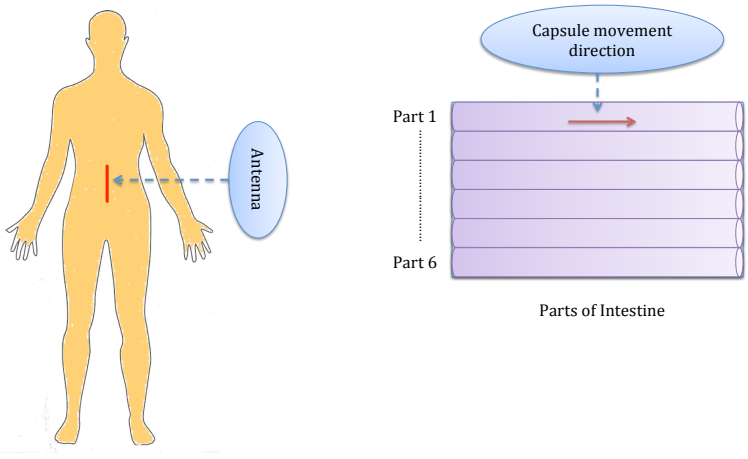

Figure 5.9: Front view of the small-intestine parts and the antenna location

respect to this point.

The presence of any obstacle near the radiating antenna can drastically degrade the radiation properties of the antenna. The human body is a lossy medium, therefore employing a lossless layer such as a wool fabric can effectively prevent the degradation

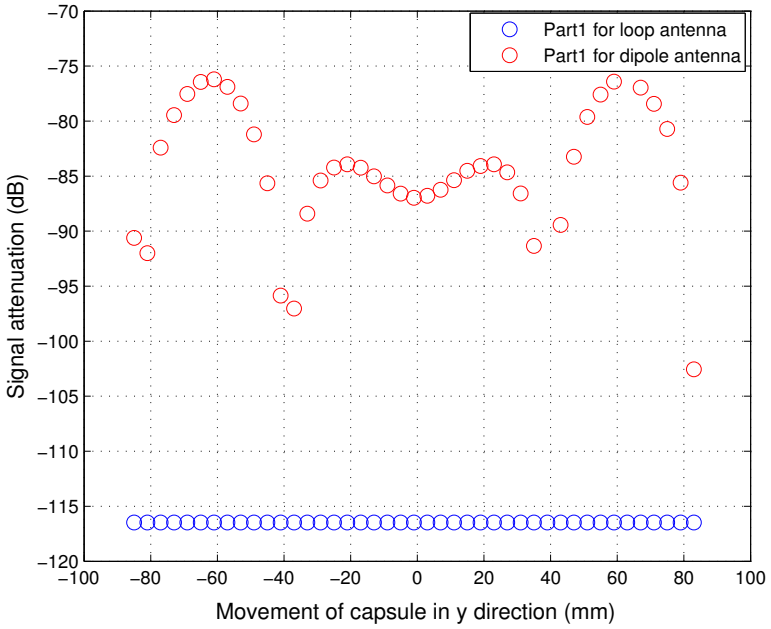

Figure 5.10: SEMCAD simulated power loss at part 1

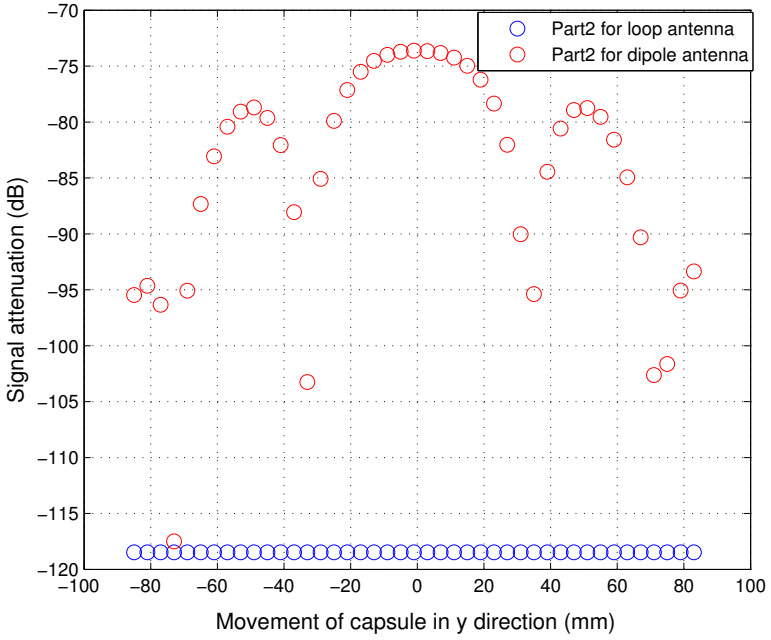

Figure 5.11: SEMCAD simulated power loss at part 2

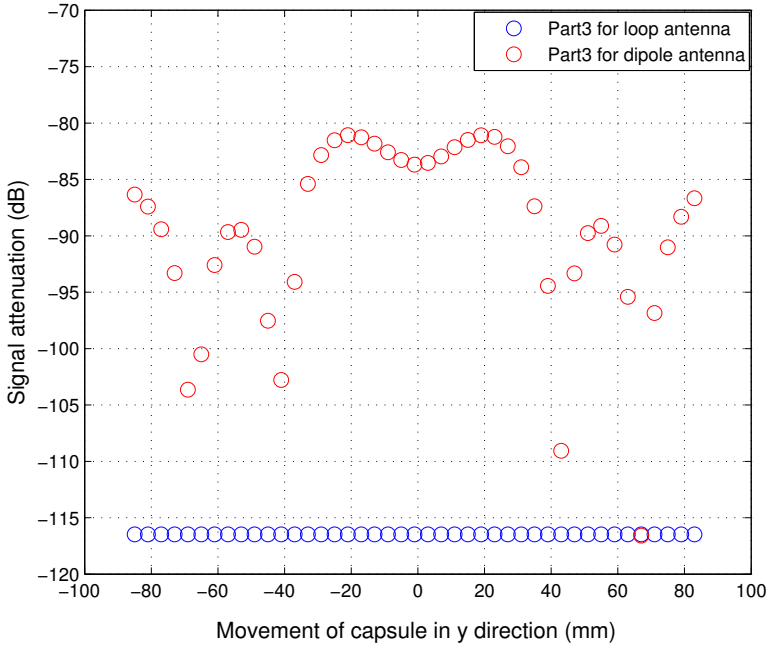

Figure 5.12: SEMCAD simulated power loss at part 3

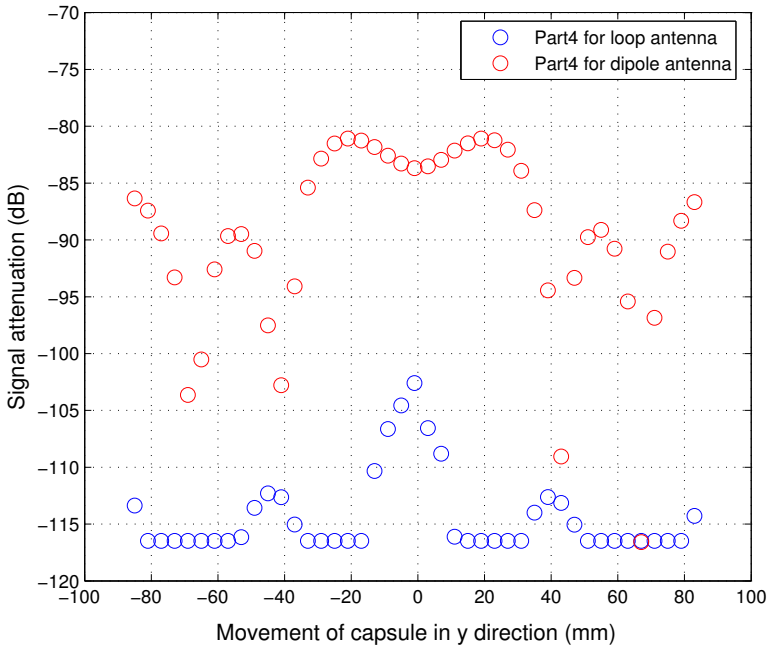

Figure 5.13: SEMCAD simulated power loss at part 4

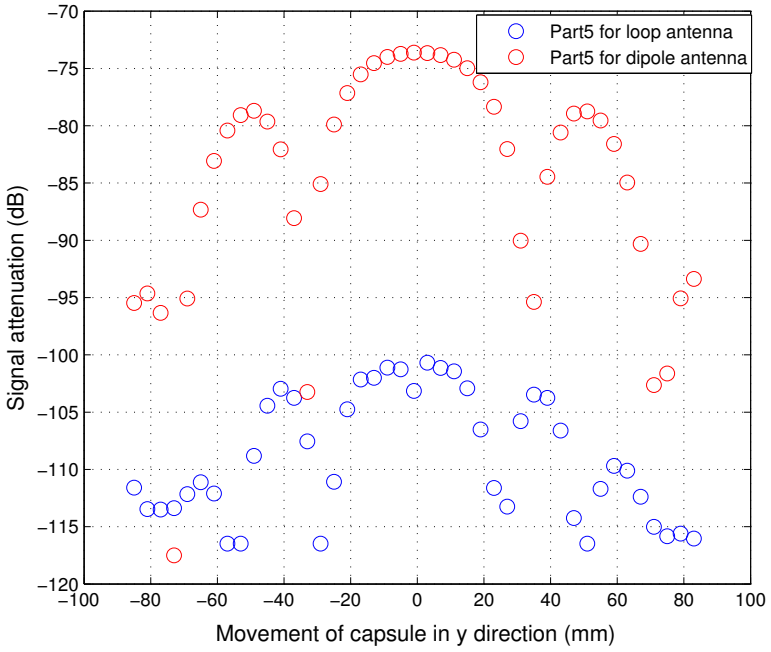

Figure 5.14: SEMCAD simulated power loss at part 5

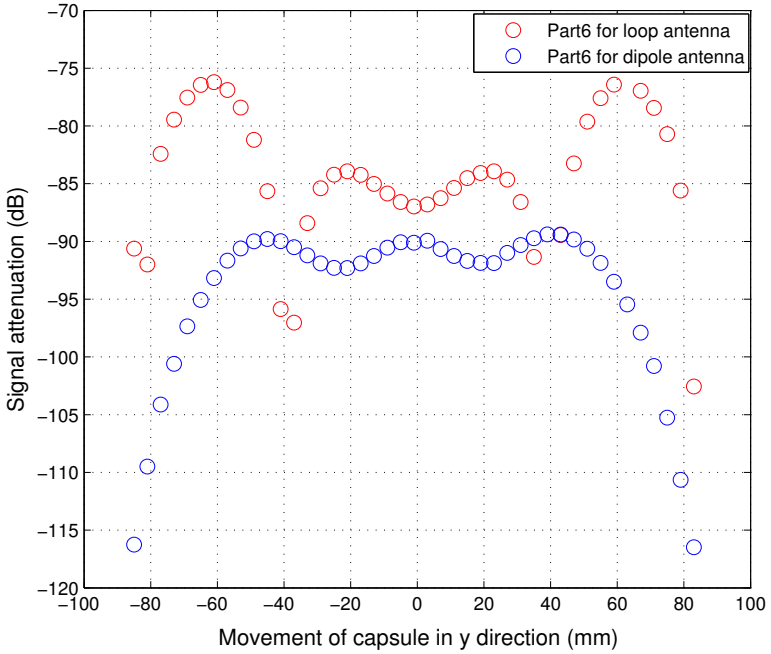

Figure 5.15: SEMCAD simulated power loss at part 6

of the antenna performance. However in the case of the loop antenna, the outer layer of the antenna is the ground plane, which significantly alters the radiation pattern.

In fact the ground surface can reflect any energy from the antenna that radiates toward it. The ground is a lossy medium and, in our simulations, it is assumed to be a perfect electric conductor. In general, the fundamental properties of the ground and its geometry can control the reflection direction and the amount of energy reflected by the ground [122].

From Figures 5.10, 5.11 and 5.12, it can be seen that the dipole antenna outperforms the loop antenna, since through the entire tract of the intestine the path loss was significantly lower than for the loop antenna. The maximum loss of the dipole antenna is about 100 dB, whereas this amount is 116 dB for the loop antenna.

The effect of the ground reflection can also be observed in Figures 5.13, 5.14 and 5.15. In fact, the movement of the capsule in the three upper parts of the intestine is beyond the loop antenna package (Figure 5.8), so the losses are remarkably low in these areas. On the other hand, the capsule encounters lower loss while moving in the three remaining lower parts of the intestine, since the movement is in front of the loop antenna and its ground surface. Also, by comparing the edges and the middle area of each part it can be seen that the attenuation was decreased due to the reflection from the ground plane.

In fact the ground surface reflections direct more energy toward the abdomen, so a greater field can be observed in the region where the ground plane is in front of the abdomen.

Based on the obtained results, it can be stated that the loop antenna cannot provide the desired resolution in location estimation of the capsule endoscope, since the system has a higher loss compared to the situation where the half-wave dipole antenna is used.

The attenuation is even worse when the capsule moves through the regions which are beyond the loop antenna package. This is due to the reduced received energy from the antenna, which results in higher loss. Also, because of the lower variations in loss in these regions, it is hard to detect a difference between different locations of the capsule.

On the other hand, in localisation based on the radar approach the two-way loss should be considered in order to estimate the received signal reflected by the capsule and the capsule location. Our observations conclude that the one-way loss caused by radiation of the signal from the loop antenna is considerable and makes it impractical in a radar-based localisation system.

5.6 Chapter Summary

This chapter presents a performance study of two different antenna types: half-wavelength dipole antenna and loop antenna, for capsule localisation inside the human GI tract. A half-wave dipole antenna was designed at 2.4 GHz and optimised so as to achieve a reflection loss of -25 dB when the antenna locates in close proximity to the human abdomen. To investigate the best position and polarisation for our designed antenna, three different antenna positions have been studied. These three positions are: vertical, horizontal and at a 45-degree position. According to our obtained results the best antenna performance is achievable when the antenna is vertically positioned in front of the human abdomen, because it can provide better signal strength at the centre of the abdomen.

In the second part a WLAN dual-band loop antenna was optimised so as to work at the single frequency of 2.4 GHz. A comparison was made between the performance of the two types of antenna: loop antenna and half-wave dipole antenna, in terms of the signal attenuation inside the GI tract at 2.4 GHz. To evaluate the antenna performance an FDTD-based simulation was conducted when the antenna was mounted on the assumed cubic model of the human abdomen. The obtained results indicate that the half-wave dipole antenna outperforms the loop antenna in all the six parts of the intestine sections, although the loss for the loop antenna can be tolerable when the capsule moves in front of the loop and its ground surface. In the outer region of the loop antenna not only is the loss significantly high, there is also no variation in the obtained loss by displacement of the capsule, which is expected to result in poor accuracy in the location estimation of the capsule at different capsule locations.

Publications pertaining to this chapter:

- P. Ara, M. Heimlich and E. Dutkiewicz, "Investigation of radar approach for localization of gastro intestinal endoscopic capsule," *2014 IEEE Wireless Communications and Networking Conference (WCNC)*, Istanbul, 2014, pp. 99-104.

- P. Ara, M. Heimlich and E. Dutkiewicz, "Antenna performance for localization of capsule endoscope," *2014 8th International Symposium on Medical Information and Communication Technology (ISMICT)*, Firenze, 2014, pp. 1-5.

6

Evaluation of General In-body Path-Loss Model

6.1 Introduction

Recent developments in capsule endoscopy have highlighted the need for accurate techniques to estimate the location of a capsule endoscope. A highly accurate location estimation of a capsule endoscope in the gastrointestinal (GI) tract in the range of several millimetres is a challenging task. This is mainly because the radio-frequency signals encounter a high-loss propagation environment. Moreover the propagation mode (near vs mid vs far field) can change based on the frequency of the localisation method and the location of the capsule itself. Therefore an accurate path-loss model is required to develop precise localisation algorithms.

The literature shows that the propagation region in the body where the capsule is located is a crucial parameter that should be taken into account. Most propagation models assume operation in the far-field region; however this may not be always the case for in-body propagation. In the near-field region the signal attenuation does not follow the same trend as in the far-field region. In this chapter, a simple theoretical path-loss model for in-body applications is proposed. The proposed model is further

compared with existing electromagnetic simulation models using the Finite-Difference Time-Domain (FDTD) method for performance evaluation as well as a theoretical near-field path-loss model.

6.2 General Review on Radio Wave Propagation and Antenna Field Region

Before giving any description of our proposed path-loss model and any analysis of the obtained results, it is appropriate to briefly introduce the theory of radio wave propagation and review the field regions around an antenna.

6.2.1 Theory of Radio Wave Propagation

A travelling wave inside a medium has not all the characteristics of the incident wave due to the periodic changes in the amplitude and phase of the wave inside the medium. Essentially, the material properties of a medium have a significant effect on changing the incident wave characteristics. The three important properties of the material are:

1. Conductivity (σ): Conductivity represents the propensity of a medium to absorb the energy of a propagation wave.

2. Relative Permittivity (ϵ_r): It is commonly known as the dielectric constant and represents the tendency of the medium to store electrical energy and concentrate the electric flux of a propagation wave.

3. Relative Permeability (μ_r): It represents an ability of the material to be magnetised in the presence of a magnetic field.

Electromagnetic propagation is characterised by the propagation coefficient (γ), which is a measure of the changes in the amplitude and phase of an electromagnetic wave as it propagates through a medium in a given direction. It is a complex quantity, where the real part α (attenuation constant) represents changes in magnitude of the electromagnetic wave while the imaginary part β (phase constant) represents the changes in phase.

$$\gamma = \sqrt{j\omega\mu(\sigma + j\omega\epsilon)} = \alpha + j\beta \tag{6.1}$$

in which ω is the angular frequency and α and β are called the attenuation and phase constants respectively, and can be written as [123]:

$$\alpha = \omega \sqrt{\frac{\mu\epsilon}{2}\left[\sqrt{1+\left(\frac{\sigma}{\omega\epsilon}\right)^2}-1\right]} \tag{6.2}$$

and

$$\beta = \omega \sqrt{\frac{\mu\epsilon}{2}\left[\sqrt{1+\left(\frac{\sigma}{\omega\epsilon}\right)^2}+1\right]} \tag{6.3}$$

Materials are characterised as perfect conductors ($\sigma = \infty$) or perfect dielectrics (where $\sigma = 0$). In the case of a perfect dielectric or a low-loss medium the attenuation constant is equal to zero so the propagation constant has just an imaginary part:

$$\gamma = j\beta \tag{6.4}$$

and

$$\beta = \omega\sqrt{\mu\epsilon} \tag{6.5}$$

In the case of lossy materials ($\sigma \neq 0$) the propagation constant (γ) has the two terms of α and β where

$$\beta \neq \omega\sqrt{\mu\epsilon} \tag{6.6}$$

In theory, during the passage of an incident signal through an interface between two media, some parts of the signal are transmitted to the second medium while some parts will be reflected by the interface. Therefore at the interface the intensity of the reflected or transmitted wave can be expressed by reflected and transmitted coefficients (ρ and τ). These coefficients are not only dependent on the material properties of either side of the interface but also depend on the polarisation of the radiation [70]. These coefficients are defined as:

$$\tau = \frac{E_{transmitted}}{E_{incident}} \tag{6.7}$$

$$\rho = \frac{E_{reflected}}{E_{incident}} \tag{6.8}$$

6.2.2 Antenna Field Region

The radiation pattern of an antenna is the spatial distribution of the electromagnetic field generated by the antenna [124]. The space surrounding an antenna is normally divided into three regions: reactive near-field, radiating near-field and far-field regions. These regions depend on distance x from the source of antenna as shown in Figure 6.1. The reactive near-field region is the part of the near-field region that immediately surrounds the antenna, and the reactive field is the dominant field in this region. The radiation near-field region or Fresnel region is the area of the antenna field between the reactive near-field region and the far-field region. The radiation field is the dominant field in this area. The last region is known as the far-field or Fraunhofer region [122].

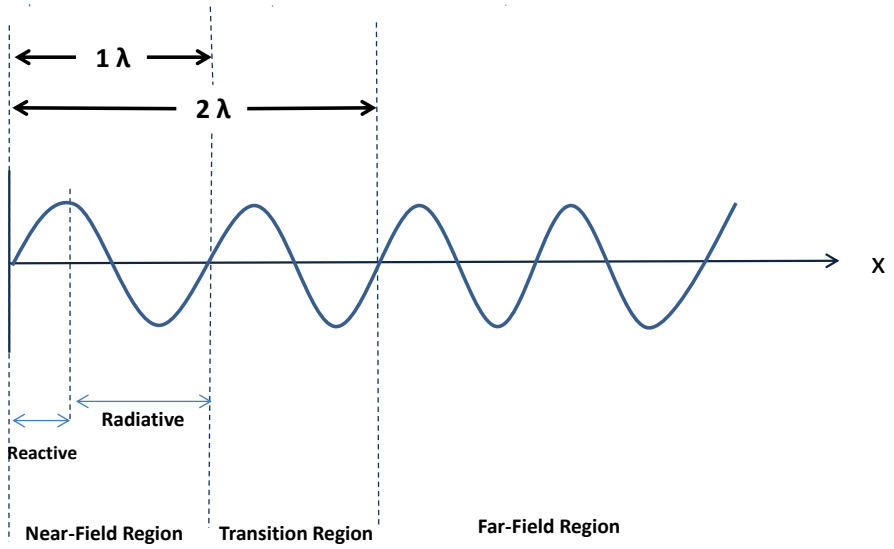

FIGURE 6.1: Radiation pattern of an antenna

The boundary of each region depends strongly on the size of the antenna and its oper-

ating frequency. The boundary regions for different sizes of antenna can be obtained from Table 6.1 [125]. It should be mentioned that, according to the IEEE standard,

Table 6.1: Near-Field and Far-Field Conditions

Antenna Size L	**Reactive near-Field**	**Radiating near-field**	**Far-field**
$L \ll \lambda$	$r < \frac{\lambda}{2\pi}$	$\frac{\lambda}{2\pi} < r < 3\lambda$	$r > 3\lambda$
$L \approx \lambda$	$r < \frac{\lambda}{2\pi}$	$\frac{\lambda}{2\pi} < r < 3\lambda$	$r > 3\lambda$
$L \gg \lambda$	$r < \frac{\lambda}{2\pi}$	$\frac{\lambda}{2\pi} < r < \frac{2L^2}{\lambda}$	$\frac{2L^2}{\lambda}$

the near-field region might not be observed if the size of an antenna is not large enough compared to its wavelength [126]. Apparently the energy of the transmitted signal is different in each region. In the reactive near-field region, which is the closest region to the antenna, the energy of the signal is attenuated with distance. In the radiating near-field region, although energy fluctuations can be seen, the average energy density is quite constant at different distances from the antenna. As opposed to the far-field region, the shape of the radiation pattern in the radiating near-field region varies considerably with distance. In the far-field region the size and the shape of the antenna can be neglected due to the distance of the subject from the antenna. Thus, it can be assumed that in the far-field region the electromagnetic field is entirely a radiating plane wave. In this region the angular distribution of the energy does not change with distance, and the power level attenuates based on the inverse square law with distance [127]. The near-field region is a close-in region to a radiating source. The electric and magnetic fields' performance and behaviour are totally different in the near-field region. According to [128] the power loss in the near-field region can be obtained from

$$PL = \frac{G_T.G_R}{4}\left(\frac{1}{(Kd)^2} - \frac{1}{(Kd)^4} + \frac{1}{(Kd)^6}\right) \tag{6.9}$$

where G_T and G_R are the transmitter and receiver gains respectively. d is the distance from the antenna and $K = \frac{\lambda}{2\pi}$. It can be seen that the power in the near field typically decreases with the inverse fourth power $(1/d^4)$ of distance. This means that this region has higher power than the far-field region. Therefore it is expected to achieve a higher signal-to-noise ratio (SNR) and a better performance link in this region. In fact the energy in this region is kind of circulating. Some parts are returning to the source while the rest is continuing to be transmitted outside this region toward the far-field region [127, 128]. Moreover, in the near-field region less interference can be observed

than with other RF systems that operate outside the range of the near-field region.

6.3 General Abdomen Path-Loss Model

In general, radio propagation of waves through a medium can be affected by several factors, which leads to an attenuation or loss of RF signal. Attenuation is a gradual loss in intensity of a signal through a medium. Some of the most significant attenuation-causing factors are summerised here as [129, 130]:

- **Absorption:** One of the most important behaviours of an RF signal is absorption. In general, when an RF signal passes through an object the part of energy of the radio wave can be absorbed by the object. Absorption is one of the main reasons of signal attenuation.

- **Reflection:** It occurs when an RF signal bounces off the surface of an object and changes direction. In fact if a signal hits a material, a partial signal can be reflected by the boundary of that material.

- **Scattering:** When an RF signal hits an object the reflected signal can be spread out in many unpredictable directions.

- **Diffraction:** This effect is similar to scattering, however the signal will be deviated at the edge of an object in different directions.

- **Refraction:** This happens due to changes in velocity when an RF signal passes through different media with different densities.

- **Shadowing:** or blocking of signal is due to the existence of a large obstacle in front of the propagation path.

To develop an efficient in-body path-loss model, absorption loss and reflection losses are considered to be the dominant losses that attenuate the signal along the path. Recently, different in-body path-loss models have been proposed to investigate wave propagation within the human body [86, 96, 131]. However the reflection losses due to each layer's boundary or the absorption losses of the possible transmitted signal in each tissue layer have not been considered. For simplicity, we start our analysis of signal attenuation in a medium by choosing a simple three-layer medium and then we extend our discussion to multiple layers.

6.4 Propagation in a Three-Layer Medium

A simple three-layer medium with layers L_1, L_2 and L_3 is considered for this section. We assume that the two layers L_1 and L_3 are free-space layers which have an infinite thickness. The L_2 layer, with a thickness of d_2, is surrounded by the two aforementioned layers (L_1 , L_3). A uniform plane signal $\hat{E}_i$ with magnitude of E_m, is considered as an incident signal toward the boundary or interface between layers L_1 and L_2. A uniform plane wave is the simplest electromagnetic wave that propagates along some fixed direction such as z while the electric and magnetic fields are orthogonal and have no dependence on the perpendicular coordinates such as x, y. Also the magnitude and phase are constant and independent of position in each of these planes [132].

The condition of signal transmission and reflection of each layer is illustrated in Figure 6.2.

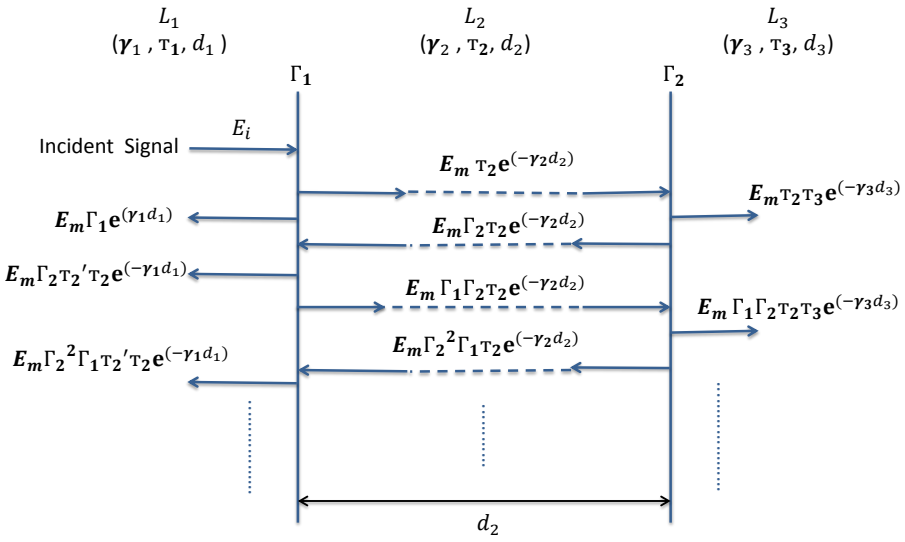

Figure 6.2: Multiple reflection and transmission in a three-layer medium

In fact when incident power hits any interface a part of the signal is transmitted to the next layer in the same forward direction while part of the signal is reflected in the backward direction into the previous layer. Moreover, there will be no backward wave from layer 3, since we assume that this layer has an infinite thickness. In theory the reflected power from each interface is retransmitted in the backward direction until it

returns to the receiver. On the other hand, some parts of this backward reflected power can be easily absorbed or attenuated by the previous layers in the backward direction. Therefore in highly absorbing dielectric materials the amount of retransmitted reflected signal can be small. The total reflected signal from the boundary between layers L_1 and L_2 is

$$\begin{aligned} P_L(Reflected) = E_m\Gamma_1(e^{\gamma_1 d}) + E_m\Gamma_2\tau_2\tau_2'(e^{-\gamma_1 d_1}) + \\ E_m\Gamma_2^2\Gamma_1\tau_2\tau_2'(e^{-\gamma_1 d_1}) + E_m\Gamma_2^3\Gamma_1^2\tau_2\tau_2'(e^{-\gamma_1 d_1}) + ... \end{aligned} \tag{6.10}$$

Assuming that the signal strength from multiple reflections is too weak and just considering the first and second reflections, the total reflection can be summarised as

$$P_L(Reflected) = E_m\Gamma_1(e^{\gamma_1 d}) + E_m\Gamma_2\tau_2\tau_2'(e^{-\gamma_1 d_1}) \tag{6.11}$$

The total signal absorbed by L_2 and L_3, again by assuming that the multiple reflections between the boundaries of L_1 and L_2 in medium 2 are too weak to be transmitted to layer 3, is

$$P_L(Absorption) = E_m\tau_2(e^{-\gamma_2 d_2}) + E_m\tau_2\tau_3(e^{-\gamma_3 d_3}) \tag{6.12}$$

6.5 Propagation in a Multi-Layer Medium

In the case of a multi-layer medium such as human tissues we can apply the same principle as explained in Section 6.4. Since our main focus is on in-body propagation, absorption and reflection losses are considered to be the dominant losses, that can be analysed and calculated as follows.

(A) **Absorption loss:** The absorption loss of the transmitted power in each tissue layer as related to its thickness d and is given as

$$P_L(Absorption) = E_m\left(\sum_{i=1}^{m}[(\tau_1...\tau_i)\left(e^{-\alpha_i d_i}\right)]\right) \tag{6.13}$$

where i is the number of a tissue layer, which in our case is up to 6, d_i is the length of the path traversed by the wave at the i^{th} layer. τ_i is the transmission

coefficient calculated from

$$\tau = \frac{2\sqrt{\epsilon_2 \mu_r}}{\sqrt{\epsilon_2 \mu_r} + \sqrt{\epsilon_1 \mu_r}} \tag{6.14}$$

Based on Table 4.1, the thickness of each tissue layer can be found for the corresponding calculation. The dielectric properties of each tissue layer at different frequencies have been obtained from [113]. Since the signal propagates through different paths and the travel distance can vary in each tissue layer, the distance which the signal travels in each layer is calculated according to the location of the capsule. Therefore, the absorption loss can be calculated based on the selected thickness and each tissue's parameters.

(B) **Reflection loss:** In addition to loss due to the absorption of each tissue layer, the loss that occurs due to reflection by the layer's boundary should also be considered. The reflection loss can be calculated as follows:

$$P_L(Reflection) = \Gamma_1 e^{-\alpha_1 d_1} + \left[\sum_{k=2}^{n} \left(\Gamma_k \prod_{i=1}^{k-1} \tau_i \tau_i{}' \right) e^{-\alpha_1 d_1} \right] \tag{6.15}$$

where n is the number of boundaries, Γ_1 is the reflection coefficient of the first boundary toward free space, τ is the transmission coefficient of each layer through which the signal is passing to reach to the capsule and τ' is the transmission coefficient of each layer toward free space as the signal returns to the radar receiver. The reflection coefficient Γ can be calculated based on the following formula:

$$\Gamma = \frac{\sqrt{\epsilon_{r2} \mu_r} - \sqrt{\epsilon_{r1} \mu_r}}{\sqrt{\epsilon_{r2} \mu_r} + \sqrt{\epsilon_{r1} \mu_r}} \tag{6.16}$$

where ϵ_r is the relative permittivity of each tissue layer and μ_r is the relative permeability, assumed to be close to 1 for most materials.

On the other hand, the free-space loss is required to be calculated and added into the final loss according to the distance of the antenna from the human body. The

free-space loss can be obtained from

$$P_L(d) = 20 \log_{10} \left(\frac{4\pi d}{\lambda} \right) \tag{6.17}$$

Therefore the total path loss can be calculated by adding the losses due to absorption, reflection and free space propagation as

$$PL = P_L(Absorption) + P_L(Reflection) + P_L(FreeSpace) \tag{6.18}$$

In order to investigate the propagation of a wave through the abdomen of the human body, the abdomen was illuminated by a plane electromagnetic wave from a radar transmitter located outside the human body. To simplify our analysis, we modelled the abdomen of the human body as parallel layers of biological tissues by considering the dielectric properties of each tissue layer. The power loss between our radar receiver, that is co-located with the transmitter, and each capsule location inside the small intestine can be determined by applying the basic principle of wave propagation inside a medium using Equation 6.18. Several simulations have also been performed on the same number of tissue layers to examine the accuracy of the proposed path-loss model.

6.6 Simulation Setup

Simulations are conducted using a 3D electromagnetic solver SEMCAD X employing FDTD techniques for the numerical analysis. The FDTD simulation results can be considered as the real measurements to evaluate the proposed path-loss model, since the real measurements are not completely practical for the capsule endoscopy subject. The human abdomen is modelled by using a cubic shape with dimensions of 67.12×200×150 mm^3. The same medium as in the layered planar model has been also used for the human abdomen (Figure 4.3).

The capsule endoscope is the target object for our radar system. It is modelled as a 26 × 11 mm^2 cylindrical object with perfect electric conductor (PEC) material. Our designed half-dipole antenna at 2.4 GHz was used for these sets of simulations, since based on our studies on the performance of different antennas (loop and half-dipole) in Chapter 5, the half-dipole antenna outperforms the loop antenna with respect to signal attenuation inside the human abdomen region. The antenna was attached vertically into wool fabric with the thickness of 0.62 mm and positioned in front of the human abdomen.

UPML (Uniaxial Perfectly Matched Layers) absorbing boundary conditions were selected to truncate the computational domain. UPML works similarly to the absorber in an anechoic chamber and prevents wave reflections from the environment. Similarly to our study in Chapter 5, it is assumed that the small intestine has 6 sections (part 1 to part 6) with a 2.5 cm diameter and is located inside the cubic abdomen shape as shown in Figure 5.9 . The harmonic simulations were run at 2.4 GHz and the field distribution was recorded at different locations of the capsule inside the intestine. The simulations have been done by moving the capsule along the y-axis from 0 to 200 mm. To determine the path loss at different capsule positions, we also manually moved the capsule 4 mm each time in different intestine sections and repeated the simulation three times.

6.7 Comparison of Near-field and Far-field based Path-loss Model

Figures 6.3 - 6.5 show the simulated and calculated loss (using Equation 6.18) at the three upper parts of the small intestine. Since the antenna was located at the middle of the abdomen, at a distance of 100 mm from the edges of the abdomen, all the simulated plots are symmetrical with respect to this point.

In our case, the antenna is 54 mm in length and is operating at 2.4 GHz. Therefore the movement of the capsule mostly happens in the radiating near-field region for all three tracking paths. The path-loss model is developed according to an exponential decay of the uniform plane-wave amplitude that propagates through the homogenous medium. In general, in the far-field region of the antenna the radiated wave can be denoted by a uniform plane wave. Therefore it can be seen that the absorption calculation is based on the absorption of the signal in the far-field region, which is in contrast with the simulation scenario, where the capsule moves in the near-field region of the antenna. As can be seen in all figures, the theoretically calculated loss demonstrates discrepancies with the SEMCAD simulated results due to the fact that in all the theoretical calculations the far-field region only is assumed, whilst the near-field regions are taken into account in the simulations. In order to compare the simulated loss pattern with the near-field loss, we have calculated the near-field loss according to Equation 6.9 and added it to all the plots. In our case, the transmitter and receiver

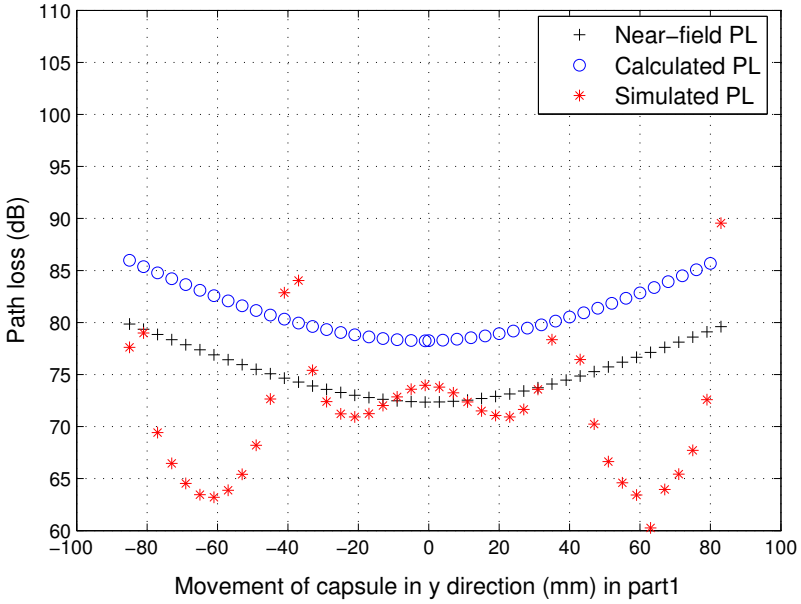

FIGURE 6.3: Calculated and simulated power loss at part 1, where the capsule movement is in the radiating near-field region

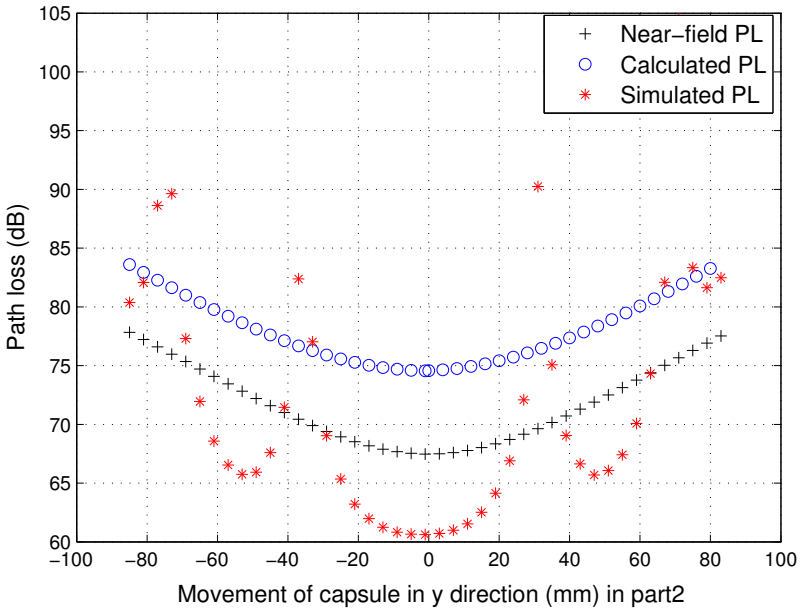

FIGURE 6.4: Calculated and simulated power loss at part 2, where the capsule movement is in the radiating near-field region

gain is 2.15 dBi and the wavelength of the signal at the point of measurement (small

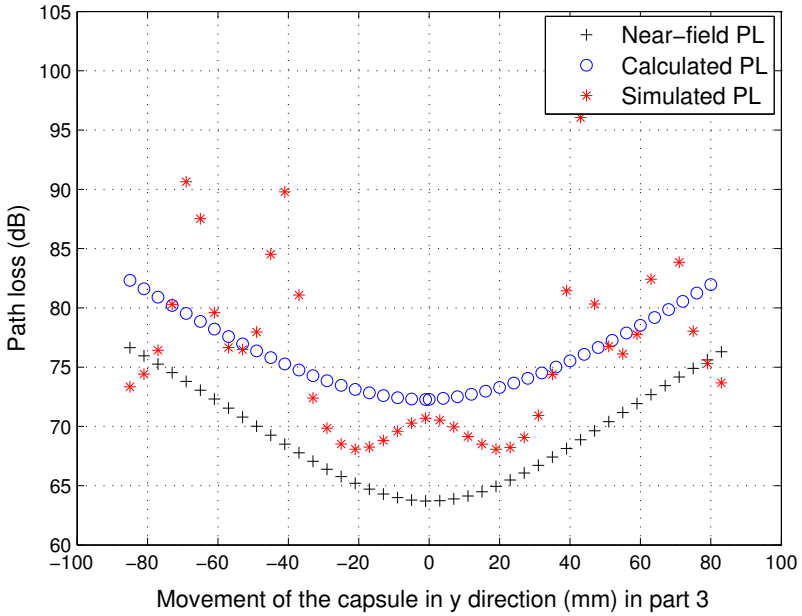

Figure 6.5: Calculated and simulated power loss at part 3, where the capsule movement is in the reactive near-field region

intestine) is 16.55 mm.

In Figures 6.3 and 6.4 higher attenuation, specifically in the far distance of the antenna, can be observed for the simulation data compared to the near-field loss. This is because the capsule movement in parts 1 and 2 of the abdomen subdivisions is in the radiative region close to the boundary of the far-field region. Therefore the near-field model cannot exactly match with the simulated results. It can be also seen in Figure 6.5 that the simulation data lies within our proposed loss model and the calculated near-field loss. Although the capsule in part 3 of the intestine moves in the radiative near-field region, the movement is mostly in the close vicinity of the reactive near-field region, so the distribution of the loss closely matches the loss in the near-field region. Figure 6.6 shows the average calculated loss based on our proposed model, the average simulated loss and the average near-field loss for the three upper parts of the intestine. It appears that the average near-field loss can be a good match for the average simulated data. In order to find the extent to which the near-field path loss and our proposed path-loss model agree with the simulated data, the correlations between the simulated data and the two latter models are calculated.

The results in Table 6.2 show that the average near-field loss has a closer correlation with the average simulated data than our proposed model. It has to be highlighted

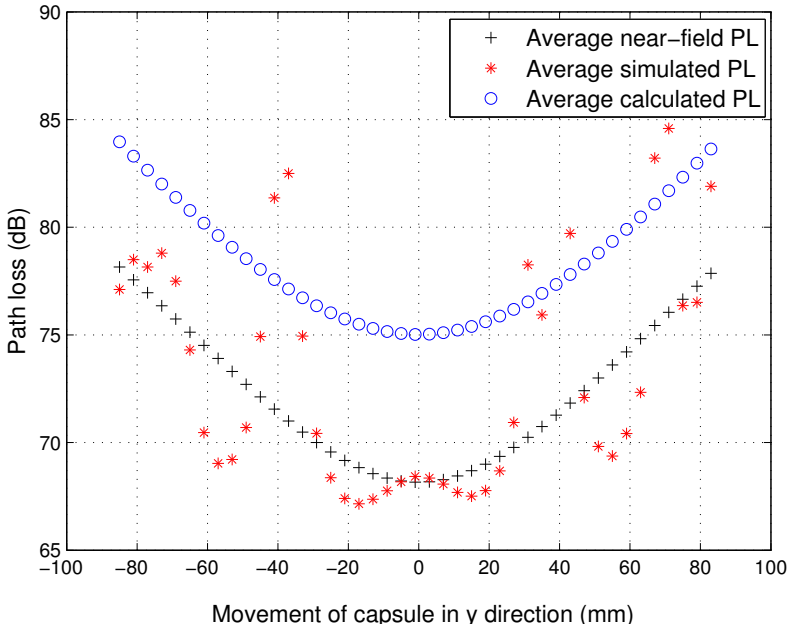

FIGURE 6.6: Average path loss for three upper parts of the intestine

that, to be able to estimate accurately the location of the capsule at each instant based on the RSS technique, it is crucial to know the exact amount of path loss at each capsule location. Although the average near-field loss is in good agreement with the average simulated data, the capsule movement inside the intestine is in different electromagnetic regions with respect to the receiver antenna. Therefore, the near-field loss model alone cannot be a suitable option to model the loss through the entire abdominal region.

TABLE 6.2: Correlation coefficient between the average simulated loss and the two other loss models

	Correlation coefficient	
	Average calculated loss	**Average near-field loss**
Average simulated data	0.5788	0.9979

6.8 Chapter Summary

This chapter presents a new in-body path-loss model based on two key insights, and investigates its performance in the human abdomen area. The proposed path-loss model is based on the absorption loss by each tissue layer and the reflection loss by each layer boundary, and incorporates propagation considerations other than the far field. It is necessary and appropriate to treat the different biological materials, fat, muscle, skin, etc., individually as their material properties vary widely and can produce additional reflections which contribute to the path loss of an endoscopic capsule. Similarly, for frequencies in the RF and microwave regions, the capsule may be within the near field of a localisation antenna positioned against or nearly against the torso skin. A comparison is made between theoretical results and those obtained from FDTD-based simulations. The comparison results indicate discrepancies between theoretical results and FDTD-based simulations. The path-loss equations assume that the target is located in the far-field region, so the signal decays exponentially with respect to distance from the source. However, the target is often in close proximity to the source, in its near-field region, where the attenuation does not follow the same rule as in the far-field region. Our results show that the specific propagation region where the capsule is located within the body is a crucial parameter to be considered in a path-loss model, as the capsule moves through different propagation regions during its eight-hour journey within the abdomen. Hence a deterministic path-loss model, which is only dependent on a theoretical analysis of radio-wave propagation inside the abdomen area, cannot fully address the accuracy of the model for each capsule location inside the abdomen. This issue is even more crucial at higher frequency, where a smaller antenna size is used and the object lies closer to the near-field region. Therefore Chapter 8 presents a newly developed statistical path-loss model which is based on simulation on three different human phantom models.

Publication pertaining to this chapter:

- P. Ara, E. Dutkiewicz, and M. Heimlich, "In-body Path-loss Model Evaluation for Localization of Capsule Endoscope," *2016 EURASIP Journal on Wireless Communications and Networking*, Submitted.

7

Sensitivity Test Analysis

7.1 Introduction

With the advance of different computing technologies, engineering designers are able to develop several visual test models and understand their underlying details and phenomena prior to doing any production or operation. Sensitivity analysis is the process that allows engineers to assess the designed model and identify the sources of uncertainty and their influence on the system performance. Sensitivity analysis should be considered as an integral part of developing any design or model. It provides an analytical examination of input parameters to validate a model. It helps a designer to have some insights into the behaviour of the system by doing experiments with a wide range of parameters.

For example, to address different application requirements in in-body wireless communications, several computational human phantom models have been developed to make up the same scenario as a real human body for researchers [133–137]. This is mainly because most in-body studies are not directly practical on a real human body.

One of these applications is developing an accurate in-body path-loss model that needs to be perfectly addressed during the research procedure, as the real measurement is quite difficult in a real human subject.

Recently various studies have focused on developing an in-body path-loss model to reveal the human body's effects on propagation of waves inside the body [79–81, 86, 87, 89]. However using different computational human phantoms with different settings makes it hardly feasible to evaluate each proposed model with regard to its accuracy or validity. This chapter presents a sensitivity test analysis on adjusting the best possible voxelling for the human models prior to performing any simulations on them. It provides a detailed analysis of RF signal propagation in the abdomen region of different human subjects at 2.4 GHz and shows how setting the best possible grid size can affect the accuracy of the loss and distance measurements and improve the overall system performance.

7.2 Numerical Simulation

To investigate the RF propagation inside the human abdomen and develop the appropriate in-body path-loss model, the interior of the human abdomen is considered to be the propagation channel since the signal should pass through the abdomen area to reach its desired target in the small intestine. Simulations are conducted using a 3D electromagnetic solver SEMCAD X employing FDTD techniques. FDTD is a numerical analysis technique based on Maxwell's equations to illustrate the behaviour of the electromagnetic field of an object in complex structures. It is one of the most suitable techniques for various electromagnetic simulations of the human body. Therefore FDTD simulation results can be considered as real measurements to investigate the propagation of waves inside the human body.

Our designed half-dipole antenna at 2.4 GHz (Chapter 5) was used for these sets of simulations. In order to contemplate a realistic situation and also to prevent the deteriorative effect of the human body on the antenna performance, the antenna was attached vertically into wool fibre and positioned in front of the human abdomen. UPML absorbing boundary conditions were selected to truncate the computational domain. The harmonic simulations were run at 2.4 GHz and the field distribution was recorded at different locations of the capsule inside the intestine.

7.2.1 Human Phantom Models

To compare the signal attenuation in different anatomical models the simulations have been done for three different phantom models. A 26-year-old female anatomical model

"Ella", an 11-year-old female anatomical model "Billie" and a 34-year-old male anatomical model "Duke", were created by the ITIS Foundation [137] and supported by the SEMCAD software employed for our simulations (Figure 7.1). The characteristics of the phantom models are summarised in Table 7.1.

Table 7.1: Different human phantoms characteristics

Human Phantom Model	Sex	Age	No.Tissues	Weight (kg)	Height (cm)	BMI
Duke	Male	34	77	72.4	177	22
Ella	Female	26	76	58.7	163	21
Billie	Female	11	75	35.4	147	16

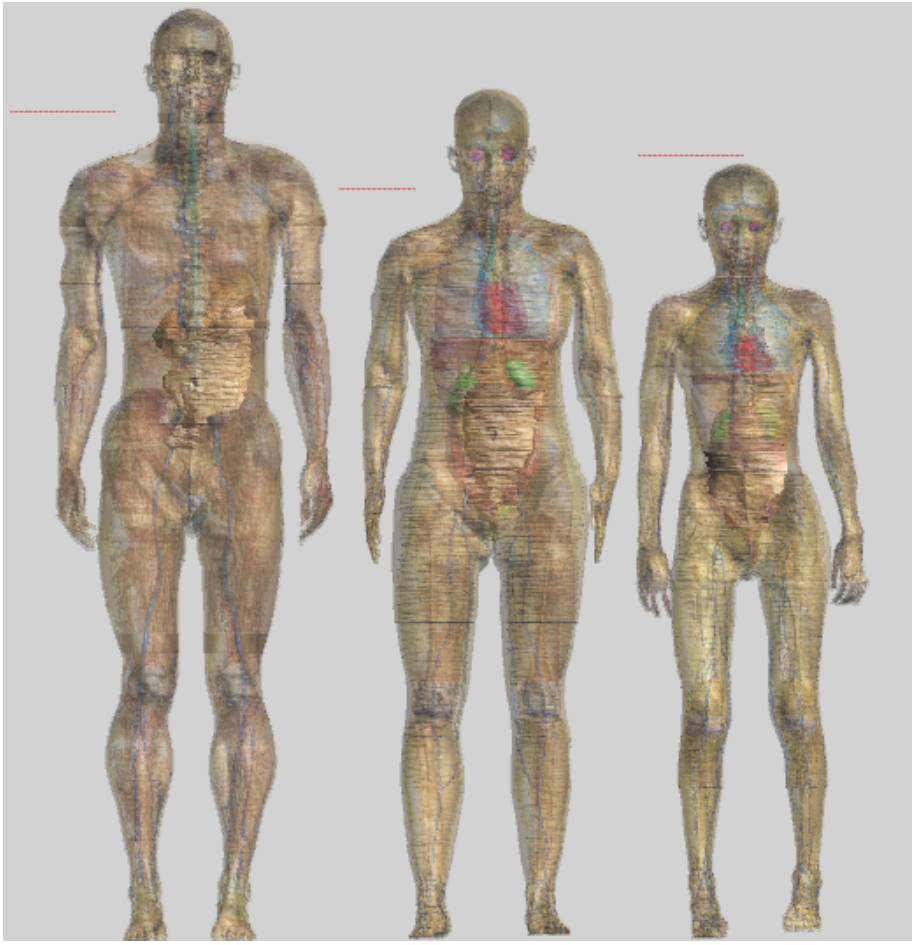

Figure 7.1: Duke, Ella and Billie phantom models

7.2.2 Intestine CAD Model

Since the human models provided by SEMCAD X are based on MRI images, their small intestine does not support the desired resolution and segmentation and it is not possible to freely move the capsule to different intestinal sections. Therefore, we developed our own intestine CAD model and imported it to the human phantom models. The three-dimensional model of the gastrointestinal tracts was created using Rhinoceros (Rhino3d, Robert McNeel and Associates, USA). Briefly, the basic geometry (overall width and height) of the intestine was first estimated from an MRI image in the coronal plane. A spine was then used to model the trajectory of the intestinal tracts by estimating its geometry from the MRI image. The lumen of the intestinal tract was assumed circular and a circle (20 mm × 20 mm) was modelled at one end of the spine and on a plane that was perpendicular to the tip of the spine. A sweep function was then performed to obtain the three-dimensional model, and a similar process was repeated using the same spine but with a smaller circle at the spine tip to model the inner surface of the lumen. A Boolean function was then performed to subtract the inner surface of the intestinal tract from the primary model. The geometry of the spine was then adjusted at various parts of the model to prevent any overlapping of surfaces until a solid hollow tube representing the gastrointestinal tract was obtained.

Our developed CAD model (Figure 7.2) consists of two layers: intestinal lumen and intestinal wall. It should be noted that the modelled intestine did not correspond to the actual length of the real intestine and did not cover the whole abdomen cavity. We fixed the model in the middle of the cavity by ignoring each phantom's intestine

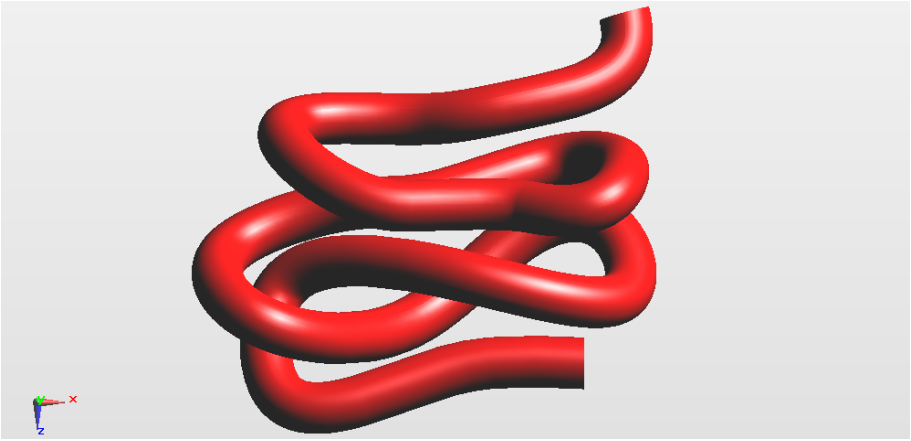

FIGURE 7.2: Small intestine CAD model

and lumen. In some parts of the abdomen, the intestine model overlapped the other tissues. This can be easily remedied by defining the highest priority to our intestine model rather than the other tissues. The dielectric properties of each tissue layer were assigned to the corresponding tissue according to the database provided by SEMCAD.

7.2.3 Capsule Endoscopy

The capsule endoscope was also modelled as a 26 mm × 11 mm hollow cylindrical object with two layers (Figure 7.3). The external layer of the capsule should be made of bio-compatible materials, so diamond was defined for the "material type" of the external layer. The interior layer was defined as a Perfect Electric Conductor (PEC). An edge source was also embedded inside the hollow part of the capsule for the purpose of measuring S-parameters. In this way our capsule model would be more realistic.

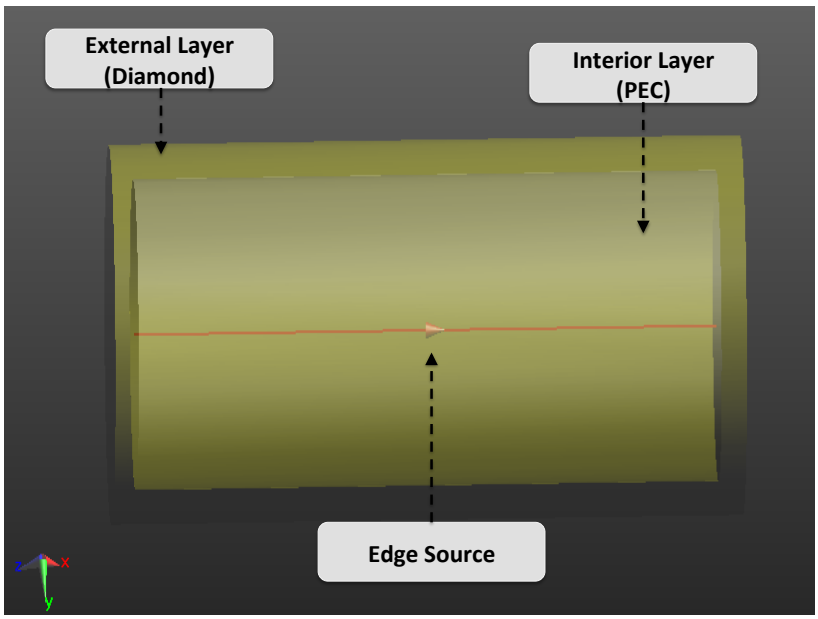

Figure 7.3: Schematic of the designed capsule endoscope

7.3 Sensitivity Analysis

7.3.1 Setting Process

In the FDTD technique the model and its surrounding computational domain need to be segmented into several cells to be able to apply and solve Maxwell's equations. On the other hand, SEMCAD X can support a full 3D ACIS-based modelling environment. This allows users to refine the grid without any restriction, rather than being tied to a predefined grid. There are four different options for the local grid setting in SEMCAD. These options can be used in a case when the grid generated by the default setting is not appropriate enough. Therefore a designer is able to add further refinement to the grid for each individual solid. The different grid setting options can be summarised as [138]:

- **Regional only:** In this setting no baselines are considered for the grid generation. In general a baseline is considered as a helper line, which is generated from a most-significant solid's geometric corners, angles or bounding-box information. The grid generator normally uses the baseline during grid-line computation. However in the "regional only " setting no baseline is generated. Moreover, in this setting the MAX step (maximum grid cells with default value of 0.07 wavelength) will be applied in the entire region. By default "regional only" is applied for dielectric and dispersive solids. It should be noted that, for any complex design which has various parts, assigning this setting to the less important parts will significantly reduce the number of baselines and help the grid generator to resolve the most important details of the model structure.

- **Bounding Box:** In contrast to the previous grid-setting option, in this setting the baselines are generated on the bounding box of the solid. By default this option is applied for PEC and PMC solids as well as Field and Port sensors.

- **Bounding Box (baseline enforced):** In this setting, for each solid upper and lower bounding-box baselines with a reference weight of 2000 are generated. This reference weight is the highest weight that can be used in SEMCAD and will be used when the distance between two baselines is close to the baseline resolution. Considering a proper reference weight assists the gridder to decide which baseline can be ignored according to its reference weight priority. By default this setting will be applied for sources and lumped elements.

- **Geometrical:** In this setting a geometric analysis is done for the solid first and the grid is then generated accordingly. In addition, in this setting it is possible to set some more geometric features to define further grid for the slot, thickness and curvature of a solid. This option might not be a suitable option for CAD parts as the grid might be over-refined.

In our simulations the capsule is moving inside the small intestine and the path loss needs to be measured with respect to each capsule location. Therefore the grid needs to be set in a way that can be optimal for all capsule locations. There are different approaches to setting the grid, but the most straightforward is to refine the grid for the intestinal part, since the capsule will always be inside it. In this way, all the simulations can have a uniform grid that is independent of the capsule location. As mentioned before, the intestine is designed as a two-layer object. For grid purposes it is not necessarily required to define the same setting for both intestinal layers, because a defined grid for an object can influence the other solids around it. We only refined the grid for the small intestine lumen, which affects all objects around it, such as the capsule and the intestinal wall.

On the other hand, the huge size of the simulations and the long processing time are the major limitations for solving such complex problems. In our case, the models have a high resolution, thus the number of cells is huge and it would take around a month to do a single simulation. However, SEMCAD X, which is bundled with the CUDA library, makes it possible to use the hardware acceleware to speed up the simulation. Our simulation computer was equipped with the NVIDA GPU (Graphics Processing Unit) which assisted us to accelerate our simulations. The only problem is that a system with one GPU can support a maximum problem size of 150 million. Therefore, in all our settings the number of cells should not exceed 150 million. To define a fine voxelling for the intestine, different grid types such as "Regional only" and "Bounding Box" were tested to compare the sensitivity of the selected methods on the voxelling and simulated results.

Figures 7.5 - 7.6 illustrate the results of different grid settings for the Duke, Ella and Billie phantom models.

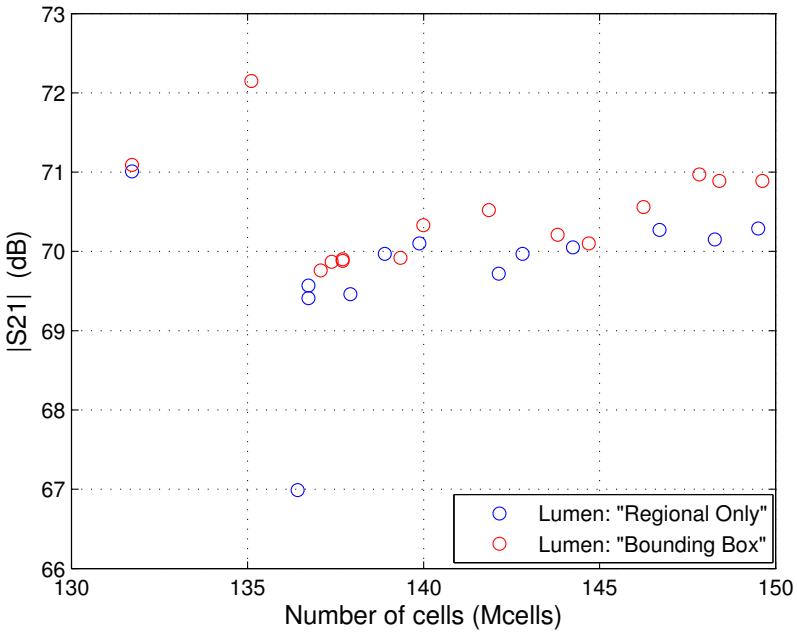

FIGURE 7.4: Sensitivity test for Duke's phantom model

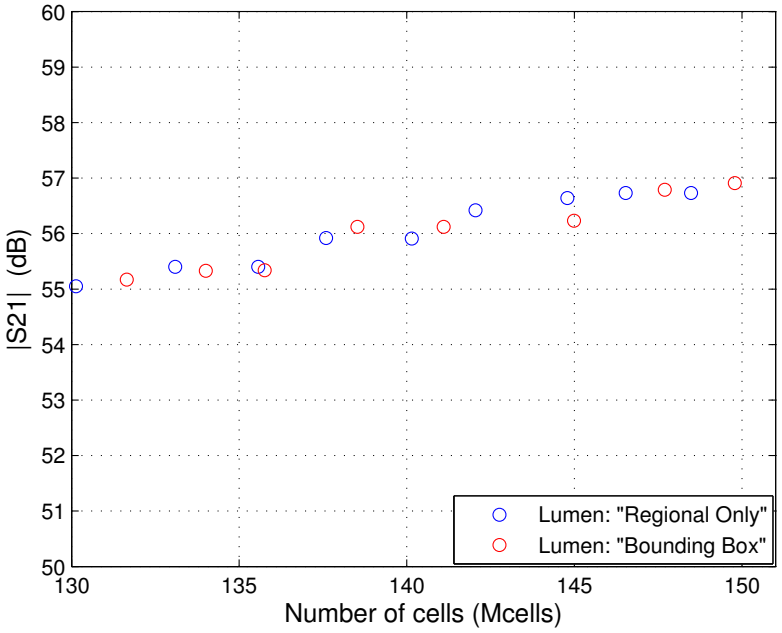

FIGURE 7.5: Sensitivity test for Ella's phantom model

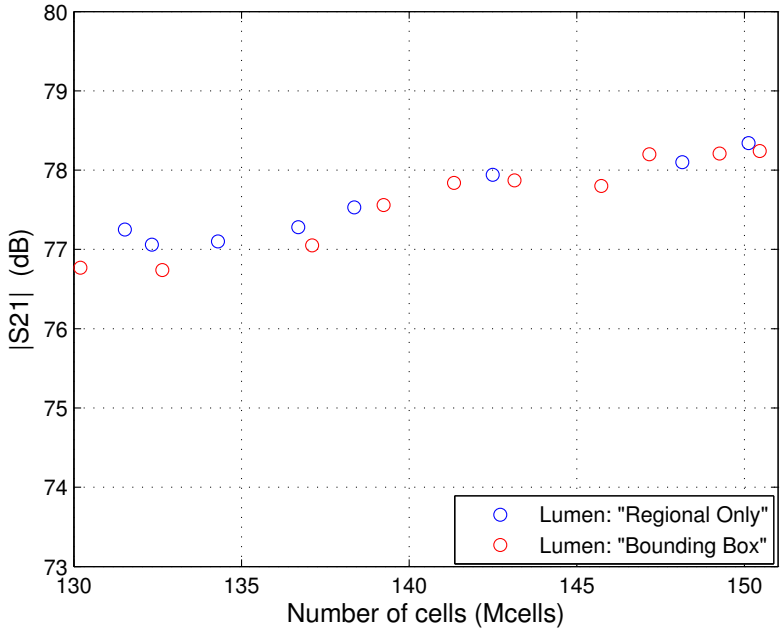

Figure 7.6: Sensitivity test for Billie's phantom model

7.3.2 Discussion of Results

It can be seen in all figures (Figure 7.5 - Figure 7.6) that $|S_{21}|$ follows a stable trend for higher cell numbers. For the case of the Ella and Billie models, about 2 dB of variation in the path loss was observed when the number of cells was changed by 20 Million, whereas the variation in path loss is around 4 dB for the same changes in cell numbers in the Duke model. This is mainly because Billie and the Ella have a similar tissue distribution in their abdominal model which is different from the Duke model. It should be also noted that, for less than 130 million a significant fluctuation in loss was observed in all three models. This brings about more than 5 dB differences in path loss compared to the loss for 150 million cells. These results demonstrate how the precise grid setting and the number of cells can effectively influence the simulated results. Thus, by selecting a large number of cells, less error can be observed in the simulations. Moreover according to the obtained results the best possible grid setting for Duke model can be achieved when the total size of the computational domain is set as $452 \times 258 \times 1258\ mm^3$, with a minimum cell size (step size) of 0.4 mm in respect to the signal wavelength. For the Ella and Billie models the computational domains should be defined as $422 \times 257 \times 1134\ mm^3$ and $383 \times 240 \times 1029\ mm^3$ respectively.

7.4 Estimation of Error in Loss and Ranging

In the next part of our study, in order to show how different grid sizes can influence the simulated results, two different sets of simulations have been conducted on our two female abdomen models (Ella and Billie) to measure the path loss between the external antenna and the capsule located inside the small intestine. The capsule was positioned in 28 different locations in the small intestine and S_{21} was recorded for all these locations. The first set of simulations was done by applying the best possible settings for the models. To derive the loss error caused by different settings in our female subject, we have repeated the simulations when the best possible grid for Duke was applied to both models. It should be noted that, since the Ella and Billie models have a smaller body than the Duke model, it is not possible to apply the best grid setting of those models to Duke as the grid size exceeded 150 Mcells. Hence, we have decided to select the best Duke's grid setting for the other two phantoms and estimate the error for the Ella and Billie models. It is obvious that, by applying the best grid setting of Duke to the Ella and Billie, different number of cells are produced on them.

Table 7.2 shows the number of cells in the Ella and Billie models with two different grid settings.

TABLE 7.2: Cell numbers in female subjects according to different grid setting

	Cell Numbers	
	Best Possible Grid Setting	**Duke Best Grid Setting Applied**
Ella	146	123
Billie	150	94

7.4.1 Results for Ella Model

As can be seen in Figure 7.7, the obtained losses for our two different simulations are not the same, which indicates how different numbers of cells in the phantom models can influence the measured results. To determine the best possible fit for all of the obtained results, both the graphical and the numerical analysis have been done on many different fitted curves. The numerical analysis included an evaluation of the confidence bound with a certainty level of 95% on the fitted coefficients and the goodness of the

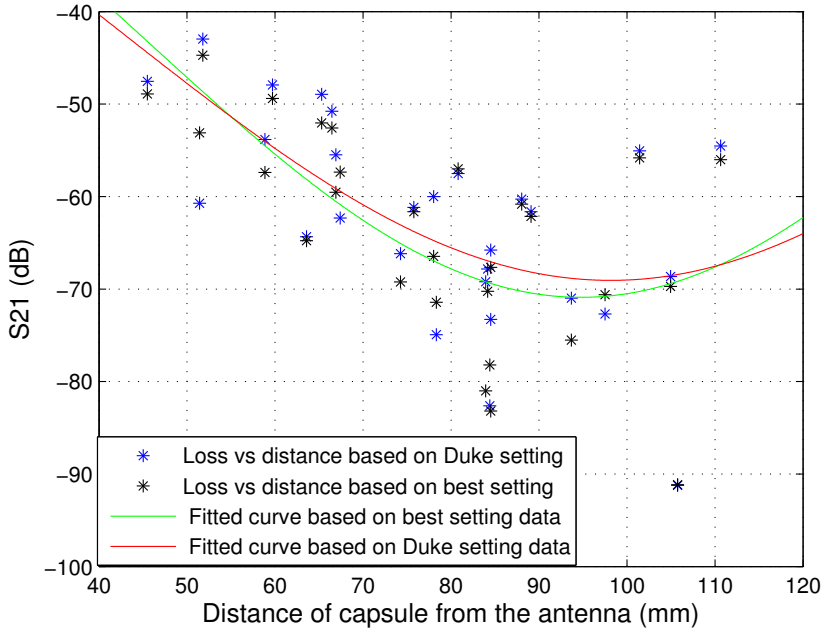

Figure 7.7: Loss versus distance for Ella model with two different grid settings

fit statistics. These results suggest that the Gaussian is the best fitted curve for the loss vs distance for both settings.

In order to determine whether the obtained losses in two different grid settings have a common distribution, a Quantile-Quantile (Q-Q) plot was provided. Figure 7.8 shows the Q-Q plot of loss for the Ella model. It demonstrates that the distribution of losses for both grid settings in the Ella model fell near the reference line. This proves that the loss in these two different settings has a common normal distribution. On the other hand, a Mean Absolute Error (MAE) of 3.05 dB was obtained with respect to a 23 Mcells difference in the number of cells compared to the best possible cell number for Ella. This shows that, for the Ella model, the error in loss with the Duke grid settings is about 3 dB when the capsule travels 80 mm along the small intestine.

To estimate the error in distance estimation caused by different grid settings on the Ella model the Cumulative Distribution Function (CDF) was plotted. Figure 7.9 depicts the CDF plot of the distance error for our two scenarios (Ella with Duke's and her best grid settings). The distance errors were calculated by getting the difference between the estimated distances of our two mentioned grid settings. The obtained mean of the distance error is about 19.58 mm. The CDF plot assures us that with 95%

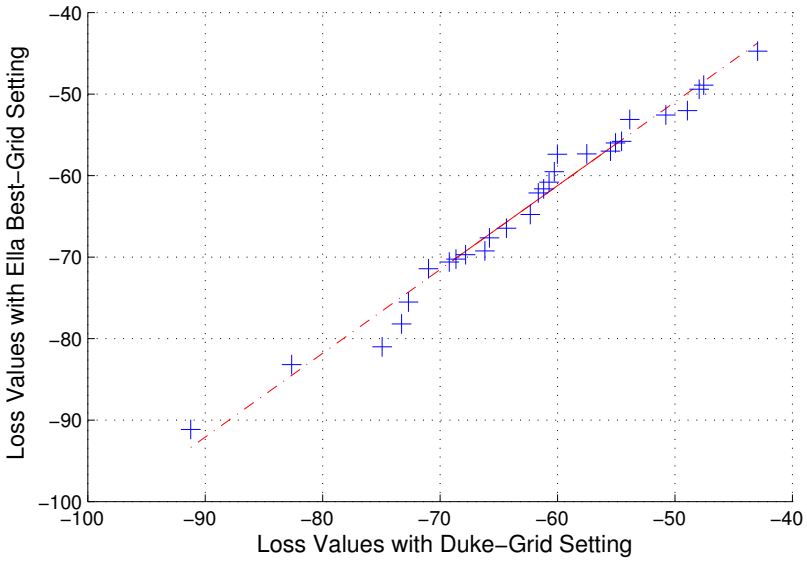

FIGURE 7.8: QQ plot of loss in Ella with different grid settings

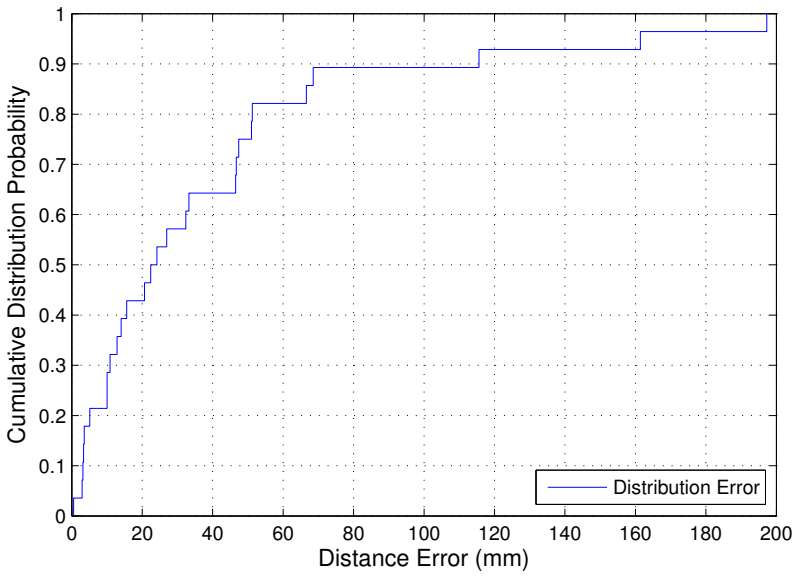

FIGURE 7.9: CDF of distance error in Ella

probability the distance error because of different grid settings is less than 160 mm.

7.4.2 Results for Billie Model

Figure 7.10 shows the simulated results for loss and their fitted curves for the abdomen area of Billie according to two different settings in the number of cells.

As can be seen, the obtained losses for our two different simulations are not the same, which indicates how different numbers of cells in the phantom models can influence the measured results. To determine the best possible fit for all of the obtained results, both the graphical and the numerical analysis have been done on many different fitted curves. The numerical analysis included an evaluation of the confidence bound with a certainty level of 95% on the fitted coefficients and the goodness of the fit statistics. These results suggest that the Gaussian is the best fitted curve for the loss vs distance for both settings. A Mean Absolute Error (MAE) of about 4.03 dB was calculated with respect to a 56 Mcells difference in the number of cells compared to the best possible cell numbers for Billie.

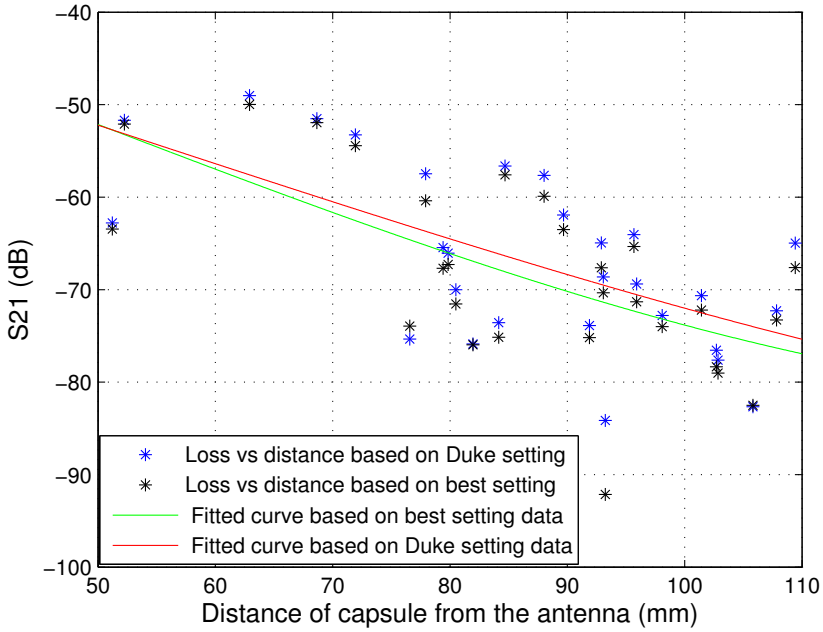

Figure 7.10: Loss versus distance for Billie model with two different grid settings

In order to determine whether the obtained losses in two different grid settings have a common distribution, a Quantile-Quantile (Q-Q) plot was provided. Figure 7.11 shows the Q-Q plot of loss for the Billie model. It demonstrates that the distribution of losses for both grid settings in the Billie model fell near the reference line. This

proves that the loss in these two different settings has a common normal distribution.

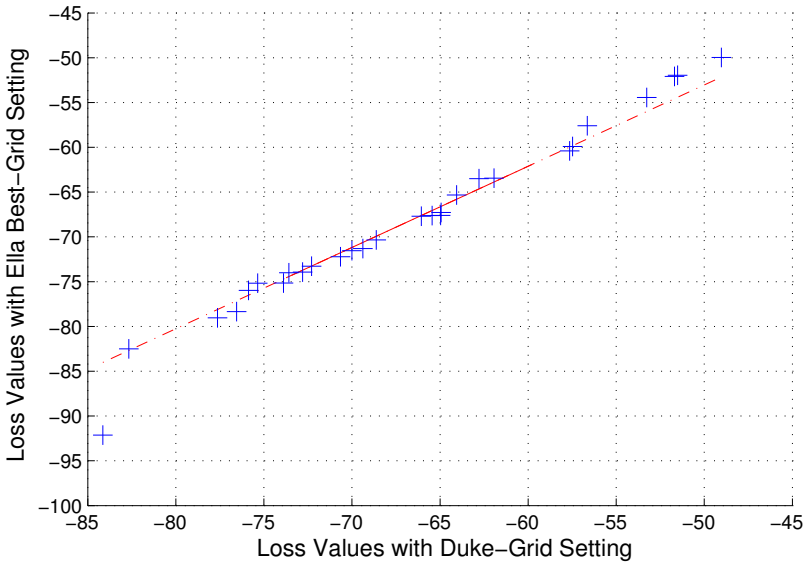

FIGURE 7.11: QQ plot of loss in Billie with different grid settings

To estimate the error in distance estimation caused by different grid settings on the Billie model the Cumulative Distribution Function (CDF) was plotted. Figure 7.12 depicts the CDF plot of the distance error for our two scenarios (Billie with Duke's and her best grid settings). The distance errors were calculated by getting the difference between the estimated distances of our two mentioned grid settings. The obtained mean of the distance error is about 7.57 mm. The CDF plot assures us that with 95% probability the distance error because of different grid settings is less than 25 mm.

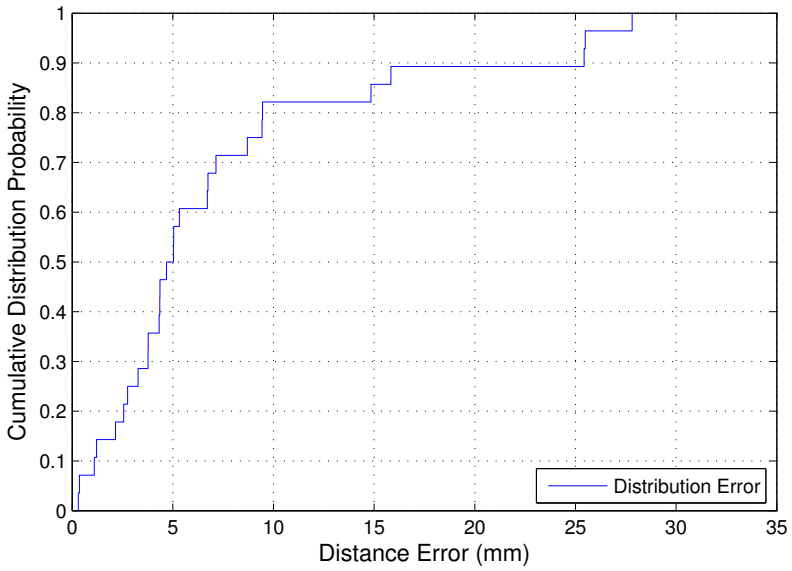

Figure 7.12: CDF of distance error in Billie

7.5 Chapter Summary

This chapter presents a comprehensive sensitivity analysis of the most influential risk factors for different human phantom models, in electromagnetic simulations using the FDTD method. Sensitivity analysis is helpful to develop an efficient parameter selection method to minimise the possible error in path loss during the simulation process and distance estimation. The obtained results confirm that sensitivity analysis is capable of identifying the significant risk factors, including the number of cells and voxelling, which influence the simulated results. Moreover, the results show that the distribution of loss has a stable trend by selecting a higher number of cells in both human models. Therefore it is crucial to consider the best possible number of cells and voxels for the model to reduce or eliminate the error caused by the simulation.

For the Billie model an mean absolute error of 4 dB in loss was observed with a 56 Mcells variation in the number of cells. Moreover, according to the CDF plots the distance error because of the different grid settings was less than 25 mm with a 95% probability. However, for the case of the Ella model, a mean absolute error of 3 dB in loss was observed when a 23 Mcells variation in the number of cells was applied. Moreover, according to the CDF plots the distance error because of the different grid settings was less than 160 mm with a 95% probability. As can be seen, the error in distance for the Ella model is more than for the Billie model and it shows how important

the grid setting is when we have a bigger object in our simulation environment.

Overall, these results can be considered as a guideline for future study, since practical measurements are not straightforward for in-body applications. Thus the numerical simulations can provide some level of insight into signal propagation inside the human abdomen.

Publications pertaining to this chapter:

- P. Ara, S. Cheng, M. Heimlich and E. Dutkiewicz, "Sensitivity analysis of human phantom models for accurate in-body path-loss model development," *Personal, Indoor, and Mobile Radio Communications (PIMRC), 2015 IEEE 26th Annual International Symposium on*, Hong Kong, 2015, pp. 1328-1332.

- P. Ara, S. Cheng, M. Heimlich and E. Dutkiewicz, "Grid sensitivity analysis of human phantom models to minimize the simulation error for capsule endoscope localization," *2015 15th International Symposium on Communications and Information Technologies (ISCIT)*, Nara, 2015, pp. 295-298.

8

Statistical Abdomen Path-loss Model for Different Human Subjects

8.1 Introduction

To improve the accuracy of RF-based localisation techniques in the GI tract, the primary focus should be on the investigation of radio propagation inside the human body, specifically in the digestive tract, to evaluate the impact of each tissue layer on the propagation. Therefore it is necessary to have an accurate propagation-based channel model before any specific localisation technique can be investigated.

Modelling an accurate radio channel for in-body communication is a challenging task. This is mainly because there is still a lack of physical measurements and analysis on the real human body due to technical and ethical issues. Therefore most of the proposed in-body channel models are focused on theoretical analyses or numerical simulations of electromagnetic wave propagation through the human body by using different digital anatomical human phantom models as well as different electromagnetic simulation software. Referring to our study in Chapter 6, we came to the conclusion that a deterministic path-loss model, which is only dependent on a theoretical analysis of radio-wave propagation inside the abdomen area, cannot fully achieve the desired

accuracy of a model specifically for location estimation of a capsule endoscope inside the small intestine.

In this chapter we develop a statistical path-loss model for three different anatomical human models by applying electromagnetic simulations using the FDTD method at 2.4 GHz. Using different anatomical models allows us to evaluate the statistical propagation models for individual human subjects. To perform a comprehensive study on the propagation of the signal in the abdominal region and construct a realistic framework, the designed generic small-intestine model (Figure 7.2) was embedded inside the abdomen cavity of the phantom models. A mathematical expression for the path-loss model was proposed based on analysis of the simulated loss at different capsule locations inside the small intestine. The proposed path-loss model is a good approximation to in-body RF propagation, since real measurements are quite infeasible for a capsule endoscopy subject.

8.2 Statistical Human Abdomen Path-loss Model

For capsule endoscope localisation several efforts have been made to develop an appropriate path-loss model for the GI tract, summarised in Chapter 2. All the discussed studies investigated the characteristics of signal propagation in different parts of the GI tract. The studies were conducted at various frequencies and depths. However, the most critical part for localising the capsule in the GI tract is the small intestine, due to its complicated structure. Thus it is absolutely necessary to develop a customised path-loss model for this anatomical organ.

Although all these simulation-based studies have addressed the in-body path loss for the digestive tract, a single human phantom model was analysed in each study. This issue is one of the controversial concepts of these path-loss models, since it is not exactly evident whether these models are subject-specific or can be generalised for all human phantoms. The evaluation of the suggested path-loss model on different human phantoms can greatly help to validate a model, because it is practically impossible to be done on a real human body.

Apart from this, regardless of the selected electromagnetic simulation software in all the aforementioned studies, there is no satisfactory discussion on the selected mesh size for their anatomical model, which can greatly influence the accuracy of the results.

This section presents our comprehensive study on three different human phantom models to develop a statistical path-loss model for the small-intestine area.

8.2.1 Simulation Setup

The three different phantom models "Ella", "Billie" and "Duke", which were created by the ITIS Foundation [137] and supported by SEMCAD software, were employed for this part of our study. According to our results from Chapter 7, by choosing the best possible grid size for our three human models the total size of the computational domain for the Duke model reaches $452 \times 258 \times 1258$ mm^3, with a minimum cell size (step size) of 0.4 mm for the chosen signal wavelength. For the Ella and Billie models the computational domains are $422 \times 257 \times 1134$ mm^3 and $383 \times 240 \times 1029$ mm^3 respectively. The capsule was positioned in 28 different locations in the small intestine (Figure 7.2) and S_{21} was recorded for both phantom models.

To present a better view of the capsule movement inside the abdomen area, the path loss was expressed in cylindrical coordinates. In cylindrical coordinates, see Figure 8.1, each capsule location can be shown as (r, ϕ, z), where r is the radial distance, which is the Euclidean distance from the z axis to the capsule. ϕ is the azimuth angle and expresses the angle between the reference direction on the xy-plane and the line from the origin to the projection of the capsule on the xy-plane. z is known as the height and shows the distance from the xy-plane to the capsule.

8.2.2 Path-loss Model for the Male Subject

The propagation loss S_{21} was measured between different capsule locations and the on-body receiver antenna. Figure 8.2 shows the path loss versus the radial distance between the capsule and the receiver antenna for our male-subject model (Duke).

The mathematical model of the path loss for the capsule endoscope at different radial distances from the external antenna, based on the best fitted line, can be written as a Gaussian function, expressed as:

$$P_{L[dB]}(R) = a_1 \exp\left(-\frac{(R-b_1)^2}{c_1^2}\right) \tag{8.1}$$

where R is the radial distance of the capsule from the antenna, a_1 and b_1 are the height and the centre positions of the curve peak respectively, and c_1 is the width of the curve.

On the other hand, the loss is not only dependent on the radial distance of the capsule from the antenna, but also depends on the azimuth angle, which is the angle between the capsule and the antenna. Figure 8.3 shows the loss versus the angle in the

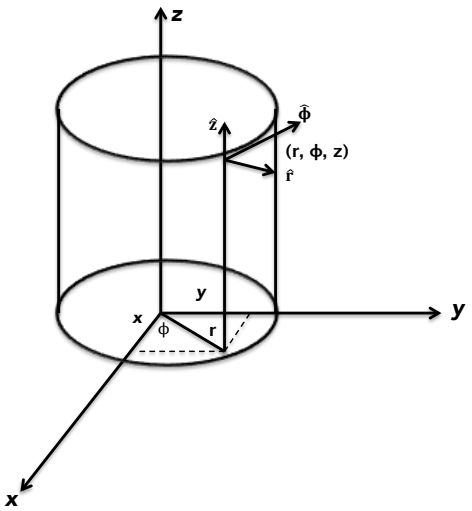

Figure 8.1: Cylindrical Coordinates

Duke phantom model.

As can be seen from this figure the distribution of the loss vs angle is between -40 and -90 dB. The obtained loss versus angle in the Duke phantom model can be fitted by a sum of sine functions with one term as follows:

$$P_{L[dB]}(\theta) = a_2 \sin(b_2\theta + c_2) \tag{8.2}$$

where a_2 is the amplitude, and b_2 and c_2 are the frequency and the phase constant of the sine wave respectively.

It should be mentioned that the distance and angle between the capsule and receiver antenna can be obtained from the following equation:

$$R = \sqrt{r^2 + r_i^2 + 2rr_i\cos(\theta) + (z - z_i)^2} \tag{8.3}$$

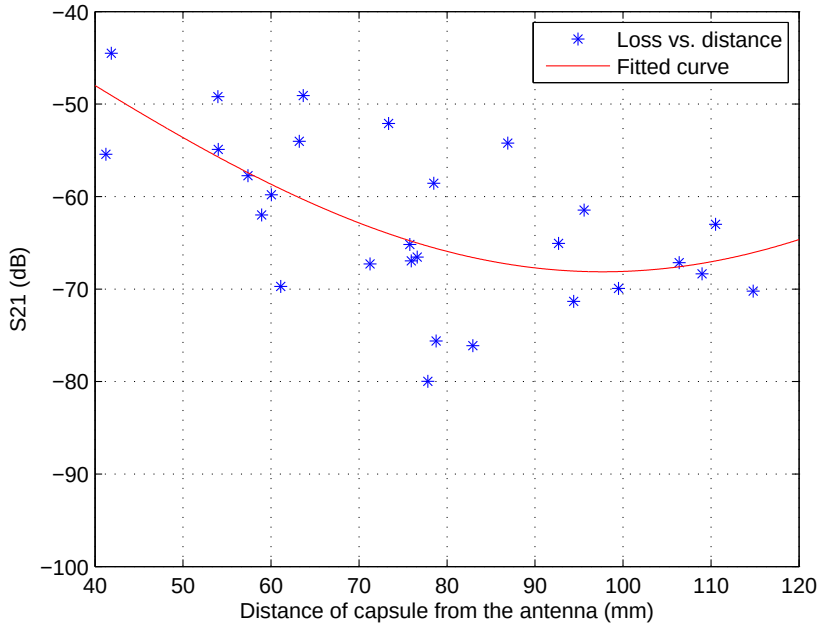

Figure 8.2: Loss versus distance for Duke model

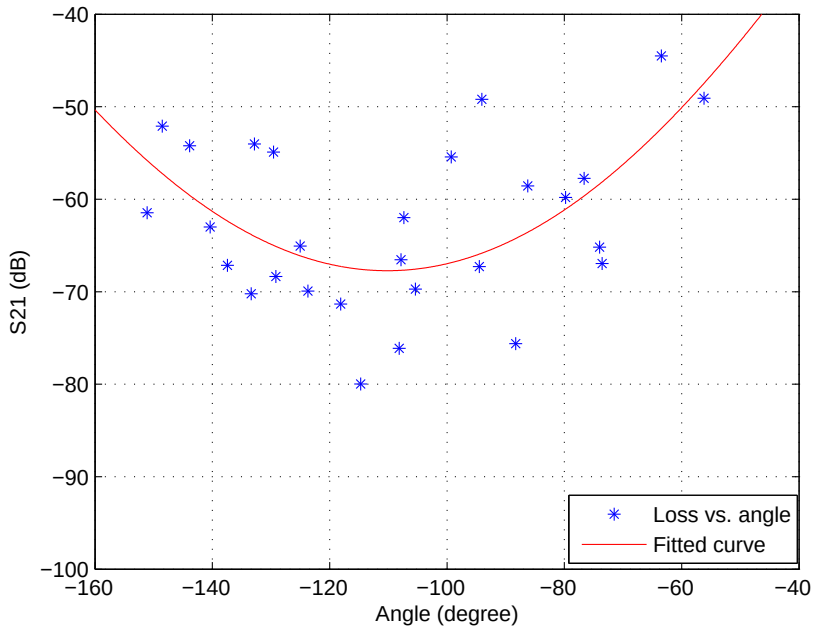

Figure 8.3: Loss versus angle for Duke model

where

$$\theta = \phi - \phi_i \tag{8.4}$$

Here r , r_i , ϕ, ϕ_i, z and z_i are the radial distances, azimuth angles and heights of the capsule and receiver respectively.

To be able to calculate the path loss at different capsule locations, we need to define a generic equation which includes both the distance and the angle in the form:

$$P_{L[dB]}(R,\theta) = a_1 \exp\left(-\frac{(R-b_1)^2}{c_1^2}\right) + a_2 \sin(b_2\theta + c_2) \tag{8.5}$$

Figure 8.4 illustrates the surface plot generated by the fitted path-loss model for the Duke phantom model. The path-loss coefficient values are given by Table 8.1.

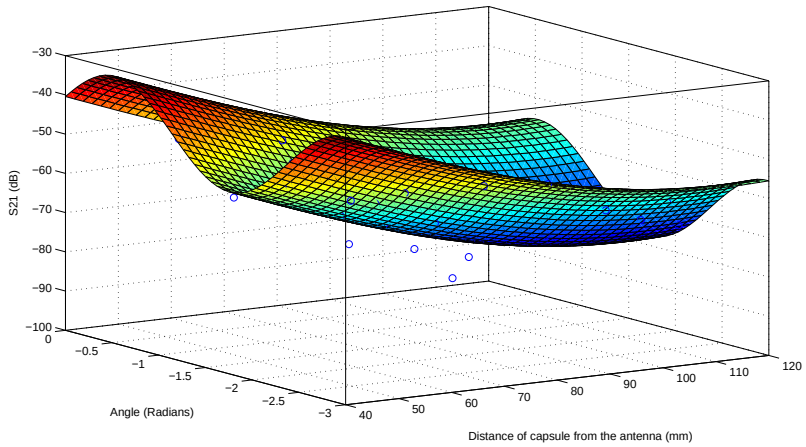

Figure 8.4: Surface plot fitted to the path loss for different radial distances and angles for Duke model

8.2.3 Path-loss Model for the Female Subject

Similarly to our male subject, the propagation loss S_{21} was simulated between different capsule locations and the on-body receiver antenna for our female subject (Ella). Figure 8.5 shows the path loss versus the radial distance between the capsule and the receiver antenna.

Surprisingly, the mathematical model of the path loss for the capsule endoscope at different radial distances from the external antenna, based on the best fitted line, for our female subject can also be written as a Gaussian function (Equation 8.1). On the

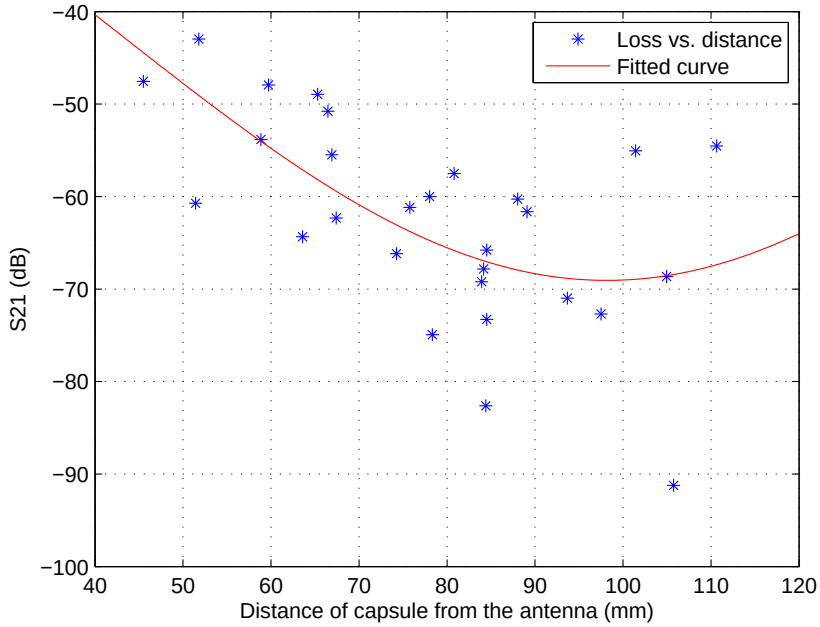

Figure 8.5: Loss versus distance for Ella model

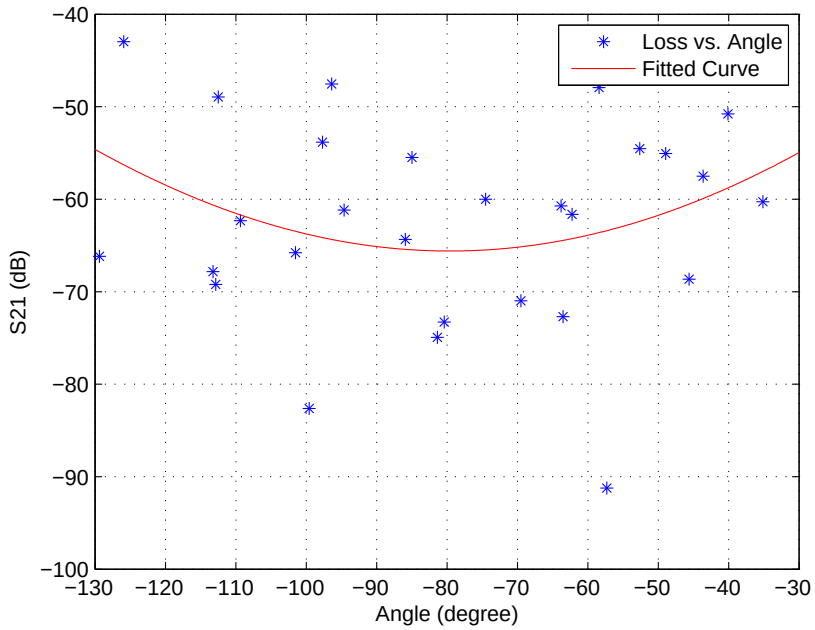

Figure 8.6: Loss versus angle for Ella model

other hand, similarly to the Duke model we observe that the loss also depends on the azimuth angle between the capsule and the antenna. Figure 8.6 shows the loss versus the angle in the Ella phantom model.

As can be seen from this figure the distribution of the loss vs angle is between -40 and -90 dB. The obtained loss versus angle can be fitted by a sum of sine functions with one term (Equation 8.2). Hence the total path loss at different capsule locations can be calculated according to the generic Equation 8.5. Figure 8.7 illustrates the surface plot generated by the fitted path-loss model for the Ella phantom model. The path-loss coefficient values are given by Table 8.1.

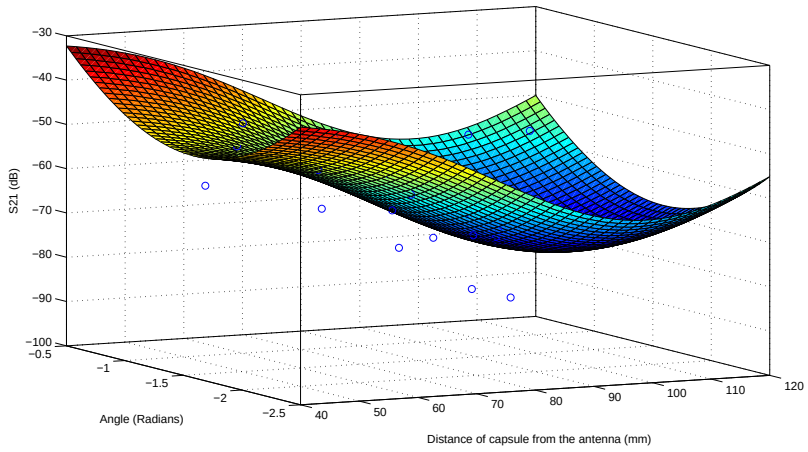

Figure 8.7: Surface plot fitted to the path loss for different radial distances and angles for Ella model

8.2.4 Path-loss Model for the Child Subject

For our child phantom model (Billie) we repeated the simulations at 28 different capsule locations to measure S_{21}. Figures 8.8 and 8.9 show the path loss versus the radial distance and angle respectively between the capsule and the receiver antenna in the child subject.

Again a Guassian fit was the best possible fit for the obtained loss vs radial distance and a Sine function was the best-fit choice for the obtained loss vs angle. Therefore, similarly to our two previous adult phantoms, the total path loss at different capsule locations can be calculated according to the generic Equation 8.5. Figure 8.10 illustrates the surface plot generated by the fitted path-loss model for the Billie phantom

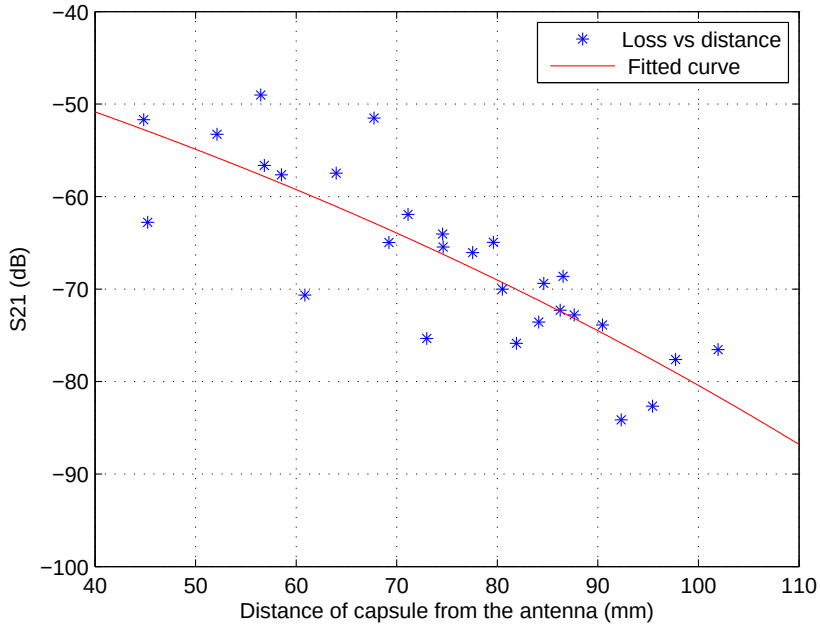

Figure 8.8: Loss versus distance for Billie model

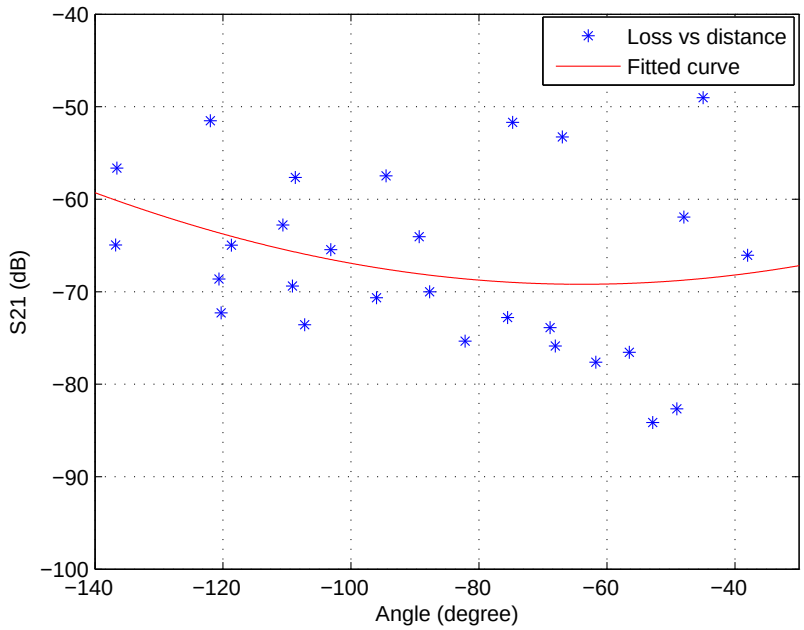

Figure 8.9: Loss versus angle for Billie model

model. The path-loss coefficient values are given by Table 8.1.

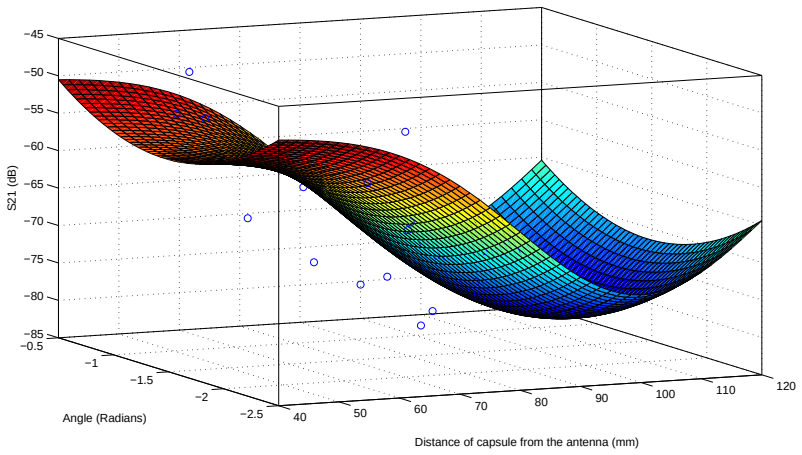

Figure 8.10: Surface plot fitted to the path loss for different radial distances and angles for Billie model

Table 8.1: Coefficient values for the path-loss model

	Coefficient Values					
	$\mathbf{a}_1$	$\mathbf{b}_1$	$\mathbf{c}_1$	$\mathbf{a}_2$	$\mathbf{b}_2$	$\mathbf{c}_2$
Ella	-27.73	98.97	35.85	48.02	0.8124	-0.2799
Billie	-24.09	100.4	28.92	56.35	0.4903	-0.8543
Duke	-66.65	112.5	108.8	10.86	2.558	2.923

8.3 Discussion

At first glance, it seems that the Duke model is overweight compared to the Ella model. But in fact the two studied models each have a normal weight. This can also be verified by calculating their Body Mass Index (BMI) [139, 140]. The calculated BMI for Ella and Duke are 21 and 22 respectively. This indicates that both models are of a normal weight. However the BMI for Billie is 16.5 which indicates that she is underweight.

In this situation we expected to observe a similar trend for the overall loss in both Ella and Duke models. As can be seen in Figures 8.2 - 8.5, the distribution of loss for the Ella model is between -40 and -90 dB and for the Duke model is between -40 and

-80 dB, which meets our expectations. Surprisingly the distribution of the loss for the Billie model is between -50 and -85 dB which is quite close to the loss distribution in the other two models.

Although less loss was expected in Billie compared to the other models, the obtained results are in contrast to our expectations. This comes back to two main reasons. The first important reason is related to the number of abdominal tissue layers. In the Billie phantom model more than three-quarters of the small intestine in the abdomen region is covered by connective tissue, which has dielectric characteristics similar to the muscle, as $\epsilon_r = 43$ and $\sigma = 1.64$ S/m at 2.4 GHz. This tissue layer can also be seen in the abdomen region of the Ella model but in lesser coverage, but there is no connective tissue in the same region of the Duke abdomen. As was shown in [141], muscle experiences higher loss than other tissues with less water, such as fat. Therefore a high amount of loss can be observed in Billie, due to the existence of an extra high-attenuation tissue layer located between the capsule and the radar antenna.

Another reason can be related to the thickness of the intestinal model. In the real scenario the thickness of the small intestine in children is less than in adults. In fact the length and width of the intestine in children both increase in their growth stage, similarly to their other organs [142]. Despite this fact the same size of intestine was used for all three models. Actually, for the Billie case, the free movement of the capsule inside the intestine was the main reason for using the same size of intestine model as for adults. Employing a thinner intestine was practically impossible, since it was required to fit the fixed-size capsule available on the market inside the small intestine.

However, decreasing the size of the capsule can be a suitable solution to deploying a thinner intestine model in simulation. But in a radar system the size of the object which is going to be localised can significantly influence the system accuracy. In a radar system one of the principal concepts is the Radar Cross Section (RCS). RCS is a measure that shows the detectability of an object. A target with a larger RCS can be more easily detected. Therefore decreasing the size of the capsule to be fitted inside the thinner intestine can influence the results.

On the other hand, for the case of Ella and Duke the overall behaviour of the loss distribution is similar. But comparing the exact point-to-point capsule location in these two adult models reveals that the amount of loss depends strongly on the tissue layers in the area of the measurements. Just as for the Billie model, the connective tissue can be seen in some parts of the abdomen region in the Ella model, and in the case of the Duke model some parts of the region were covered by tendon and ligament with dielectric properties of $\epsilon_r = 43$ and $\sigma = 1.64$ S/m. The Rectus abdominis is the

flat muscle which covers the whole front of the abdomen and is crossed by 3 bands named tendinous inscriptions [20]. A partial tendon layer can be seen in the Duke model while no tendon tissue is assigned for the abdomen of the Ella or Billie models. Both the connective tissue and the tendon are high-permittivity materials which cause higher attenuation. Therefore, in any location of the capsule where the abdomen is covered by any other of these tissues, the loss at that point is higher than for similar locations in the other models.

On the other hand, employing an in-body path-loss model which only depends on the distance between the capsule and a receiver's antenna can not accurately provide capsule position estimation. To show this important fact, the capsule in three different positions were depicted in which the loss is almost the same in all of these three points. These three points are marked red as shown in Figure 8.11. The related positions of the capsule in the small intestine are also illustrated in Figure 8.12. It can clearly be seen that, for all these three different capsule positions, the loss is -70 dB. Using the obtained path loss for the location estimation of the capsule just gives us one capsule position, whereas the capsule can be located in any of these three locations.

In general for any given body (male, female, child) it is not possible to simply use S_{21} to determine distance, as shown by the measurements and the lack of strong correlation. This result motivates the work to be presented in subsequent chapters to improve on raw RSS measurement results and provide more accurate localisation.

8.4 Chapter Summary

This chapter presents a new statistical in-body path-loss model for the human abdomen region. The proposed path-loss model was obtained from numerical FDTD simulations on three different human models at 2.4 GHz. Our results indicate that the path loss is highly dependent on both the radial distance and the angle of the capsule from the antenna. On the other hand the results confirm that for any given body (male, female, child) it is not possible to simply use S_{21} to determine distance.

The study shows that in 50% of the cases at the same capsule location in any of the models, the obtained loss is different. This is due to the fact that different human subjects are significantly different in terms of body mass and size. Also, human abdomen tissues are not uniform in the abdomen region, and this can influence the radiation characteristics. This concept is also verified from our results, that the percentage of high-attenuation abdominal tissues such as muscle can significantly affect

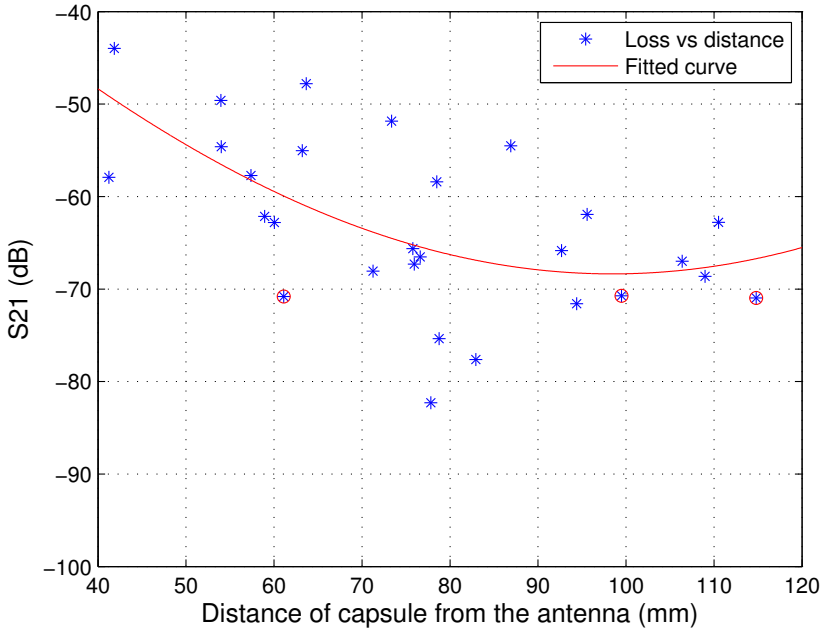

Figure 8.11: Loss versus distance for Duke model

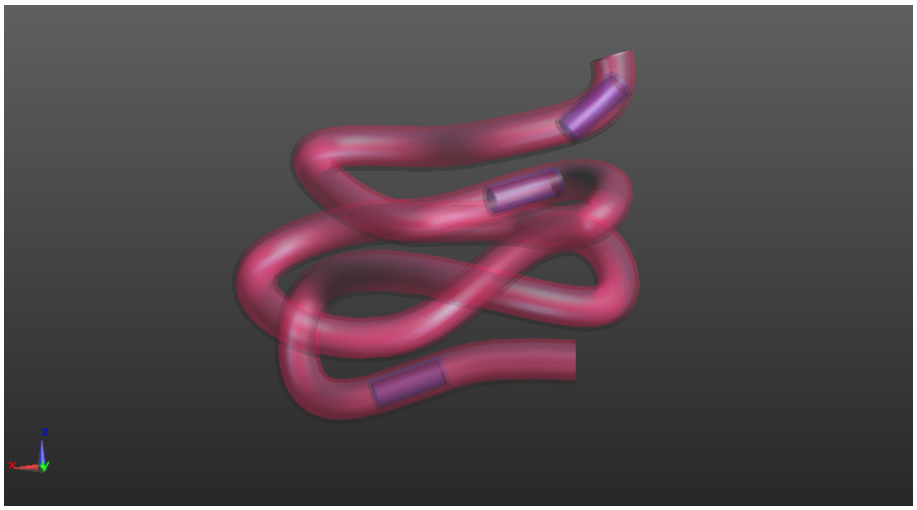

Figure 8.12: Small intestine CAD model with three different capsule locations

the abdominal path loss in different male and female subjects.

Overall, these results can be considered as a guideline for future study, since practical measurements are not straightforward for in-body applications. Thus numerical simulations can provide some level of insight into signal propagation inside the human abdomen.

Publication pertaining to this chapter:

- P. Ara, S. Cheng, M. Heimlich and E. Dutkiewicz, "Investigation of in-body path loss in different human subjects for localization of capsule endoscope," *2015 37th Annual International Conference of the IEEE Engineering in Medicine and Biology Society (EMBC)*, Milan, 2015, pp. 5461-5464.

9

Location Estimation of Wireless Capsule Endoscope

9.1 Introduction

Recent developments in capsule endoscopy have highlighted the need for techniques to estimate accurately the location of a capsule endoscope. A highly accurate location estimation of a capsule endoscope in the gastrointestinal (GI) tract within several millimetres is a challenging task, as radio-frequency signals encounter a high-loss propagation environment. So far different methods have been proposed to determine the location of a capsule in the digestive tract. None of them can, however, produce the required localisation accuracy of the order of a few millimetres except magnetic-based techniques. However employing a magnetic localisation technique for WCE is not very practical, as discussed in detail in Chapter 2.

This chapter presents a non-iterative position estimation method based on received signal-strength measurements to estimate the 2D location of a WCE inside the small intestine. The Levenberg-Marquardt algorithm, which is a Non-Linear Least Square (NLLS) method, was applied to solve the path-loss equation proposed in Chapter 8. The distance between capsule and receiver antennas then can be estimated as well as

the position of the capsule. On the other hand, the accuracy in the localisation system depends on a number of different factors such as the geometry of the nodes in the system, the method and algorithm that are used to process data, and the measurement accuracy of parameters (e.g. range, angle, and signal arrival time). Further, this chapter presents a discussion of system performance in terms of position determination precision. The Cramér-Rao Lower Bound (CRLB) method is then used to analyse the performance of the radar system in location estimation of a WCE. The CRLB is derived for three different scenarios, i.e. three cases of shadowing: constant variance, with parameter-dependent variance and with correlated and parameter-dependent variance.

9.2 System Model

Simulations are conducted using a 3D electromagnetic solver SEMCAD X employing FDTD techniques. To estimate the location of the capsule and derive the CRLB to benchmark the accuracy of location estimation for a WCE inside the small intestine, the simulations have been conducted for a 34-year-old male anatomical model "Duke", with a height of 177 cm and weight of 72.4 kg and with up to 77 tissue types. Since the phantom model was constructed based on MRI images and its small-intestine model does not support the desired resolution and segmentation to freely move the capsule to different intestinal sections, therefore we developed our own simple intestine CAD model and imported it to the abdomen of the human phantom model.

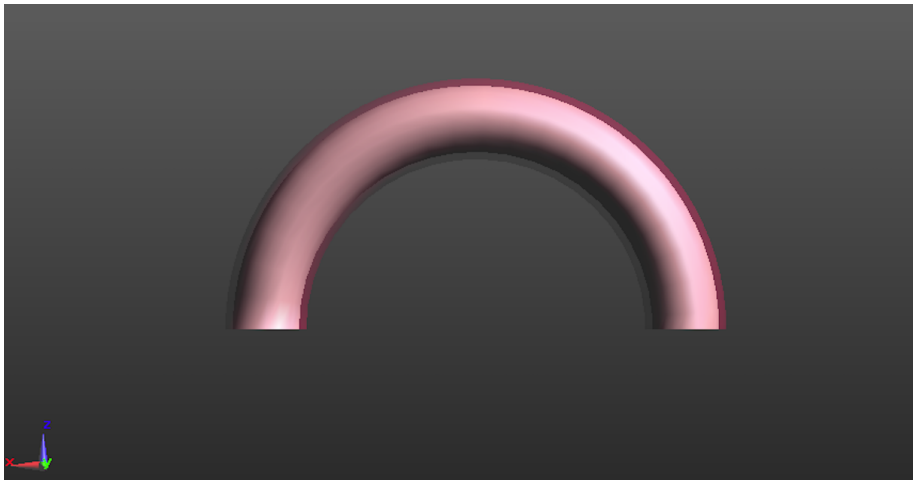

FIGURE 9.1: Small-intestine CAD model

Our developed CAD model (Figure 9.1) consists of two layers: intestinal lumen and

intestinal wall. It should be noted that the designed intestine does not correspond to the actual length of the real intestine and does not cover the whole abdomen cavity. We fixed the model in the middle of the cavity by ignoring the phantom's intestine and lumen. In some parts of the abdomen, the designed intestine model overlaps other tissues. This can be easily remedied by defining the highest priority to our intestine model rather than to the other tissues. The dielectric properties of each tissue layer at 2.4 GHz were assigned to its corresponding tissue according to the database provided by SEMCAD. The capsule endoscope which is the target object for our radar system was also modelled as a two-layer cylindrical object, with a diameter of 11 mm, along the length of the small intestine. As mentioned in Section 7.2.2, the external layer of the capsule should be made of bio-compatible materials, so diamond was defined as the "material type" of the external layer. The interior layer was defined as a Perfect Electric Conductor (PEC). About 55 edge sources (voltage sources) were also embedded inside the hollow part of the capsule for the purpose of measuring the scattering parameters as well as modelling the movement of the capsule at each instant.

In our scenario, the radar transmitter and receiver antennas are placed outside the human body. The signal is transmitted from one transmitter antenna and reflected signals are captured by a number of receiver antennas. The location of a capsule in the GI tract is estimated by processing the received reflected wave from the capsule. In fact a multi-channel radar system is considered, which can process the received signals from multiple antennas simultaneously. Moreover in this study, for simplicity in theoretical performance analysis, we ignore the probability of receiving multiple reflections from other human tissues and assume that the reflected signal from the capsule is our only received signal. The designed half-wavelength dipole antenna, operating at 2.4 GHz, with a height of 54 mm and radius of 1.5 mm (Chapter 5), was employed for these simulations as well. In order to contemplate a realistic situation and also to prevent the deteriorative effect of the human body on the antenna performance, the transmitter antenna was attached vertically into wool fabric with the thickness of 0.62 mm and positioned in front of the human abdomen. The vertical position of the antenna was chosen because, according to our past study [143], this is the best possible position. Moreover we considered three receiver antennas which were attached to the human abdomen as shown in Figure 9.2. It should be also pointed out that the distance (d) between the receiver antennas and the transmitter antenna was selected to follow the rule of ($d_{min} = \frac{D^2}{\lambda}$), where D is the effective area of the antenna, although in practice it is usually required to have $d > \frac{2D^2}{\lambda}$ [144].

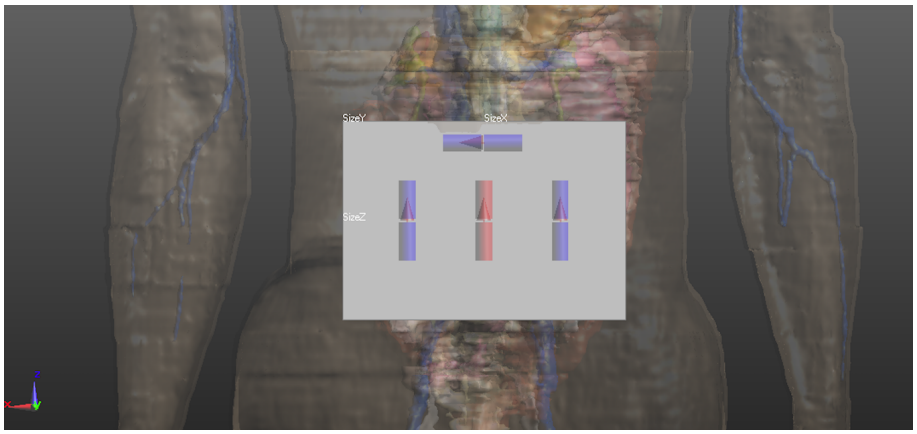

FIGURE 9.2: Illustration of antenna configuration: The transmitter antenna (red) is surrounded by three receiver antennas (blue)

The location estimation and derivation of the CRLB for a WCE were performed for a rectangular location area of 20 cm × 14 cm. UPML (Uniaxial Perfectly Matched Layers) absorbing boundary conditions were selected to truncate the computational domain. This works similarly to the absorber in an anechoic chamber and prevents wave reflection from the environment. The harmonic simulations were run at 2.4 GHz and the field distribution was recorded at different locations of the capsule inside the intestine.

9.2.1 Human Abdomen Path-loss Model

In Chapter 8 the statistical in-body path-loss model for the small-intestine region was derived. The derived path-loss model includes a dependency on both the distance and the angle between the capsule and a receiver antenna. The statistical model of the path loss can be written as

$$PL_i = a_1 \exp\left(-\frac{(R_i - b_1)^2}{c_1^2}\right) + a_2 \sin\left(b_2(\phi - \phi_i) + c_2\right) + S_i + n_i \tag{9.1}$$

where ϕ and ϕ_i are the azimuth angles of the capsule and the i^{th} receiver antenna respectively. a_1, b_1, c_1, a_2, b_2 and c_2 are the model coefficients. The male human phantom model (Duke) was employed for our investigation of capsule location estimation, and its related loss coefficients are listed in Table 9.1.

S_i represents lognormal shadowing with zero mean ($\mu_s = 0$) and a Standard Deviation (STD) of σ_s. n_i represents the measurement noise, with zero mean and an STD

of σ_n. The STD of the shadowing effect in this scenario was measured as 7 dB, while the average STD of the measured noise was about 12 dB. R_i is the distance between the capsule and the i^{th} receiver antenna, which in a cylindrical coordinate system can be defined as

$$R_i = \sqrt{r^2 + r_i^2 - 2rr_i \cos(\phi - \phi_i)} \tag{9.2}$$

where r and r_i are the radial distances of the capsule and the i^{th} receiver antenna respectively as shown in Figure 9.3.

Table 9.1: Coefficient Values for the Path-loss Model

	a_1	b_1	c_1	a_2	b_2	c_2
Duke Phantom	-66.65	112.5	108.8	10.86	2.558	2.923

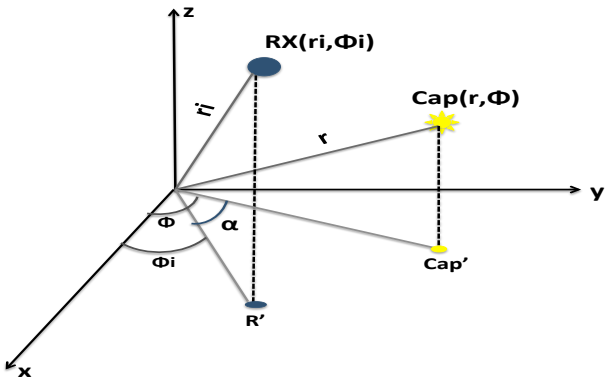

Figure 9.3: Capsule and receiver antennas' geometric positions in a cylindrical coordinate system.

9.3 Wireless Capsule Endoscope Location Estimation via Trilateration Method

In general, the lateration technique is a range-based technique in which the position of a target node can be estimated using the strength of the received signal from known-position reference nodes. Using the relationship between signal strength and distance that is normally obtained from a channel path-loss model, the distance between the target node and each reference node can be computed. The details of this technique were discussed in Chapter 2.

In this study the trilateration method was employed to estimate the location of the capsule in two dimensions. Note that in this section, for simplicity in analysis, Cartesian coordinates are used. Three half-wavelength dipole antennas were employed as the receiver antennas and attached to the abdomen of the human phantom model (Figure 9.2). These antennas are considered as our reference nodes with known location (x_i, y_i). The simulations were run and the loss (S_{21}) between each reference node and the capsule endoscope at each capsule location was recorded. In terms of the unknown location of the capsule, denoted as (x_c, y_c), and the known location of the reference nodes, the distance (R_i) between the capsule and the i^{th} reference node is simply given by

$$R_i^2 = (x_i - x_c)^2 + (y_i - y_c)^2 \tag{9.3}$$

Moreover, the azimuth angle between the capsule and each reference node can be calculated as

$$\theta_i = \tan^{-1}\left(\frac{y_i - y_c}{x_i - x_c}\right) \tag{9.4}$$

By substituting R_i and θ_i from Equations 9.3 and 9.4 into 9.1 the unknown location of the capsule (x_c, y_c) can be computed as follows.

$$\begin{aligned} P_{L[dB]}(x_c, y_c) = a_1 \exp\left(-\frac{(\sqrt{(x_i - x_c)^2 + (y_i - y_c)^2} - b_1)^2}{c_1^2}\right) + \\ a_2 \sin(b_2 \tan^{-1}(\frac{y_i - y_c}{x_i - x_c}) + c_2) + S_i \end{aligned} \tag{9.5}$$

It is obvious that a unique solution can not be found by using a single equation. Therefore by using more than one reference node we are able to form a system of non-linear equations. In general there are different algorithms to solve non-linear problems

(Equation 9.5). One of the most commonly used methods for position computation is the Non-linear Least Squares (NLLS) method which is a form of Least Square (LS) analysis. It is mostly used to fit a set of observations with a non-linear model which has n unknown parameters. Normally the number of observations should be more than the number of unknown parameters. The Levenberg-Marquardt algorithm, which is a NLLS method, was exploited to obtain the capsule position estimate. In the Levenberg-Marquardt algorithm the solution can be found by successive iterations, where at each iteration the system is approximated by a linear problem and the value of the unknown parameters is found in a way that minimises the sum of the squared differences between the actual and estimated data. It should be noted that to start the minimisation process using the Levenberg-Marquardt algorithm an initial guess of capsule position is needed. The error can be defined as

$$E = \sum_{j=1}^{m} [y_j - y_{LS}(p_j)]^2 \tag{9.6}$$

where $j = 1, 2, ...m$ is the index of a data point, y_j is the actual value of the variable and y_{LS} is the value predicted by the model at point p_j. It should be mentioned that in the NLLS method an initial value for each unknown parameter is required to initiate the minimisation process.

9.4 Numerical Results

In this section, we present our results obtained through simulations using SEMCAD X and MATLAB software. In our study we use the proposed path-loss model (Equation 9.1). By applying the non-linear squares method on our set of equations the location coordinates of the capsule at each position is estimated. The results show that the average distance error between capsule location and receiver antenna 1 is 6.98 mm, and 13 mm and 11 mm for receiver antennas 2 and 3 respectively. Figures 9.4 and 9.5 illustrate the location estimation error in the X and Y axes respectively. The calculated mean error is 21 mm and 7 mm for the X-axis and Y-axis respectively. Figure 9.6 depicts the distance between the true and estimated capsule positions. A mean distance error of 30 mm with an STD of 9 was obtained from the simulated data. The root-mean-square error (RMSE) is 31 mm. Figure 9.7 presents the cumulative distribution function of the distance error. As can be seen the CDF plot assures us

that, with 90% probability, the location estimation error is less than 4 cm.

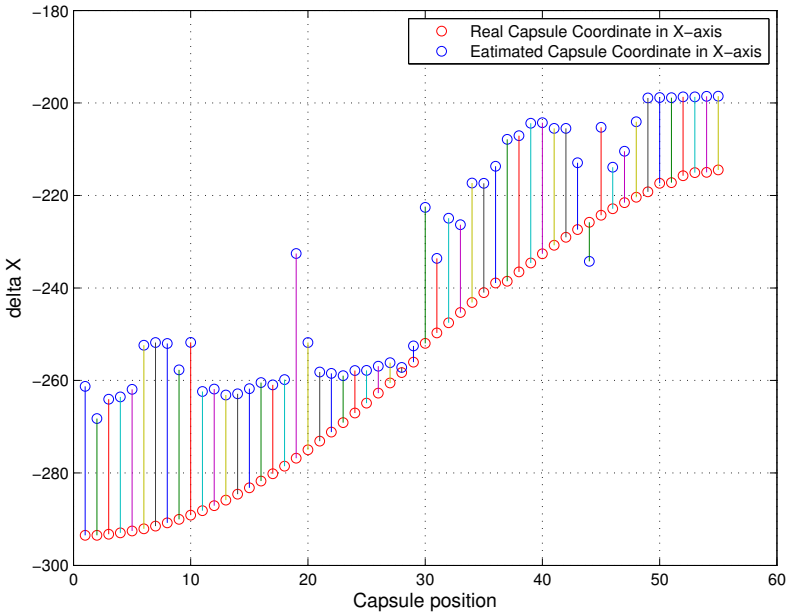

FIGURE 9.4: Position estimation error in X-axis

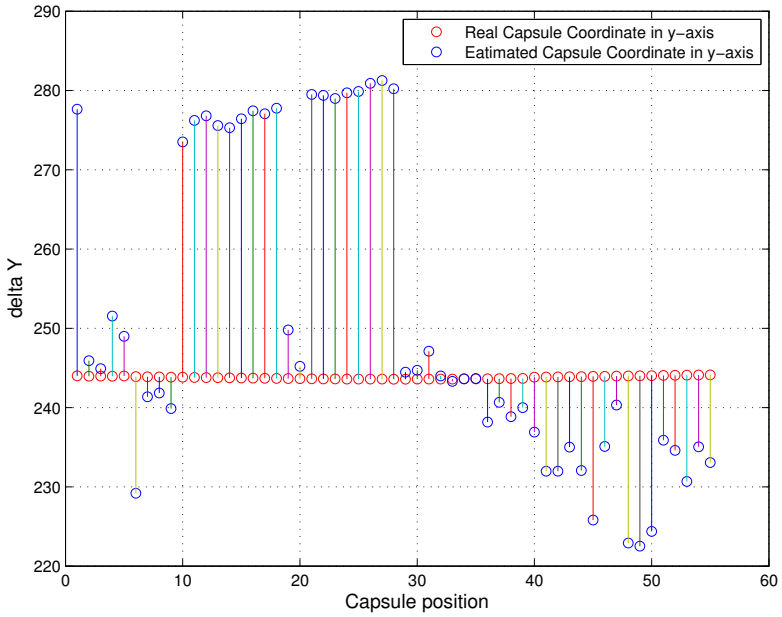

FIGURE 9.5: Position estimation error in Y-axis

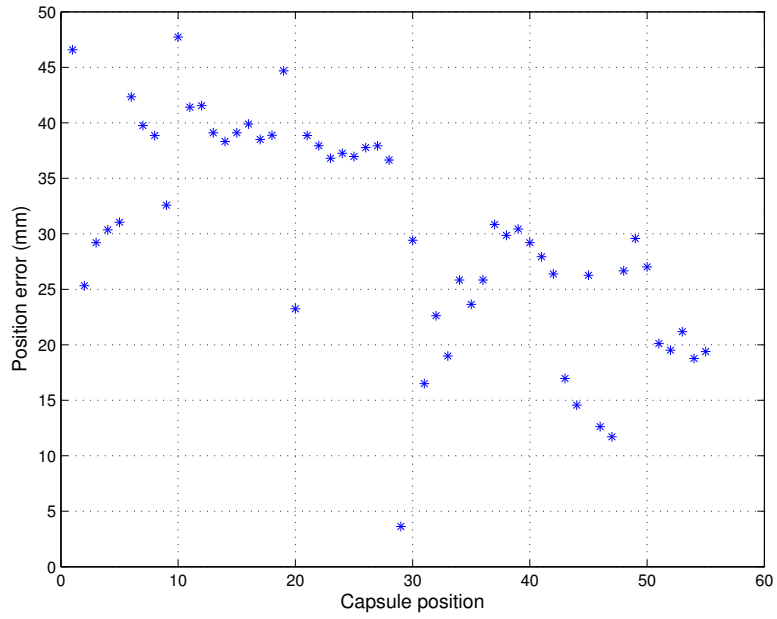

Figure 9.6: The distance between the true and estimated capsule positions

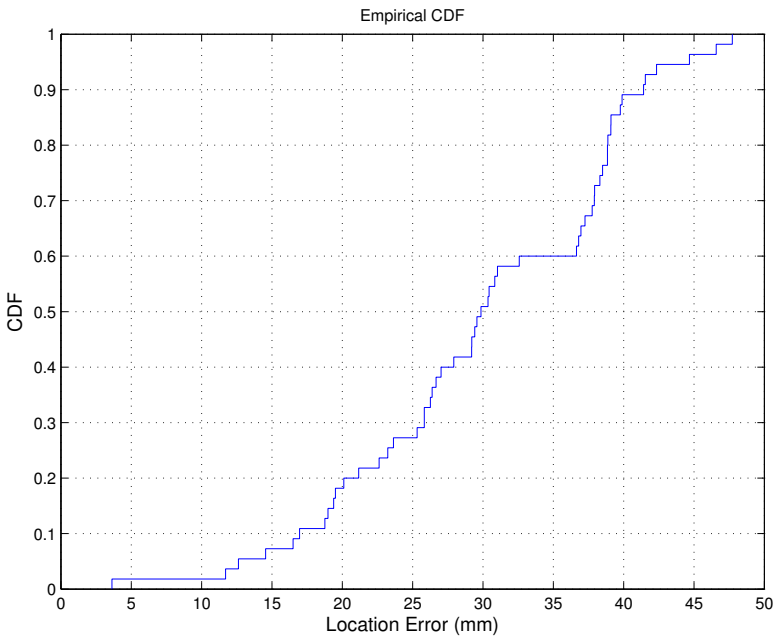

Figure 9.7: CDF of distance error

9.5 Localisation Error Versus Different Noise STDs

In this part the overall trend of localisation performance has been investigated in the presence of noise. We reveal how a noise component can influence the location estimation accuracy. In medical applications such as the capsule endoscopy procedure, noise mainly initiates and occurs from different sources like: electronic devices which are surrounded by or connected to the patient, body movement, bowel movement, intestinal gas and fluid, etc. It is obvious that minimising naturally present noise is out of our control. Therefore, to develop a high-performance communication system it is required to consider the noise effect on the performance of the system. We investigate how the accuracy of the capsule location estimation would be affected by the noise standard deviation. Figures 9.8, 9.9 and 9.10 illustrate the mean, standard deviation and RMSE of location error, as a function of path-loss noise STDs. As expected the mean, STD and RMSE of the WCE location error increase linearly with increase of the noise STD. It can also be seen that, in the worst case, when the noise STD is 20 dB, the system position error mean is about 24 mm with a standard deviation of 14 mm and an RMSE of 27 mm.

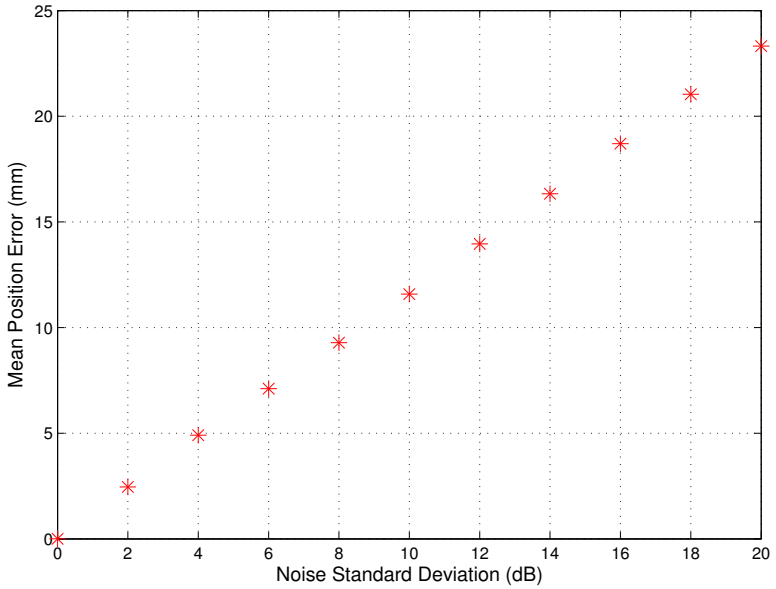

FIGURE 9.8: Mean location error versus noise STD

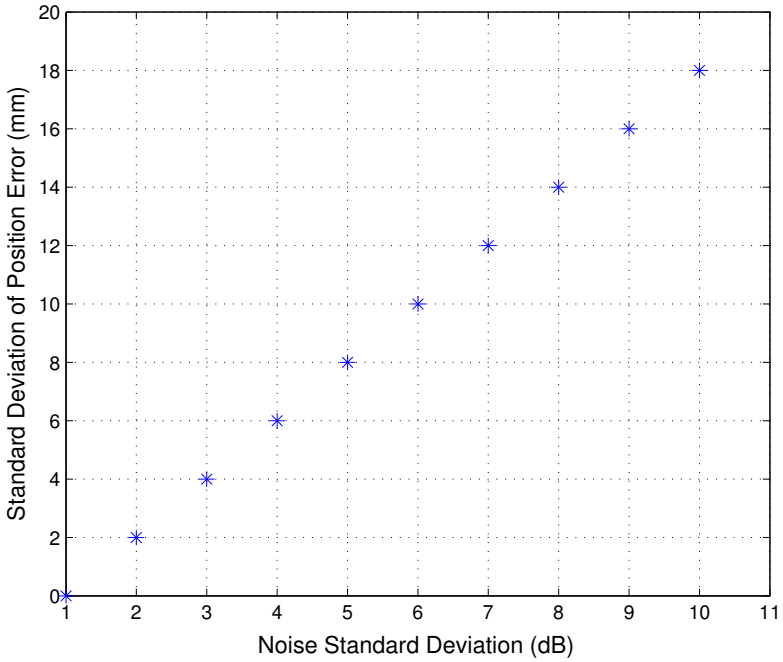

Figure 9.9: Location error STD versus noise STD

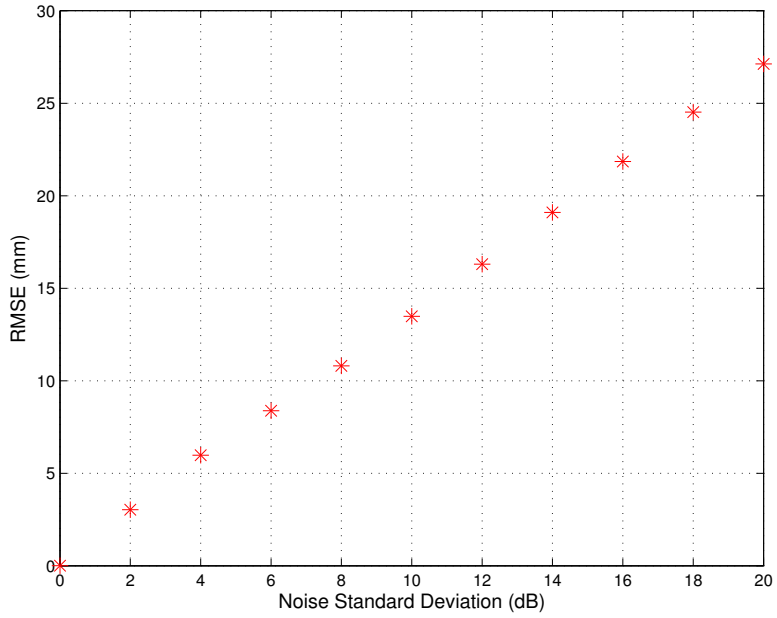

Figure 9.10: RMSE of location error versus noise STD

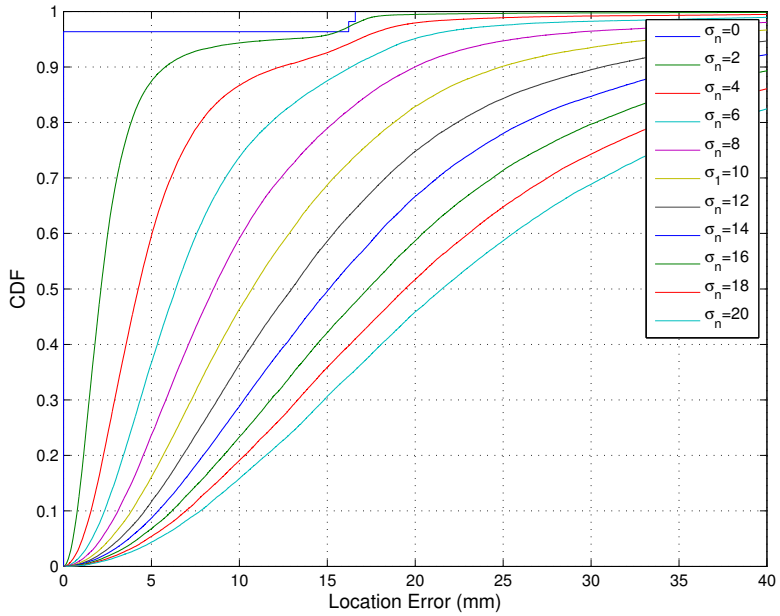

FIGURE 9.11: CDF of location error at different noise STDs

Figure 9.11 shows the Cumulative Distribution Function (CDF) of the location error versus different noise STDs. It can be observed that the distribution of error is higher in higher-noise STDs. Moreover the probability of achieving a location error of less than 15 mm is about 80% in a condition where the noise standard deviation is less than 8 dB .

9.6 CRLB for 2D Capsule Endoscope Localisation

To measure the accuracy of the positioning system a number of accuracy measures can be applied. The Geometric Dilution of Precision (GDOP), CRLB, Root-Mean-Square Error (RMSE) and Cumulative Distribution Probability (CDP) methods are the main positioning accuracy measures that can be used to specify the system performance [145]. Among those techniques, CRLB has been widely used to provide a reference to benchmark the performance of radio positioning. In fact by assessing the CRLB it is possible to outline a lower bound on the performance of any unbiased estimator.

The CRLB is calculated using the Probability Distribution Function (PDF) of the observed data, which includes all the information of the data and assists us to determine the impact of each different parameter on the location estimation accuracy. Therefore

it can be said that the estimation accuracy depends strongly on the PDF. This section presents the derivation of the CRLB for two-dimensional location estimation of a WCE inside the small intestine. For simplicity we consider the 2D localisation problem; the results can easily be extended to the three-dimensional case. We assume three scenarios for the shadowing. In the first scenario we neglect the increase of shadowing variance with distance. In the second scenario we derive the CRLB when the shadowing is distance-dependent and its variance increases linearly with distance. In the last scenario we study the accuracy of the system by considering that the variance of shadowing not only increases linearly with distance but also is spatially correlated. In general, the STD of the measured data (shadowing) is supposed to be constant and not depend on any estimated parameter, but this is not the case in practice, where the STD is parameter dependent. Although this fact can make the CRLB calculation more complicated, it provides a more realistic assessment of system performance. Actually the third scenario is more like what happens in wave propagation inside the human abdomen.

Moreover, in all of the scenarios we assume that a group of sensors at known locations $s_i(r_i, \phi_i), i = 1, 2, .., N$, receive the reflected signal coming from the capsule at an unknown location $c(r, \phi)$.

9.7 CRLB in Constant-Variance Shadowing

In this part we assume that the variance of the shadowing is constant. Using the path-loss model (9.1) and under the assumption of constant variance for shadowing we can write: $S \sim \mathcal{N}(0, \sigma_s^2)$.

We are interested to know the location of the capsule $I_\theta = (r, \phi)$, so the Fisher Information Matrix (FIM) can be defined as

$$I_\theta = \begin{bmatrix} I_{rr} & I_{r\phi} \\ I_{\phi r} & I_{\phi\phi} \end{bmatrix} \tag{9.7}$$

Since the path loss has a Gaussian distribution, according to [146] the elements of the FIM can be calculated using

$$I_\theta(i,j) = [\frac{\partial \mu}{\partial \theta_i}]^T C^{-1} [\frac{\partial \mu}{\partial \theta_j}] + \frac{1}{2} \mathrm{tr}\left[C^{-1} \frac{\partial C}{\partial \theta_i} C^{-1} \frac{\partial C}{\partial \theta_j} \right] \tag{9.8}$$

where μ is the mean path loss

$$\mu = [\mu_1, \mu_2, ..., \mu_n]^T \tag{9.9}$$

$$\mu(i) = a_1 \exp\left(-\frac{(R_i - b_1)^2}{c_1^2}\right) + a_2 \sin\left(b_2(\phi - \phi_i) + c_2\right) \tag{9.10}$$

and the covariance matrix C can be written as

$$C(i) = \text{diag}(\sigma_1^2, \sigma_2^2, ..., \sigma_i^2, ..., \sigma_n^2) \tag{9.11}$$

and the total variance is defined as

$$\sigma^2 = \sigma_s^2 + \sigma_n^2 \tag{9.12}$$

where σ_s^2 and σ_n^2 are the variances of shadowing and measurement noise respectively. In this step, because the variance is constant ($C(\sigma^2) = \sigma^2 I$), then $\frac{\partial C}{\partial \theta} = 0$ and we just need to solve the first part of (9.8).

To calculate each element of I_θ based on (9.8), we first need to calculate the derivative of μ with respect to r and ϕ. That is,

$$\frac{\partial \mu}{\partial r} = [A_1, A_2, ..., A_i, ...A_n]^T, \tag{9.13}$$

$$\frac{\partial \mu}{\partial \phi} = [B_1, B_2, ..., B_i, ...B_n]^T, \tag{9.14}$$

where

$$A_i = \frac{-2a_1(R_i - b_1)(r - r_i\cos(\phi - \phi_i))e^{-(\frac{R_i - b_1}{c_1})^2}}{R_i c_1^2} \tag{9.15}$$

and

$$B_i = \frac{-2a_1 \sin(\phi - \phi_i) r r_i (R_i - b_1) e^{-(\frac{R_i - b_1}{c_1})^2}}{R_i c_1^2} + a_2 b_2 \cos\left(b_2(\phi - \phi_i) + c_2\right) \tag{9.16}$$

By substituting the results in (9.13) through (9.16) in (9.8), each element of the FIM can be obtained as:

$$I_{rr} = [\frac{\partial \mu}{\partial r}]^T C^{-1} [\frac{\partial \mu}{\partial r}] = \sum_{i=1}^{N} \frac{A_i^2}{\sigma^2} \tag{9.17}$$

$$I_{r\phi} = [\frac{\partial \mu}{\partial r}]^T C^{-1} [\frac{\partial \mu}{\partial \phi}] = \sum_{i=1}^{N} \frac{A_i B_i}{\sigma^2} \tag{9.18}$$

$$I_{\phi r} = [\frac{\partial \mu}{\partial \phi}]^T C^{-1} [\frac{\partial \mu}{\partial r}] = \sum_{i=1}^{N} \frac{B_i A_i}{\sigma^2} \tag{9.19}$$

$$I_{\phi\phi} = [\frac{\partial \mu}{\partial \phi}]^T C^{-1} [\frac{\partial \mu}{\partial \phi}] = \sum_{i=1}^{N} \frac{B_i^2}{\sigma^2} \tag{9.20}$$

Since the CRLB matrix is equal to the inverse of the FIM, the CRLB for radial distance r can be calculated as follows:

$$CRLB(r) = \frac{\sigma^2 \sum_{j=1}^{N} B_j^2}{\sum_{i=1}^{N} \sum_{j=1}^{N} (A_i^2 B_j^2 - A_i B_i B_j A_j)} \tag{9.21}$$

and the CRLB for angle ϕ as

$$CRLB(\phi) = \frac{\sigma^2 \sum_{i=1}^{N} A_i^2}{\sum_{i=1}^{N} \sum_{j=1}^{N} (A_i^2 B_j^2 - A_i B_i B_j A_j)} \tag{9.22}$$

It can be seen that the CRLBs in both cases are not only a function of the angle and distance between the capsule and receiver antennas, but also depend on the geometric location information of the capsule and receiver antennas.

We have conducted numerical simulations by assuming that three receiver antennas are available and considering 55 capsule locations inside the small intestine in the first scenario. Figures 9.12 and 9.13 respectively show the distribution of the square root of $CRLB$(r) and the square root of $CRLB(\phi)$ versus each capsule position. It is apparent that the CRLBs vary with respect to each capsule position. The minimum CRLB for r is associated with the capsule locations at which it is near the geometric centre of all three received antennas, while the maximum square root of CRLBs are for capsule locations which are close to the boundary formed by the received antennas. It needs to be mentioned that the trend of the square root of $CRLB$ distribution follows the shape of the sample intestine model. On the other hand the results for $\sqrt{CRLB(\phi)}$ indicate that the accuracy is degraded significantly whenever the angle between the capsule and the received antenna is increased. In this case, the means of $\sqrt{CRLB(r)}$ and $\sqrt{CRLB(\phi)}$ are 14.59 mm and 0.0361 rad respectively. It should be also mentioned that the breakpoints in both Figures 9.12 and 9.13 are due to the change in y-coordinate of the capsule, which is about 0.2 mm.

To evaluate the impact of shadowing on the performance of the system, we calculate

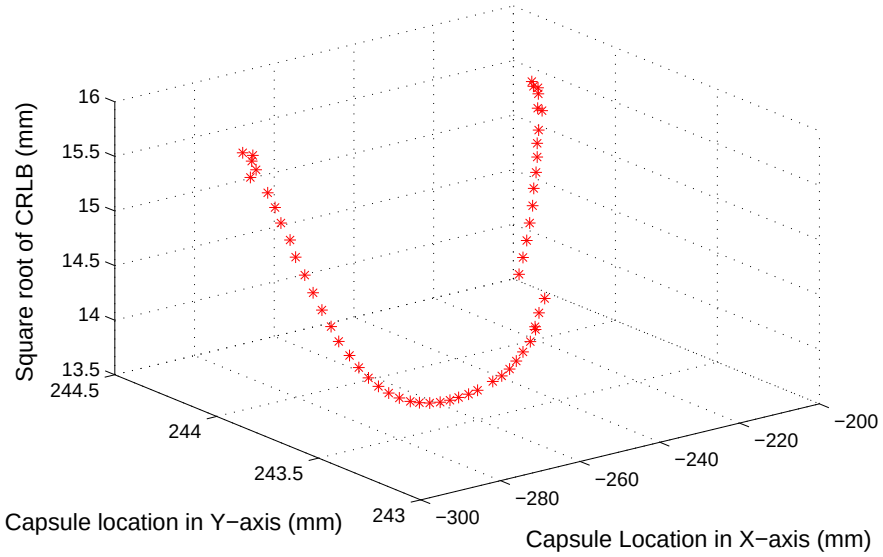

FIGURE 9.12: Distribution of $\sqrt{CRLB(r)}$ versus capsule position at $\sigma_s = 7$ dB

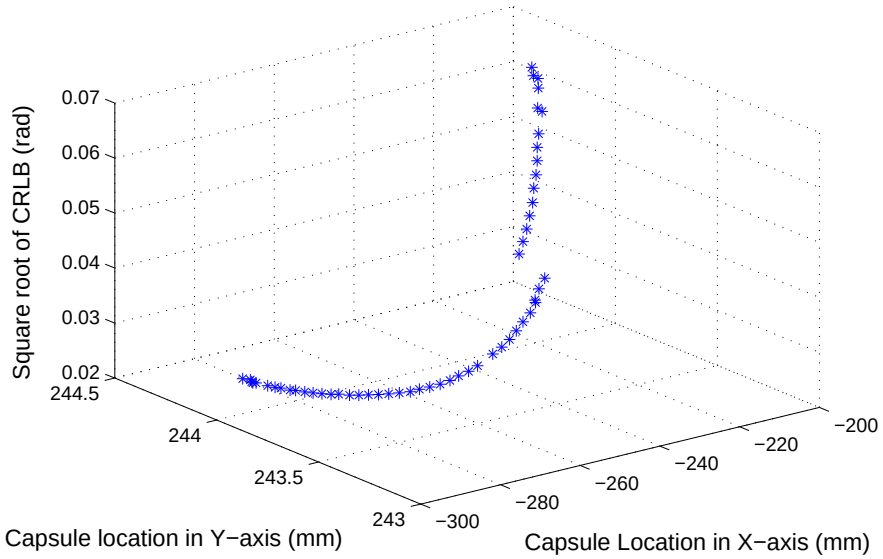

FIGURE 9.13: Distribution of $\sqrt{CRLB(\phi)}$ versus capsule position at $\sigma_s = 7$ dB

the CRLB for radial distance and angle with the STD of shadowing ranging between 0 and 20 dB as shown in Figures 9.14 and 9.15. It can be seen from these figures that $\sqrt{CRLB}$ for both ϕ and r increases as the STD of shadowing becomes larger. Also, in both figures the average $\sqrt{CRLB}$ increases slowly with an shadowing STD of less than

5 dB, while the average $\sqrt{CRLB}$ increases more quickly when the STD of shadowing is greater than 6 dB.

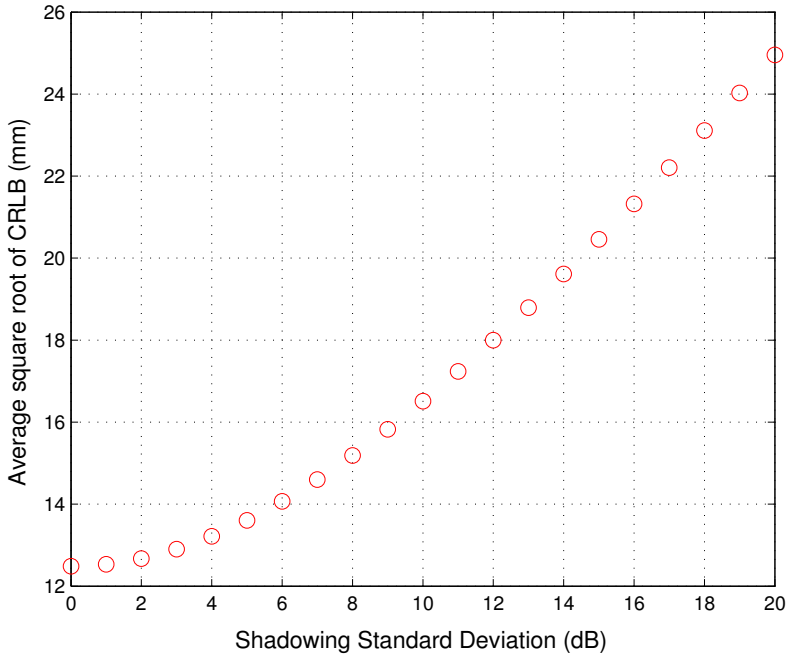

Figure 9.14: Averaged $\sqrt{CRLB(r)}$ versus different shadowing STD

9.8 CRLB in Distance-Dependent Variance Shadowing

In this scenario we assume that the variance of shadowing is not constant as in scenario 1, but depends on distance as $S \sim \mathcal{N}(0, C(R))$. This is mainly because our propagation medium (human abdomen) is not uniform and has random inconsistency, so we can expect more randomness by increasing the distance between the capsule and the on-body sensors [147]. We have also limited our study to the case where the variance of shadowing increases linearly with distance. Moreover we assume that the variance of shadowing is also independent of the measurement noise variance, hence their covariance is zero and we can write the total variance simply as

$$\sigma^2 = \sigma_s^2 + \sigma_n^2 = TR + \sigma_n^2 \tag{9.23}$$

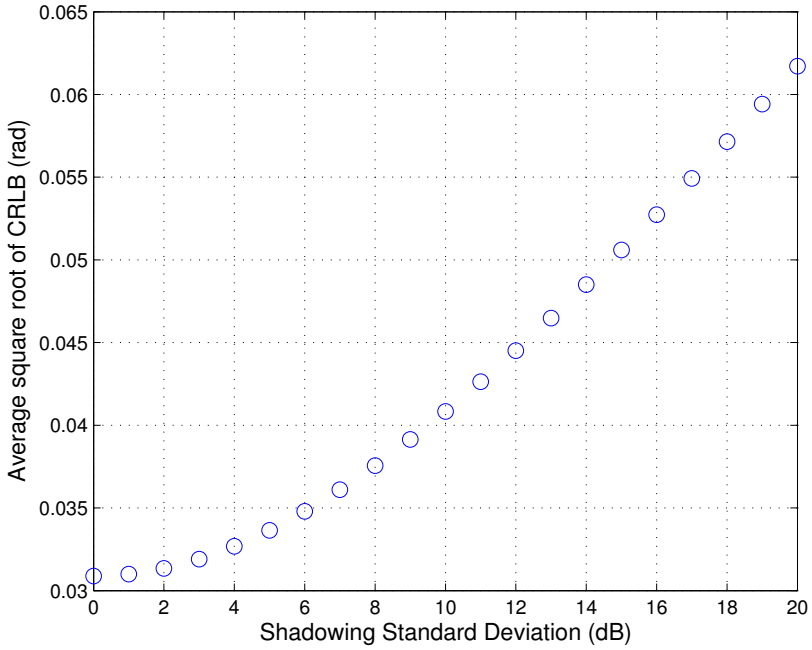

FIGURE 9.15: Averaged $\sqrt{CRLB(\phi)}$ versus different shadowing STD

Here T is a coefficient which represents the dependency of shadowing on distance.

Therefore the problem here is to estimate the capsule location given $PL \sim \mathcal{N}(\mu(\theta), C(\theta))$ where $\mu(\theta)$ is defined by (9.10) and $C(\theta)$ is a diagonal covariance matrix:

$$C(\theta) = \text{diag}(TR_1 + \sigma_n^2, TR_2 + \sigma_n^2, ..., TR_N + \sigma_n^2) \tag{9.24}$$

Just as with scenario 1, since the distribution of path loss is Gaussian, each element of the FIM for $\theta(r, \phi)$ can be calculated using (9.8).

In contrast to the previous scenario, the derivative of the covariance matrix w.r.t. θ is not zero, and it can be calculated as:

$$\frac{\partial C}{\partial r} = \text{diag}(E_1, E_2, ..., E_i) \tag{9.25}$$

and

$$\frac{\partial C}{\partial \phi} = \text{diag}(D_1, D_2, ..., D_i) \tag{9.26}$$

where

$$E_i = \frac{T(r - r_i \cos(\phi - \phi_i))}{R_i} \tag{9.27}$$

and

$$D_i = \frac{Trr_i \sin(\phi - \phi_i)}{R_i} \tag{9.28}$$

By substituting (9.13), (9.14), (9.25) and (9.26) in (9.8), each element of the FIM of $I(\theta)$ can be calculated as:

$$I_{rr} = [\frac{\partial \mu}{\partial r}]^T C^{-1} [\frac{\partial \mu}{\partial r}] + \frac{1}{2}\text{tr}\left[C^{-1}\frac{\partial C}{\partial r}C^{-1}\frac{\partial C}{\partial r}\right] = \sum_{i=1}^{N}\left(\frac{A_i^2}{TR_i + \sigma_n^2} + \frac{E_i^2}{2(TR_i + \sigma_n^2)^2}\right) \tag{9.29}$$

$$I_{r\phi} = [\frac{\partial \mu}{\partial r}]^T C^{-1} [\frac{\partial \mu}{\partial \phi}] + \frac{1}{2}\text{tr}\left[C^{-1}\frac{\partial C}{\partial r}C^{-1}\frac{\partial C}{\partial \phi}\right] = \sum_{i=1}^{N}\left(\frac{A_i B_i}{TR_i + \sigma_n^2} + \frac{E_i D_i}{2(TR_i + \sigma_n^2)^2}\right) \tag{9.30}$$

$$I_{\phi r} = [\frac{\partial \mu}{\partial \phi}]^T C^{-1} [\frac{\partial \mu}{\partial r}] + \frac{1}{2}\text{tr}\left[C^{-1}\frac{\partial C}{\partial \phi}C^{-1}\frac{\partial C}{\partial r}\right] = \sum_{i=1}^{N}\left(\frac{B_i A_i}{TR_i + \sigma_n^2} + \frac{D_i E_i}{2(TR_i + \sigma_n^2)^2}\right) \tag{9.31}$$

$$I_{\phi\phi} = [\frac{\partial \mu}{\partial \phi}]^T C^{-1} [\frac{\partial \mu}{\partial \phi}] + \frac{1}{2}\text{tr}\left[C^{-1}\frac{\partial C}{\partial \phi}C^{-1}\frac{\partial C}{\partial \phi}\right] = \sum_{i=1}^{N}\left(\frac{B_i^2}{TR_i + \sigma_n^2} + \frac{D_i^2}{2(TR_i + \sigma_n^2)^2}\right) \tag{9.32}$$

Hence $I(\theta)$ is given by

$$I(\theta) = \begin{bmatrix} I_{rr} & I_{r\phi} \\ I_{\phi r} & I_{\phi\phi} \end{bmatrix} \tag{9.33}$$

Therefore the CRLB for a radial distance of r and an azimuth angle of ϕ can be

derived as:

$$CRLB(r) = \frac{2\sum_{i=1}^{N} \frac{(2B_i^2(TR_i+\sigma_n^2)+D_i^2)}{(TR_i+\sigma_n^2)^2}}{\sum_{i=1}^{N}\sum_{j=1}^{N} \frac{K_{ij}}{(TR_i+\sigma_n^2)^2(TR_j+\sigma_n^2)^2}} \tag{9.34}$$

$$CRLB(\phi) = \frac{2\sum_{i=1}^{N} \frac{(2A_i^2(TR_i+\sigma_n^2)+E_i^2)}{(TR_i+\sigma_n^2)^2}}{\sum_{i=1}^{N}\sum_{j=1}^{N} \frac{K_{ij}}{(TR_i+\sigma_n^2)^2(TR_j+\sigma_n^2)^2}} \tag{9.35}$$

where K is

$$\begin{aligned} K_{ij} = {} & (2A_i^2(TR_i+\sigma_n^2)+E_i^2)(2B_j^2(TR_j+\sigma_n^2)+D_j^2) \\ & -(2(TR_i+\sigma_n^2)A_iB_i+E_iD_i)(2(TR_j+\sigma_n^2)B_jA_j+D_jE_j) \end{aligned} \tag{9.36}$$

In this scenario we can again see from (9.34) and (9.35) that the CRLBs depend on the radial distance and the angle between the capsule and the receiver antenna.

We have conducted numerical simulations by employing three receiver antennas to investigate the impact of distance-dependent shadowing on the derived CRLBs. Figures 9.16 and 9.17 show the average square root of $CRLB$ with respect to different shadowing coefficients. It can be seen that the average $\sqrt{CRLB}$ for both r and ϕ increases with shadowing STD. In fact the relation between the square root of $CRLB$ and different shadowing coefficients is approximately linear. Furthermore, it can be observed that, in the worst case (shadowing coefficient equal to one), the system can still achieve a quite acceptable square root of $CRLB$ of 14.83 mm and 0.036 rad for r and ϕ respectively.

9.9 CRLB in Specially Correlated and Distance-Dependent Variance Shadowing

In the third scenario, we assume that the variance of shadowing is spatially correlated and also dependent on distance. In most cases the shadowing is modelled as independent and identically distributed (i.i.d.) zero-mean Gaussian random variables (the same as in scenario 1). However, in reality, the correlation of the shadow fading is perceptible due to the existence of obstacles in the propagation paths between the source and anchor nodes, or the network configuration [148, 149]. In fact shadowing correlation occurs when two links share some dominant propagation path. In general, different

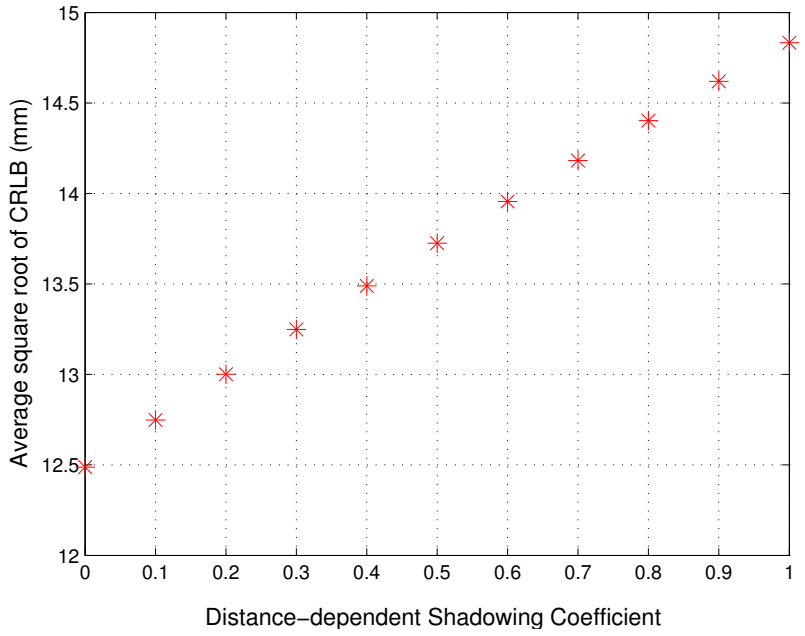

FIGURE 9.16: Averaged $\sqrt{CRLB(r)}$ versus different shadowing coefficients

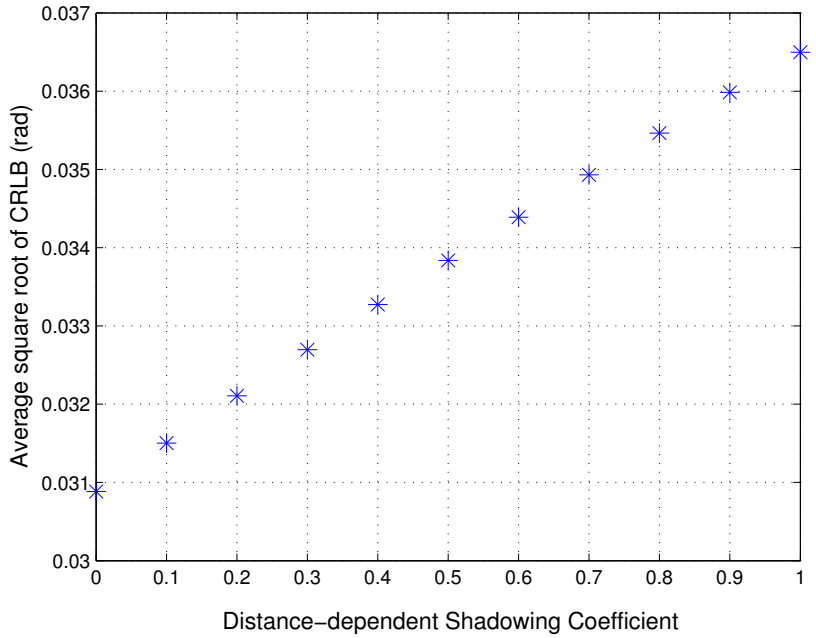

FIGURE 9.17: Averaged $\sqrt{CRLB(\phi)}$ versus different shadowing coefficients

models of shadowing correlation which have been developed in the literature can be

classified into four main groups: distance only, angle only, distance-angle, distance-angle-separable [150, 151]. So far three statistical models for shadowing correlation have been proposed to discover the performance of a network. These models can be summarised as:

- Gudmundson model (1991): This is a widely accepted model to predict the shadowing correlation between the mobile node and the base station in a cellular network [152].
- Wang et al. model (2006): It is an extension of the Gudmundson model and describes the shadow correlation on just a single link, when both ends of the link are moving [153].
- Agrawal and Patwari model (2009): This model represents the correlations in shadow fading between different links in a multi-hop network [154].

Of the three aforementioned models, the Gudmundson model is the most suitable for the capsule endoscope scenario. In fact the model makes the assumption that the distance between the mobile node and the base station should be large enough compared to the distance of the mobile node relocation. Since the movement of the capsule inside the small intestine is very slow, the distance of the capsule from the on-body sensors is larger than the distance of capsule relocation over a sampling interval.

According to the Gudmundson model the covariance matrix for shadowing can be written as

$$\Gamma_{ij} = \begin{cases} \sigma_s^2, & i = j \\ \sigma_s^2 e^{|\frac{d_{ij}}{D}|}, & i \neq j \end{cases} \tag{9.37}$$

where σ_s^2 is the variance of the shadowing, d_{ij} is the Euclidean distance between two sensors at location points i and j. D is the de-correlation distance and is defined as the distance separation at which the correlation coefficient reduces to 1/2 [155]. In free space D is around 50-100 m, however in our case, because we are considering in-body to on-body communication, the value of D is much less due to the very small propagation distance. It is also apparent that in this situation the covariance matrix is no longer diagonal.

To calculate the CRLB for our last scenario, we again need to apply (9.8) to derive each element of the FIM for the vector R. According to our assumption the shadowing is spatially correlated and also distance dependent ($S \sim \mathcal{N}(0, C(r, \phi))$). Therefore the path-loss distribution can be written as: $Pl \sim \mathcal{N}(\mu(r, \phi), C(r, \phi))$, where $C(r, \phi)$ is the

covariance matrix of shadowing autocorrelation. When considering N links between the sensor nodes and each capsule location, it can be written as

$$C(r,\phi) = \begin{bmatrix} \sigma_s^2 + \sigma_n^2 & \cdots & \sigma_s^2 e^{-\frac{d_{1N}}{D}} + \sigma_n^2 \\ \sigma_s^2 e^{-\frac{d_{21}}{D}} + \sigma_n^2 & \cdots & \sigma_s^2 e^{-\frac{d_{2N}}{D}} + \sigma_n^2 \\ \vdots & \ddots & \vdots \\ \sigma_s^2 e^{-\frac{d_{N1}}{D}} + \sigma_n^2 & \cdots & \sigma_s^2 + \sigma_n^2 \end{bmatrix} \tag{9.38}$$

Since in this scenario the covariance matrix is not diagonal, determination of I_R in closed form is complex. Hence for simplicity we have decided to solve the problem by just considering two links between a single capsule location and two external sensor nodes. We are interested to identify the autocorrelation effect between these two links (see Figure 9.18).

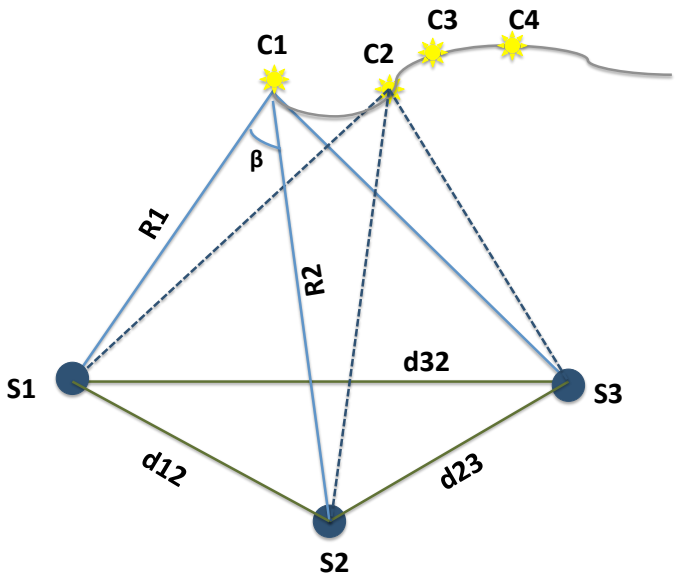

Figure 9.18: Geometric relation between capsule location and two on-body sensors

Therefore the covariance matrix for this case can be formed as

$$\Gamma(R) = \begin{bmatrix} \sigma_s^2 + \sigma_n^2 & \sigma_s^2 e^{-\frac{d_{12}}{D}} + \sigma_n^2 \\ \sigma_s^2 e^{-\frac{d_{21}}{D}} + \sigma_n^2 & \sigma_s^2 + \sigma_n^2 \end{bmatrix} \tag{9.39}$$

where

$$d_{ij} = d_{ji} = \sqrt{R_i^2 + R_j^2 - 2R_iR_j\cos\beta} \tag{9.40}$$

Here d_{12} is equal to d_{21} which represents the Euclidean distance between the two sensors. R_1 and R_2 are the distances of the capsule from the two sensors (s_i and s_j) and β is the angle between them (Figure 9.18). We still apply (9.8) to calculate the CRLB and find each element of the FIM of $I(\theta)$, under the same assumption that the path loss has a Gaussian trend. It should be noted that from now on alphabetical notations will be used in each equation to simplify the equations for further mathematical determination.

Let us calculate the first derivative of the covariance matrix of Γ w.r.t. r and ϕ; we write

$$\frac{\partial C_{ij}}{\partial r} = \begin{bmatrix} 0 & M \\ M & 0 \end{bmatrix} \tag{9.41}$$

$$\frac{\partial C_{ij}}{\partial \phi} = \begin{bmatrix} 0 & L \\ L & 0 \end{bmatrix} \tag{9.42}$$

where

$$M_i = -\frac{\sigma_s^2(r - r_i\cos(\phi - \phi_i))(R_i - R_j\cos\beta)e^{-\frac{d12}{D}}}{DR_id_{12}} \tag{9.43}$$

$$L_i = -\frac{\sigma_s^2 r r_i\sin(\phi - \phi_i)(R_i - R_j\cos\beta)e^{-\frac{d12}{D}}}{DR_id_{12}} \tag{9.44}$$

and i and j represent sensor location indices:

$$i = \begin{cases} 1, & \text{if } j = 2 \\ 2, & \text{if } j = 1 \end{cases} \tag{9.45}$$

Also the inverse of the covariance matrix can be written as:

$$C^{-1} = \begin{bmatrix} F & H \\ H & F \end{bmatrix} \tag{9.46}$$

where

$$F = \frac{\sigma_s^2 + \sigma_n^2}{\sigma_s^4(1 - e^{\frac{-2d_{12}}{D}}) + 2\sigma_s^2\sigma_n^2(1 - e^{\frac{-d_{12}}{D}})} \tag{9.47}$$

$$H = \frac{\sigma_s^2 e^{-\frac{d_{12}}{D}} + \sigma_n^2}{\sigma_s^4(1 - e^{\frac{-2d_{12}}{D}}) + 2\sigma_s^2\sigma_n^2(1 - e^{\frac{-d_{12}}{D}})} \tag{9.48}$$

The path-loss mean $\mu(i)$ is the same as (9.10), hence the first derivative of the path loss mean with respect to r and ϕ can be written as:

$$\frac{\partial \mu}{\partial r} = [A_1, A_2]^T \tag{9.49}$$

$$\frac{\partial \mu}{\partial \phi} = [B_1, B2]^T \tag{9.50}$$

where A and B are defined as:

$$A_i = \frac{-2a_1(R_i - b_1)(r - r_i\cos(\phi - \phi_i))e^{-(\frac{R_i - b_1}{c_1})^2}}{R_i c_1^2} \tag{9.51}$$

$$B_i = \frac{-2a_1\sin(\phi - \phi_i) r r_i (R_i - b_1)e^{-(\frac{R_i - b_1}{c_1})^2}}{R_i c_1^2} + a_2 b_2 \cos(b_2(\phi - \phi_i) + c_2) \tag{9.52}$$

By substituting the above equations in (9.8) each element of the FIM can be obtained as:

$$I_{rr} = [\frac{\partial \mu}{\partial r}]^T C^{-1}[\frac{\partial \mu}{\partial r}] + \frac{1}{2}\mathrm{tr}\left[C^{-1}\frac{\partial C}{\partial r}C^{-1}\frac{\partial C}{\partial r}\right] = \sum_{i=1}^{2}(A_i^2 H + M_i^2(H^2 + F^2)) \tag{9.53}$$

$$I_{r\phi} = [\frac{\partial \mu}{\partial r}]^T C^{-1}[\frac{\partial \mu}{\partial \phi}] + \frac{1}{2}\mathrm{tr}\left[C^{-1}\frac{\partial C}{\partial r}C^{-1}\frac{\partial C}{\partial \phi}\right] = \sum_{i=1}^{2}(A_i B_i H + M_i L_i(H^2 + F^2)) \tag{9.54}$$

$$I_{\phi r} = [\frac{\partial \mu}{\partial \phi}]^T C^{-1} [\frac{\partial \mu}{\partial r}] + \frac{1}{2}\text{tr}\left[C^{-1}\frac{\partial C}{\partial \phi}C^{-1}\frac{\partial C}{\partial r}\right] = \sum_{i=1}^{2}(B_i A_i H + M_i L_i (H^2 + F^2)) \tag{9.55}$$

$$I_{\phi\phi} = [\frac{\partial \mu}{\partial \phi}]^T C^{-1} [\frac{\partial \mu}{\partial \phi}] + \frac{1}{2}\text{tr}\left[C^{-1}\frac{\partial C}{\partial \phi}C^{-1}\frac{\partial C}{\partial \phi}\right] = \sum_{i=1}^{2}(B_i^2 H + L_i^2 (H^2 + F^2)) \tag{9.56}$$

The CRLB for radial distance r and angle ϕ can be obtained by taking the inverse of $I(\theta)$ as:

$$CRLB(r) = \frac{\sum_{i=1}^{2}(B_i^2 H + L_i^2 (H^2 + F^2))}{\sum_{i=1}^{2}\sum_{j=1}^{2} K_{ij}} \tag{9.57}$$

and

$$CRLB(\phi) = \frac{\sum_{i=1}^{2}(A_i^2 H + M_i^2 (H^2 + F^2))}{\sum_{i=1}^{2}\sum_{j=1}^{2} K_{ij}} \tag{9.58}$$

where

$$K_{ij} = \big((A_i^2 H + M_i^2 (H^2 + F^2))(B_j^2 H + L_j^2 (H^2 + F^2))\big) - \big((A_i B_i H + M_i L_i (H^2 + F^2))(B_j A_j H + M_j L_j (H^2 + F^2))\big) \tag{9.59}$$

We have conducted numerical simulations to derive the CRLB for the third scenario by considering only two links and assuming a decorrelation distance of $D = 200$ mm. This assumption is intuitive, since the maximum depth of our human phantom model is not greater than 20 cm. d_{12}, which is the distance between two receiver antennas, is 93 mm (Figure 9.19).

Figures 9.20 and 9.21 illustrate the distribution of $\sqrt{CRLB}$ with respect to the distance moved by a capsule. Before any discussion on the obtained results, it is appropriate to briefly review the capsule movement inside the small intestine. The movement of a wireless capsule endoscope along the small intestine is in a similar manner to food movement, and it depends strongly on the natural peristalsis of the GI tract. Therefore it can be concluded that the movement behaviour of the capsule is totally determined

by the strain and stress cycle of the intestine. Clinical examinations of capsule endoscopes show that the assumption of a constant strain cycle of the intestine is true if the patient is in their normal condition [156]. On the other hand, it is expected that the capsule stays for a random amount of time in each bend section of the intestine. In general it is presumed that the capsule endoscope has a small variation in speed while it is moving inside a certain section of the small intestine. In this study we assume that the capsule movement is about 4 mm over each sampling interval. According to the author's knowledge the exact amount of capsule movement at each second inside the small intestine has not been addressed in any study. As Figure 9.20 shows, the system performance will be improved when the capsule is moving forward further from its previous position. In fact the capsule encounters the same category of environment when it is located sufficiently close to its previous position so that the measurements are heavily correlated. The auto-correlation shadowing affects the total path loss, so the capsule experiences different losses in time as it moves. It can clearly be seen that when the capsule is further from its first position ($d = 80$ mm) then $\sqrt{CRLB}$ reaches its minimum value. After this point the capsule enters into the uncorrelated region where the shadowing effects are considered totally uncorrelated and the performance of the system is degraded. On the other hand, Figure 9.21 shows that increasing the relocation distance of the capsule causes a decreasing trend in $\sqrt{CRLB}$ for ϕ. It can also be seen that at $d = 120$ mm, where the capsule is about half of its actual length away from its first location, $\sqrt{CRLB}$ experiences its minimum value. Similarly to $\sqrt{CRLB}$ for r the performance of the system gets worse exponentially when the capsule enters the uncorrelated shadowing region.

We have also calculated $\sqrt{CRLB}$ for r and ϕ for the case when all three receiver antennas are in the system. Figures 9.22 and 9.23 show the distribution of the square root of $CRLB$ versus different capsule locations with respect to the three receiver antennas. As can be seen, $\sqrt{CRLB}$ for r reaches its minimum value (1.3 mm) when the capsule is at a distance of about half of its actual length from its first position. After that point the capsule enters the uncorrelated shadowing region and $\sqrt{CRLB}$ increases exponentially. On the other hand in the presence of three receiver antennas we can see that the correlated shadowing has no significant impact on $\sqrt{CRLB}$ for ϕ, however after the capsule reaches the uncorrelated shadowing region $\sqrt{CRLB}$ increases exponentially. It should also be mentioned that the performance of the system is much better when we employ three receiver antennas. Overall the results demonstrate that a

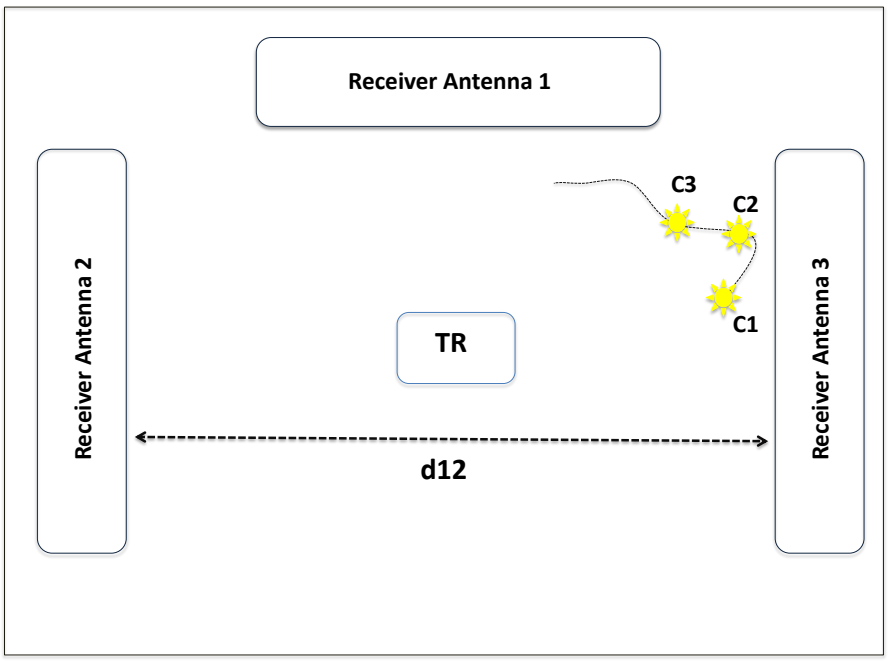

FIGURE 9.19: Illustration of antenna configuration and capsule relocation

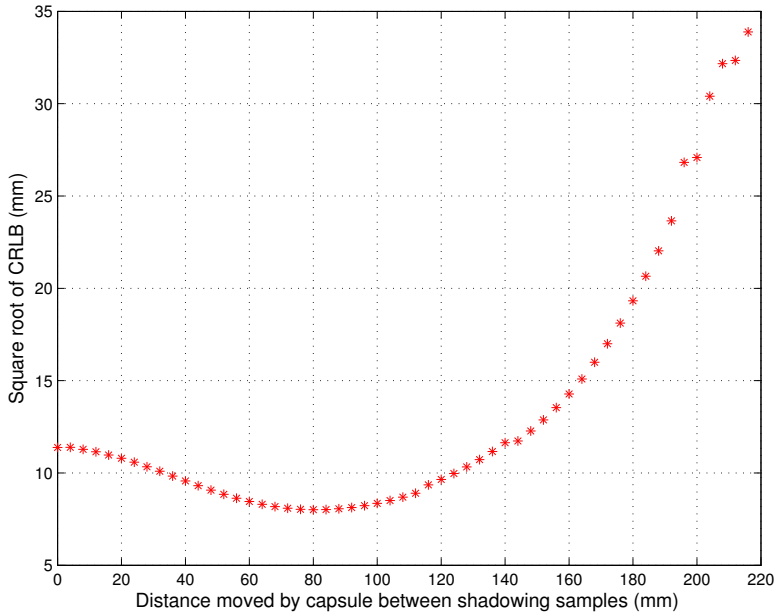

FIGURE 9.20: Distribution of $\sqrt{CRLB(r)}$ versus different capsule displacements with two receiver antennas

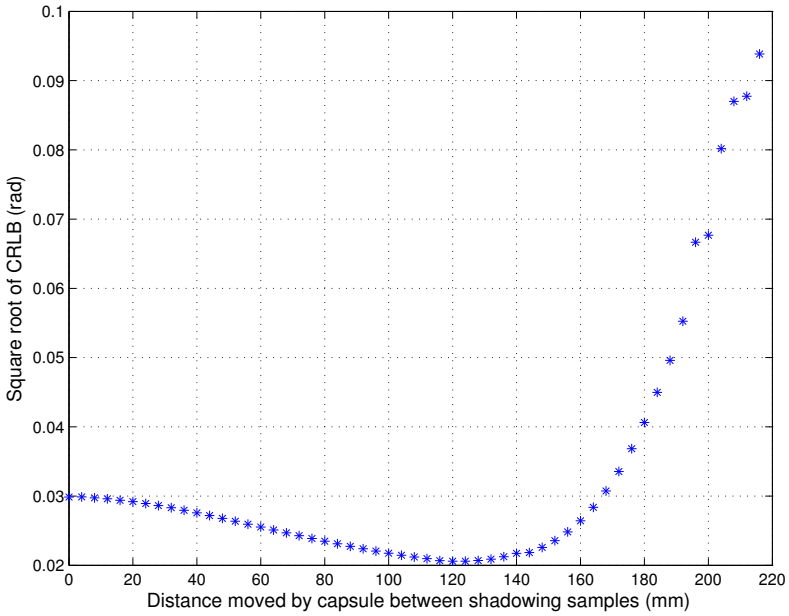

Figure 9.21: Distribution of $\sqrt{CRLB(\phi)}$ versus different capsule displacements with two receiver antennas

significant performance gain can be obtained in the location estimation of the wireless capsule in correlated shadowing when the capsule is located at an appropriate distance from its previous position.

9.10 Chapter Summary

In this chapter the achievable location estimation error for RSS-based localisation methods was studied as a wireless capsule endoscope passes through the small intestine. In this study the trilateration method was employed to estimate the 2D location of the capsule endoscope. In particular, the Levenberg-Marquardt algorithm, which is a Non-linear Least Squares (NLLS) algorithm, was exploited to obtain the capsule position estimate. The results reveal that we can achieve a mean radial position error of 3 cm for capsule location estimation. Overall the obtained results assure us that, with 90% probability, the location estimation error is less than 4 cm. We have also studied the impact of different noise standard deviations on location error and our results confirm that the probability of achieving a location error of less than 15 mm is about 80% in a condition where the noise standard deviation is less than 8 dB .

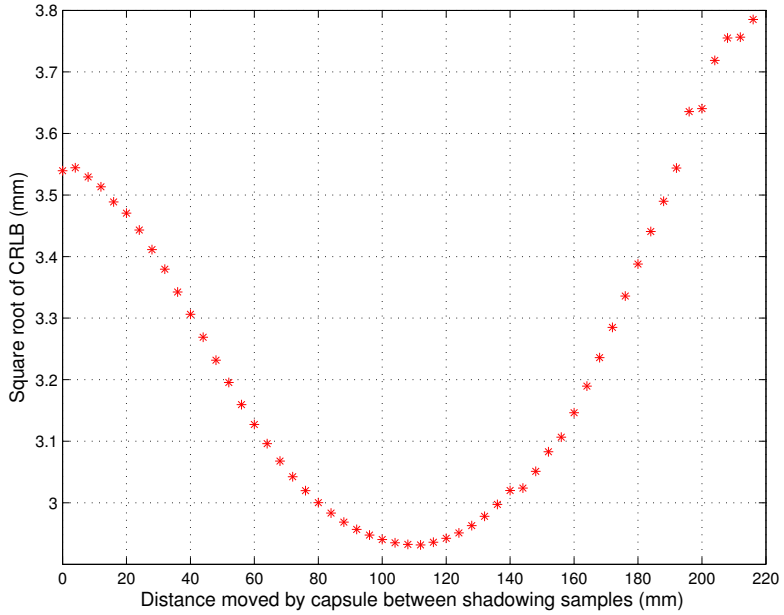

FIGURE 9.22: Distribution of $\sqrt{CRLB(r)}$ versus different capsule displacements with three receiver antennas

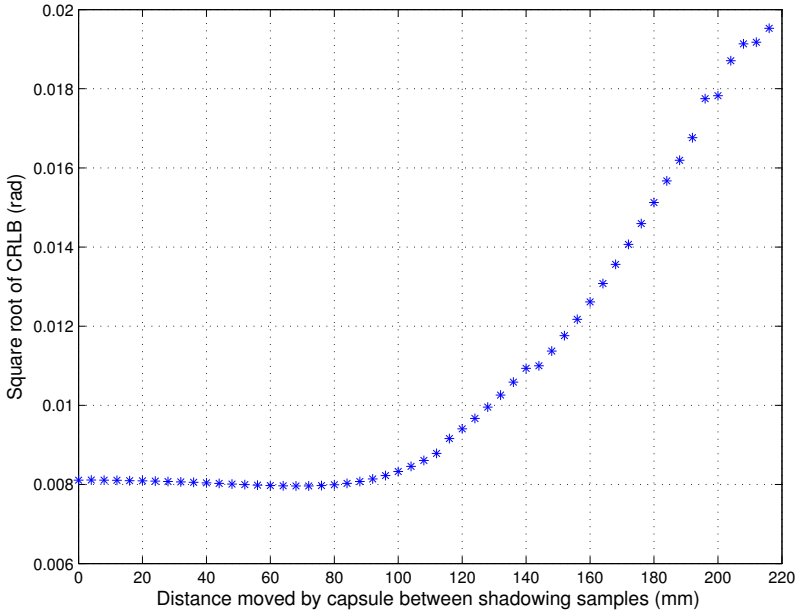

FIGURE 9.23: Distribution of $\sqrt{CRLB(\phi)}$ versus different capsule displacements with three receiver antennas

In the second part, the potential precision limits for RSS-based localisation for a wireless capsule endoscope was investigated using the CRLB method. The theoretical localisation precision limit was studied for three different shadowing scenarios. The results show that the CRLB behaves quite differently for each of the scenarios. Moreover our results demonstrate that in all the three aforementioned scenarios the localisation precision depends on the distance between the capsule and the receiver antennas as well as the angle between them. In scenario 1, where the shadowing is constant, we achieved means of 14.59 mm and 0.0361 rad for $\sqrt{CRLB(r)}$ and $\sqrt{CRLB(\phi)}$ respectively. In scenario 2, where the shadowing is distance dependent, even for the high shadowing coefficient of one we can still achieve an acceptable square root of $CRLB$ of 14.83 mm and 0.036 rad for r and ϕ respectively. The results also indicate that, in the most realistic scenario where the shadowing is spatially correlated and distance dependent, and the standard deviation of noise is 7 dB, the maximum square root of $CRLB$ is 3.8 mm. Moreover, $\sqrt{CRLB}$ experiences its minimum value of 2 mm when the capsule is away from its first location by about half of its actual length, hence we can expect the best system performance at this point. Moreover in comparing the system performance in terms of achieved precision the results demonstrate that the system with three receiver antennas has much better performance than the system with two receiver antennas. From the results and not withstanding the transmitter or receiver circuitry complexity, positioning and number of antennas, etc., we conclude that a 2.4 GHz RSS-based localisation using a radar system is feasible and can reach a precision in the order of centimetre.

Publication pertaining to this chapter:

- P. Ara, K. Yu, S. Cheng, E. Dutkiewicz, and M. Heimlich, "Derivation of CRLB for Wireless Capsule Endoscope Localization Using Received Signal Strength," *in IEEE Sensors Journal*, 2016, vol.PP, no.99, pp.1-11.

10

Conclusion and Recommendations for Future Work

10.1 Conclusion

Location estimation of a capsule endoscope in the gastrointestinal (GI) tract is a challenging task, as radio-frequency signals encounter a high-loss channel propagation environment. In this thesis, location estimation of a wireless capsule endoscope inside the small intestine has been presented using the Received Signal Strength (RSS) method and applying a radar system. The proposed design has been simulated using the 3D electromagnetic simulation software of SEMCAD X and the numerical computing environment of MATLAB.

Of different proposed working frequencies for the radar system, the results confirmed that the radar system can have a better performance at the front of the human abdomen at 2.4 GHz. Accordingly a half-wavelength dipole antenna was designed at 2.4 GHz to be applied as a transceiver antenna in front of the human body.

To improve the accuracy of RF-based localisation techniques in the GI tract, the primary focus should be on the investigation of radio propagation inside the human body, specifically in the human abdomen area, to evaluate the impact of each tissue

layer on the propagation. Therefore, it is necessary to have an accurate propagation-based channel model before any specific localisation techniques can be investigated. A deterministic path-loss model was developed based on the absorption loss by each tissue layer and the reflection loss by each layer boundary, and it showed that a deterministic path-loss model, which is only dependent on a theoretical analysis of radio-wave propagation inside the abdomen, cannot fully achieve the desired accuracy of the model for each capsule location inside the abdomen. Hence a new statistical path-loss model was developed which was based on several simulations on three different human phantom models. This path-loss model was applied for the rest of our studies, since it showed an acceptable approximation to model in-body propagation.

To study the achievable location estimation error for our proposed radar system, the trilateration method was employed to estimate the location of the capsule in two dimensions, as well as the Non-linear Least Squares (NLLS) algorithm to compute the capsule position. The obtained results assure us that the probability of achieving a location error of less than 15 mm is about 80% in a condition where the noise standard deviation is less than 8 dB. Finally, in analysing the potential precision limit for RSS-based localisation, the results confirm that in the most realistic scenario, where the shadowing is spatially correlated and distance dependent, the square root of $CRLB$ experiences its minimum value when the capsule is away from its first location by about half of its actual length, hence we can expect the best system performance at this point. Overall, from the results and not withstanding the transmitter or receiver circuitry complexity, positioning and number of antennas, etc., it can be concluded that a 2.4 GHz RSS-based localisation using a radar system is feasible and can reach a precision in the order of centimetre.

10.2 Contribution

Contributions are made in different fields in this thesis, however the main contributions are:

(i) Developing a theoretical in-body path-loss model focused on the abdomen region and based on the different dielectric properties of human tissues and several wave absorptions and reflections by each tissue and each tissue boundary. We confirm that the theoretical path-loss model might not be suitable for some applications such as developing a precise location estimation algorithm. This issue is even more crucial at higher frequency, where a smaller antenna size is used and the object lies closer to the near-field region.

(ii) Proposing a statistical path-loss model for three different anatomical human models. The proposed path-loss model is a good approximation to model in-body RF propagation, since real measurements are quite infeasible for a capsule endoscopy subject. In general for any given body (male, female, child) it is not possible to simply use the propagation loss (S_{21}) to determine distance. This is mainly because the types of tissue when going from the antenna to a point in the intestine near the lung are different from the same distance toward the bowels.

(iii) Investigating the achievable location estimation error for the RSS-based localisation method as the capsule endoscope passes through the small intestine. The results reveal that we can achieve a mean radial position error of 3 cm for capsule location estimation. Overall the obtained results assure us that with 90% probability the location estimation error is less than 4 cm. We have also studied the impact of different noise standard deviations on location error, and our results confirmed that the probability of achieving a location error of less than 15 mm is about 80% in a condition where the noise standard deviation is less than 8 dB .

(iv) The potential precision limits for RSS-based localisation for the wireless capsule endoscope was investigated using the Cramér-Rao Lower Bound (CRLB) method. The theoretical localisation precision limit was studied under three different shadowing scenarios. The results show that in the most realistic scenario, when the shadowing is spatially correlated and distance dependent and the standard deviation of noise is 7 dB, the maximum square root of $CRLB$ is 3.8 mm. Moreover the square root of $CRLB$ experiences its minimum value of 2 mm when the capsule is away from its first location by about half of the capsule length.

10.3 Limitations and Future Research Directions

This research has laid significant groundwork for further investigation in developing a location estimation algorithm to estimate the location of a capsule endoscope inside the GI tract using the Received Signal Strength (RSS) method. However, identified limitations may be investigated to identify opportunities for further research. The limitations and difficulties can be listed as follows:

(i) In the past few years, several different in-body path-loss models for the abdomen region were developed based on theoretical or simulation studies. This is mainly

because it is impractical to perform measurements on a real human body. However none of these path-loss models can perfectly address and model the complexity of human tissues, specifically in the abdomen region.

(ii) Simulation-based studies for capsule location estimation should be performed for different human phantom models which vary in height, age, weight, etc. This assists us to develop a unique model and algorithm for WCE location estimation.

(iii) The resolution of the small intestine in the phantom models should be considerably improved to enable researchers to simulate a realistic situation.

(iv) Although setting a higher resolution by increasing the voxel size for the phantom models provides a closer match to the real human body, the simulation time will be increased tremendously. Moreover, powerful computers are needed to handle such complex and time-consuming simulations.

Along with the aforementioned limitations that need to be addressed in future work, the following suggestions for further work might also be considered to achieve highly accurate location estimation.

A further contribution can be made by applying the TOA location estimation technique to measure the time of flight between the capsule and each received antenna. It is a good idea to compare the performance of the two most in-demand localisation techniques (RSS and TOA) to find the best possible performance of the radar system in any of the aforementioned techniques. Moreover other location estimation algorithms, such as Hybrid localisation algorithms, the K-nearest-neighbour (KNN) algorithm or the fingerprint-based algorithm, can be applied to find the best algorithm performance.

Another recommended future line of research is modelling the movement of a wireless capsule endoscope and developing a model-based target tracking algorithm to improve the location estimation of the capsule.

A

Human Phantom Models

Recently, due to the development of wireless communication devices that need to be used inside or in the close vicinity of the human body, human phantom models are known as an essential tool to study interaction of electromagnetic fields and human tissues as well as the safety of such devices. A body phantom model is a physical phantom or simulated biological body which represents different characteristics of biological tissues. In general, applying phantom models can assists researchers to analyse the influence of an electromagnetic field on different human tissues as well as the impact of the human body on their designed devices, because these studies are not applicable on real human subjects.

A.1 Physical Phantom Model

Normally a physical phantom model can be classified as liquid, solid or semisolid models and will be discussed briefly in the following sections.

A.1.1 Liquid Phantom Model

A liquid phantom is the first and oldest type of phantom. It is made of a container that is filled with a liquid. The liquid has the same dielectric properties of the desired tissues at the selected frequency. Most liquid phantoms use sugar or Di-ethylene Glycol Butyl Ether (DGBE) to control the permittivity and salt (NaCl) to control the conductivity of the liquid [157]. The container is usually made of a fibreglass material, which has a low relative permittivity and conductivity. The shape of the container can be designed according to the application requirements. These phantoms are widely used in SAR studies. In general this phantom suffers from some disadvantages, as the difficulty of dealing with the dielectric properties and shape of the container and also the dielectric properties of the liquid are limited to certain frequencies [158].

A.1.2 Semisolid Phantom Model

The authors in [157] developed a semisolid phantom, by mixing some components such as: sodium chloride, polyamide resin (TX-150), Polyethylene powder and water. The polyethylene powder and sodium chloride were used to control the relative conductivity and permittivity of the phantom. Furthermore, Ito et al. [159] developed a self-shaping phantom based on the recipe in [157]. However this time they added two more substances, sodium dehydroacetate and agar, to preserve and coagulate the phantom. This kind of phantom is normally suitable to be applied for high-water-content materials such as muscle or brain. On the other hand, by adding polyacrylamide to the above recipe it is possible to apply the phantom for low-water-content material as well. The main disadvantage of semisolid phantoms is that they can easily degrad over time at room temperature due to the loss of water or growth of fungi, so they should be kept in a cold place such as a refrigerator.

A.1.3 Solid Phantom Model

A solid phantom is a kind of phantom that is made of materials which can keep their shape for a period of time. This type of phantom is also suitable for in-body or out-body studies since it can accurately represent the inhomogeneity of the human body. Several recipes for this kind of phantom have been proposed, such as a mixture of silicone rubber with carbon fibre [160], mixture of ceramic and graphic [161], and plastic made conductive with carbon black [162]. Most of these phantoms are easy to build except for ceramic phantoms, that need expensive equipment and special construction

procedures.

A.2 Numerical Phantom Model

A numerical phantom is a type of phantom model which is specifically designed for computational simulation-based study or theoretical analysis. They can be divided into two subgroups, theoretical phantom and voxel phantom, which will be discussed in the following sections.

A.2.1 Theoretical Phantom Model

A homogenous or layered planar phantom model is considered as the simplest theoretical model that can be used for theoretical analysis of electromagnetic waves. They can be designed in spherical, cylindrical, etc. shapes to model human head, eye or body trunk respectively.

A.2.2 Voxel-based Phantom Model

Recently advances in medical imaging technologies such as CT, X-ray and MRI have encouraged the development of different voxel-based models. These models provide a realistic environment similar to the human body and facilitate different electromagnetic analyses and studies inside or around the human body. Table A.1 summarises some of these well-known phantoms.

Table A.1: Human Phantom Models

Reference	Technique	Name of the phantom	Sex	No. of Tissue	Resolution
[163]	MRI	NORMAN	Male	37	$2.04 \times 2.o4 \times 1.95\ mm^3$
[164]	MRI	NAOMI	Female		2 mm
[165]	MRI	-	Male & Female	51	2 mm
[166]	Transversal color photographic images	VIP-Man	Male	-	Contain of 3.7 billion voxels
[167]		Glenn	Male	304	-
		Fats	Male	V3.1 includes 305 Tissues V1.1 includes 153 Tissues	$0.5 \times 0.5 \times 0.5\ mm^3$
		Duke	Male	V3.0 includes 305 Tissues V1.3 includes 146 Tissues	
		Ella	Female	V3.0 includes 305 Tissues V1.3 includes 76 Tissues	
		Louis	14-year-old boy	V3.1 includes 306 Tissues V1.3 includes 182 Tissues	
		Billie	11-year-old girl	V3.1 includes 305 Tissues V1.3 includes 112 Tissues	
		Eartha	8-year-old girl	V3.1 includes 306 Tissues V1.3 includes 75 Tissues	
		Dizzy	8-year-old boy	V3.1 includes 306 Tissues V1.3 includes 137 Tissues	
		Thelonious	6-year-old boy	V3.1 includes 299 Tissues V1.3 includes 76 Tissues	
		Roberta	5-year-old girl	V3.1 includes 302 Tissues V1.3 includes 66 Tissues	
		Nina	3-year-old girl	V1.1 includes 61 Tissue	
		Charlie	8-week-old girl	V1.1 includes 61 Tissues	

B

SEMCAD

B.1 SEMCAD X

SEMCAD X is a full-wave 3-D electromagnetic simulation software package based on the FDTD method. It was designed and developed by Schmid & Partner Engineering (SPEAG). The software is designed to address different varieties of engineering challenges in the wireless and medical areas, EMC, dosimetry and antenna design. It is based on the ACIS modelling toolkit that makes it possible to easily import and process different CAD formats. Moreover a wide range of anatomical heterogeneous, high-resolution, posable human and animal models from the Virtual Family Project is available. One of the important features of this software is that it can be interfaced with the Hardware Accelerator using NVIDIA GPU cards. A SPEAG CUDA library is also available as an alternative for GPU hardware acceleration. These technologies significantly reduce the runtime of simulations by more than 35 times. SEMCAD X also offers three multi-view options that facilitate designing and viewing complex models with their detailed geometry.

B.2 Finite-difference Time-domain Method

The simulation in SEMCAD is based on the finite-difference time-domain (FDTD) method, which is a principal form of electromagnetic modelling. In fact it is a computational technique for solving Maxwell equations. There are several techniques such as the Method of Moments (MOM), the Finite Element Method (FEM), theory of diffraction, finite integration theory and physical optics that have been applied for the solution of electromagnetic problems. However the most popular technique is FDTD and it can be successfully applied in a wide variety of electromagnetic problems including: scattering, radiation of antennas, optical applications, guided wave propagation etc.

The theory at the basis of the FDTD method is straightforward. To solve an electromagnetic problem, one approach is to discretise the space in terms of grids and solve Maxwell's equations at each point in the grid. Hence in the FDTD method the time-dependent Maxwell's equations should be discretised using central-difference approximations in both time and space. The electric field can be solved at a given instant of time and then the magnetic field will be solved at the next instant in time, and this process can be repeated again multiple times.

To perform any FDTD computation on Maxwell's equations, first it is crucial to establish a computational domain. The computational domain can be defined as any physical region over which the simulation will be performed. In the next step the H and E fields are calculated at any point in space within that computational domain. Therefore it is necessary to define the material of each cell within the computational domain. In general, material can be defined as either metal, dielectric or free space (air). This allows a user to easily specify and model a wide variety of linear and nonlinear magnetic and electric materials. Since the FDTD method is a time-domain method, computation can also be done for a wide frequency range with just a single simulation run.

B.3 Accuracy of FDTD Method

In the FDTD method the computational domain should be divided into very small rectangular cells referred to as voxels. Then the electric and magnetic field will be calculated in every voxel using an algorithm based on Maxwell's equations.

The cell size plays an important role in the accuracy of the FDTD method. It should be chosen carefully so that over one increment the magnetic and electric field

do not change. Also the number of sampling points needs to be adequate to ensure that accurate results can be achieved even at higher frequencies. On the other hand the cell size is affected by the assumed material parameters. When the permittivity or conductivity of a material increases a shorter wavelength will exist in the material, thus a smaller cell is required. In general the accuracy of the FDTD method can be improved significantly by reducing the cell size, although employing more cells in a simulation consumes more computer memory, and solving the equations takes significant extra time.

B.4 Voxelling of the Human Phantom Model

Each voxel of an anatomical human phantom represents the composition of different tissues in phantom. Voxelized phantoms are widely applied in modelling of the human body for computations of different medical applications. One of the main advantages of the SEMCAD software is that it has a built in Graphic User Interface (GUI) that helps user to re-scale the voxel size of the human phantom. It is apparent that increasing the resolution of the model influences the accuracy of the computation results.

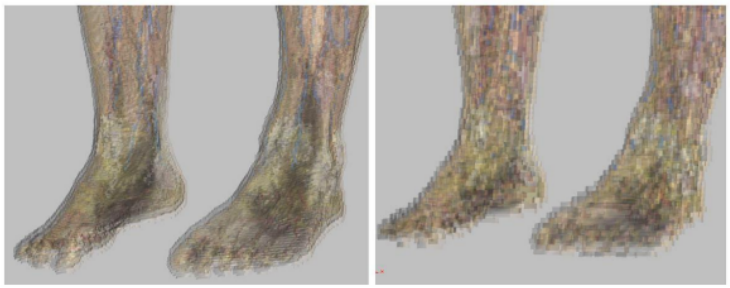

Figure B.1: Voxel size resolution variation [7]

Figure B.1 compares two different voxels used in a phantom. It can be seen that

the phantom feet appear clearly and more anatomical details are visible with 2 mm resolution than with 4mm resolution. The remarkable advantage of working with a higher-resolution phantom is that it provides a closer match to the real human body by representing more tissues and organs. On the other hand, increasing the voxel size near the surface of the body produces a larger number of voxels containing both body tissues and external air. This leads to inaccurate results. Therefore choosing an adequate resolution of the human phantom is required to improve the computation results.

List of Acronyms/Abbreviations

AOA	Angle Of Arrival
APP	Angular Power Profile
BAN	Body Area Network
CDF	Cumulative Distribution
CDP	Cumulative Distribution Probability
CIR	Channel Impulse Response
CRLB	Cramér-Rao Lower Bound
CST	Computer Simulation Technology
CT	Computed Tomography
EIRP	Effective Isotropically Radiated Power
FCC	Federal Communications Commission
FDA	Food and Drug Administration
FDTD	Finite-difference Time-domain method
FEM	Finite Element Method
FIM	Fisher Information Matrix
FIT	Finite Integral Technique
GDOP	Geometric Dilution of Precision
GI	Gastrointestinal
GUI	Graphic User Interface
HBC	Least Squares
LOS	Line Of Sight

LS	Least Squares
MICS	Medical Implant Communications Service
ML	Maximum Likelihood
MOM	Method of Moment
MRI	Magnetic Resonance Imaging
NB	Narrow Band
NIH	National Institutes of Health
NLLS	Non-linear Least Squares
NLOS	Non Line Of Sight
PDF	Probability Distribution Function
PDP	Power Delay Profile
PEC	Perfect Electric Conductor
PH	potential hydrogen
PMC	Perfect Magnetic Conductor
RCS	Radar Cross Section
RF	Radio Frequency
RSE	Recieved Signal Electricity
RSS	Received Signal Strength
RMS	Root Mean Square
SAR	Specific Absorption Rate
SNR	Signal to Noise ratio
STD	Standard Deviation
TDOA	Time Difference of Arrival
TOA	Time Of Arrival
UPML	Uniaxial Perfectly Matched Layers
UWB	Ultra-Wideband
WCE	Wireless Capsule Endoscope
WMTS	Web Map Tile Service

ICNIRP International Commission on Non-Ionizing Radiation Protection

References

[1] *Mirocam capsule endoscopy* URL http://www.medivators.com/sites/default/files/minntech/documents/MiroCam%2050098-272%20Rev%20A.pdf/. xvii, 4

[2] P. Valdastri, M. Simi, and R. Webster. *Advanced technologies for gastrointestinal endoscopy.* Annual Review Biomedical Engineering **14**, 397 (2012). xvii, 12

[3] *9 regions of abdomen* (2016). URL http://www.newhealthguide.org/9-Regions-Of-Abdomen.html. xvii, 15, 16

[4] *The small intestine* (2015). URL http://teachmeanatomy.info/abdomen/gi-tract/small-intestine. xvii, 16

[5] M. R. Yuce. *Ultra-Wideband and 60 GHz Communications for Biomedical Applications* (Springer, 2014). xvii, 71

[6] G. Alwis and M. Delahoy. *60 GHz band millimeter wave technology* (2004). URL http://www.acma.gov.au/webwr/radcomm/frequency_planning. xvii, 70, 72

[7] F. Ying. *Analysis of exposure to electromagnetic fields within the near-field of HF broadcast antennas.* PhD thesis, University of Sheffield pp. 45–83 (2013). URL http://etheses.whiterose.ac.uk/4699/. xx, 187

[8] M. Keuchel, F. Hagenmller, and H. Tajiri. *Video Capsule Endoscopy: A Reference Guide and Atlas* (Springer). xxi, 13, 14

[9] S. Movassaghi, M. Abolhasan, J. Lipman, D. Smith, and A. Jamalipour. *Wireless body area networks: A survey.* Communications Surveys Tutorials, IEEE **16**(3), 1658 (2014). xxi, 42

[10] D. S. Mishkin, R. Chuttani, J. Croffie, J. DiSario, J. Liu, R. Shah, L. Somogyi, W. Tierney, L. M. Wong Kee Song, and B. T. Petersen. *ASGE Technology Status Evaluation Report: wireless capsule endoscopy.* Gastrointestinal Endoscopy **63**(4), 539 (2006). 2

[11] C. M. Höög, L.-Å. Bark, J. Arkani, J. Gorsetman, O. Broström, and U. Sjöqvist. *Capsule retentions and incomplete capsule endoscopy examinations: an analysis of 2300 examinations.* Gastroenterology Research and Practice **2012** (2011). 2

[12] Z. Liao, R. Gao, C. Xu, and Z.-S. Li. *Indications and detection, completion, and retention rates of small-bowel capsule endoscopy: a systematic review.* Gastrointestinal Endoscopy **71**(2) (2009). 2

[13] D. Bandorski, M. Keuchel, M. Brück, R. Hoeltgen, M. Wieczorek, and R. Jakobs. *Capsule endoscopy in patients with cardiac pacemakers, implantable cardioverter defibrillators, and left heart devices: a review of the current literature.* Diagnostic and Therapeutic Endoscopy **2011** (2011). 2, 3

[14] Y. Guyomar, L. Vandeville, S. Heuls, F. Coviaux, P. Graux, P. Cornaert, and B. Filoche. *Interference between pacemaker and video capsule endoscopy.* Pacing and Clinical Electrophysiology **27**(9), 1329 (2004). URL http://dx.doi.org/10.1111/j.1540-8159.2004.00631.x. 2

[15] H. Herlinger, D. Maglinte, and B. A. Birnbaum. *Clinical Imaging of the Small Intestine* (New York: Springer-Verlag, 2001), 2nd ed. 3

[16] G. Ciuti, A. Menciassi, and P. Dario. *Capsule endoscopy: From current achievements to open challenges.* Biomedical Engineering, IEEE Reviews in **4**, 59 (2011). 12

[17] S. Bang, J. Y. Park, S. Jeong, Y. H. Kim, H. B. Shim, T. S. Kim, D. H. Lee, and S. Y. Song. *First clinical trial of the mirocapsule endoscope by using a novel transmission technology: electric-field propagation.* Gastrointestinal Endoscopy **69**(2), 253 (2015). 13

[18] *CapsoCam sv-2 the new standard in capsule endoscopy.* URL http://www.image-tech.uk.com/product/capsocam-sv2-new-standard-capsule-endoscopy/. 13

[19] M. Pennazio, C. Spada, R. Eliakim, M. Keuchel, A. May, C. J. Mulder, E. Rondonotti, S. N. Adler, J. Albert, P. Baltes, F. Barbaro, C. Cellier, J. P. Charton,

M. Delvaux, E. J. Despott, D. Domagk, A. Klein, M. McAlindon, B. Rosa, G. Rowse, D. S. Sanders, J. C. Saurin, R. Sidhu, J.-M. Dumonceau, C. Hassan, and I. M. Gralnek. *Small-bowel capsule endoscopy and device-assisted enteroscopy for diagnosis and treatment of smallbowel disorders: European Society of Gastrointestinal Endoscopy (ESGE) Clinical Guideline.* Endoscopy, **47**(04), 352 (2015). 13

[20] H. Gray. *Anatomy of the human body.* URL http://www.bartleby.com/107/248.html. 15, 17, 87, 142

[21] S. Gezici. *A survey on wireless position estimation.* Wireless Personal Communication **44**(3), 263 (2008). 17, 21, 22

[22] S. Gezici and H. V. Poor. *Position Estimation via Ultra-Wide-Band Signals.* Proceedings of the IEEE **97**(2), 386 (2009). 17, 22, 28

[23] H. Liu, H. Darabi, P. Banerjee, and J. Liu. *Survey of Wireless Indoor Positioning Techniques and Systems.* Systems, Man, and Cybernetics, Part C: Applications and Reviews, IEEE Transactions on **37**(6), 1067 (2007). 20, 22, 24

[24] P. Swar, Y. Ye, K. Ghaboosi, and K. Pahlavan. *On effect of transmit power variance on localization accuracy in wireless capsule endoscopy.* In *Wireless Communications and Networking Conference (WCNC), 2012 IEEE*, pp. 2119–2123 (2012). 22

[25] Y. Gu, A. Lo, and I. Niemegeers. *A survey of indoor positioning systems for wireless personal networks.* Communications Surveys Tutorials, IEEE **11**(1), 13 (2009). 24, 25, 28, 29, 33

[26] C. Nerguizian, C. Despins, and S. Affes. *A framework for indoor geolocation using an intelligent system* (Citeseer). 25

[27] M. Triki, D. Slock, V. Rigal, and P. Francois. *Mobile Terminal Positioning via Power Delay Profile Fingerprinting: Reproducible Validation Simulations.* In *Vehicular Technology Conference, 2006. VTC-2006 Fall. 2006 IEEE 64th*, pp. 1–5 (2006).

[28] F. Althaus, F. Troesch, and A. Wittneben. *UWB geo-regioning in rich multipath environment.* In *Vehicular Technology Conference, 2005. VTC-2005-Fall. 2005 IEEE 62nd*, vol. 2, pp. 1001–1005 (2005).

[29] C. Nerguizian, C. Despins, and S. Affes. *Geolocation in mines with an impulse response fingerprinting technique and neural networks.* Wireless Communications, IEEE Transactions on **5**(3), 603 (2006). 25

[30] M. Abdat, T. C. Wan, and S. Supramaniam. *Survey on indoor wireless positioning techniques: Towards adaptive systems.* In *Distributed Framework and Applications (DFmA), 2010 International Conference on*, pp. 1 –5 (2010). 25, 26

[31] T. W. Sudhir Dixit. *Content Networking in the Mobile Internet* (Wiley Publishing, 2004). 26

[32] T. D. Than, G. Alici, H. Zhou, and W. Li. *A Review of Localization Systems for Robotic Endoscopic Capsules.* Biomedical Engineering, IEEE Transactions on **59**(9), 2387 (2012). 29, 30

[33] V. Schlageter, P. Drljaca, R. S. Popovic, and P. Kucera. *A magnetic tracking system based on highly sensitive integrated hall sensors.* In *JSME International Journal Series C*, vol. 45, pp. 967–973 (2002). 30

[34] C. Hu, M. Q. Meng, and M. Mandal. *Efficient magnetic localization and orientation technique for capsule endoscopy.* In *Intelligent Robots and Systems, 2005. (IROS 2005). 2005 IEEE/RSJ International Conference on*, pp. 628–633 (2005).

[35] C. Hu, M. Li, S. Song, W. Yang, R. Zhang, and M.-H. Meng. *A Cubic 3-Axis Magnetic Sensor Array for Wirelessly Tracking Magnet Position and Orientation.* Sensors Journal, IEEE **10**(5), 903 (2010). 30, 37

[36] X. Wu, W. Hou, C. Peng, X. Zheng, X. Fang, and J. He. *Wearable magnetic locating and tracking system for mems medical capsule.* Sensors and Actuators A: Physical **141**(2), 432 (2008). 37

[37] S. Hashi, S. Yabukami, H. Kanetaka, K. Ishiyama, and K. I. Arai. *Numerical Study on the Improvement of Detection Accuracy for a Wireless Motion Capture System.* Magnetics, IEEE Transactions on **45**(6), 2736 (2009). 30, 37

[38] T. Shah, S. M. Aziz, and T. Vaithianathan. *Development of a Tracking Algorithm for an In-Vivo RF Capsule Prototype.* In *Electrical and Computer Engineering, 2006. ICECE '06. International Conference on*, pp. 173–176 (2006). 30, 31, 32

[39] K. Arshak and F. Adepoju. *Adaptive linearized methods for tracking a moving telemetry capsule.* In *Industrial Electronics, 2007. ISIE 2007. IEEE International Symposium on*, pp. 2703–2708 (2007). 31

[40] D. Anzai, S. Aoyama, and J. Wang. *Impact of propagation characteristics on RSSI-based localization for 400 MHz MICS band implant body area networks.* In *Medical Information and Communication Technology (ISMICT), 2012 6th International Symposium on*, pp. 1–4 (2012). 32, 37, 55, 66

[41] J. Hou, Y. Zhu, L. Zhang, Y. Fu, F. Zhao, L. Yang, and G. Rong. *Design and Implementation of a High Resolution Localization System for In-Vivo Capsule Endoscopy.* In *Dependable, Autonomic and Secure Computing, 2009. DASC '09. Eighth IEEE International Conference on*, pp. 209–214 (2009). 30

[42] U. I. Khan, K. Pahlavan, and S. Makarov. *Comparison of TOA and RSS based techniques for RF localization inside human tissue.* In *Engineering in Medicine and Biology Society, EMBC, 2011 Annual International Conference of the IEEE*, pp. 5602–5607 (2011). 31, 32, 37

[43] Y. Wang, R. Fu, Y. Ye, U. Khan, and K. Pahlavan. *Performance bounds for RF positioning of endoscopy camera capsules.* In *Biomedical Wireless Technologies, Networks, and Sensing Systems (BioWireless), 2011 IEEE Topical Conference on*, pp. 71–74 (2011). 31, 32, 37

[44] D. Fischer, R. Schreiber, D. Levi, and R. Eliakim. *Capsule endoscopy: the localization system.* In *Gastrointestinal Endoscopy of Clinics North America*, vol. 14, pp. 25–31 (2004). 32, 37

[45] H. Jacob, M. Frisch, D. Levy, A. Glukhovsky, R. Shreiber, and S. Adler. *Localization of the Given M2A ingestible capsule in the Given diagnostic imaging system.* In *The American Journal of Gastroenterology*, vol. 55 (2001). 32, 37

[46] Y. Ye, U. Khan, and K. Pahlavan. *Accuracy bounds for RSS and TOA based RF localization in capsule endoscopy.* In *Engineering in Medicine and Biology Society, EMBC, 33rd Annual International Conference of IEEE* (2011). 32

[47] H. Liu, H. Darabi, P. Bnerjee, and J. Liu. *Survey of Wireless Indoor Positioning Techniques and Systems.* In *IEEE Transactions on Systems, Man and Cybernetics*, vol. 37, pp. 1067–1080 (2007). 33

[48] L. Zhang, Y. Zhu, T. Mo, J. Hou, and H. Hu. *Design of 3D Positioning Algorithm Based on RFID Receiver Array for In Vivo Micro-robot.* In *Dependable, Autonomic and Secure Computing, 2009. DASC '09. Eighth IEEE International Conference on*, pp. 749–753 (2009). 33, 37

[49] L. Zhang, Y. Zhu, T. Mo, J. Hou, and G. Rong. *Design and Implementation of 3D Positioning Algorithms Based on RF Signal Radiation Patterns for In Vivo Micro-robot*. In *Body Sensor Networks (BSN), 2010 International Conference on*, pp. 255–260 (2010). 37

[50] J. Hou, Y. Zhu, L. Zhang, Y. Fu, F. Zhao, L. Yang, and G. Rong. *Design and Implementation of a High Resolution Localization System for In-Vivo Capsule Endoscopy*. In *Dependable, Autonomic and Secure Computing, 2009. DASC '09. Eighth IEEE International Conference on*, pp. 209–214 (2009). 33, 37

[51] C. S. Wang and C. Chen. *Flexible Localization and Identification System Based on RFID and Vision Tracking Technologies*. In *International Symposium on Computer Science and Society*, vol. 37, pp. 356–360 (2011). 33

[52] K. Duda, T. Zielinski, R. Fraczek, J. Bulat, and M. Duplaga. *Localization of endoscopic capsule in the GI tract based on MPEG-7 visual descriptors*. In *Imaging Systems and Techniques, 2007. IST '07. IEEE International Workshop on*, pp. 1–4 (2007). 33, 37

[53] J. Bulat, K. Duda, M. Duplaga, R. Fraczek, A. Skalski, M. Socha, P. Turcza, and T. Zielinski. *Data processing tasks in wireless GI endoscopy: Image-based capsule localization and navigation and video compression*. In *Engineering in Medicine and Biology Society, 2007. EMBS 2007. 29th Annual International Conference of the IEEE*, pp. 2815–2818 (2007). 33

[54] J. Lee, J. Oh, S. K. Shah, X. Yuan, and S. J. Tang. *Automatic classification of digestive organs in wireless capsule endoscopy videos*. In *Proceedings of the 2007 ACM Symposium on Applied Computing*, SAC '07, pp. 1041–1045 (ACM, 2007). URL http://doi.acm.org/10.1145/1244002.1244230. 33, 37

[55] F. Carpi, N. Kastelein, M. Talcott, and C. Pappone. *Magnetically controllable gastrointestinal steering of video capsules*. Biomedical Engineering, IEEE Transactions on **58**(2), 231 (2011). 34, 37

[56] R. Kuth, J. Reinschke, and R. Rockelein. *Method for determining the position and orientation of an endoscopy capsule guided through an examination object by using a navigating magnetic field generated by means of a navigation device* (2007). US Patent App. 11/481,935, URL https://www.google.ch/patents/US20070038063. 34

[57] S. S. Davis, J. G. Hardy, S. P. Newman, and I. R. Wilding. *Gamma scintigraphy in the evaluation of pharmaceutical dosage forms.* European Journal of Nuclear Medicine **19**, 971 (1992). 34

[58] I. Wilding, P. Hirst, and A. Connor. *Development of a new engineering-based capsule for human drug absorption studies.* Pharmaceutical Science and Technology Today **19**, 385 (2000). 34, 37

[59] K. Arshak and F. Adepoju. *Capsule tracking in the GI tract: a novel microcontroller based solution.* In *Sensors Applications Symposium, 2006. Proceedings of the 2006 IEEE*, pp. 186–191 (2006). 35

[60] M. Fluckiger and B. Nelson. *Ultrasound emitter localization in heterogeneous media.* In *Engineering in Medicine and Biology Society, 2007. EMBS 2007. 29th Annual International Conference of the IEEE*, pp. 2867–2870 (2007). 35, 37

[61] Z. Nagy, M. Fluckiger, O. Ergeneman, S. Pane, M. Probst, and B. Nelson. *A wireless acoustic emitter for passive localization in liquids.* In *Robotics and Automation, 2009. ICRA '09. IEEE International Conference on*, pp. 2593–2598 (2009). 35, 37

[62] I. K. K. Bradley J. Nelson and J. J. Abbott. *Microrobots for minimally invasive medicine.* In *Annual Review of Biomedical Engineering*, vol. 12, pp. 55–85 (2010). 35

[63] C. L. Dumoulin, S. P. Souza, and R. D. Darrow. *Real-time position monitoring of invasive devices using magnetic resonance.* Magnetic Resonance in Medicine **29**, 411 (1993). 35, 37

[64] A. Krieger, R. Susil, C. Menard, J. Coleman, G. Fichtinger, E. Atalar, and L. Whitcomb. *Design of a novel MRI compatible manipulator for image guided prostate interventions.* Biomedical Engineering, IEEE Transactions on **52**(2), 306 (2005). 35, 37

[65] X. Li, E. Pancera, L. Niestoruk, W. Stork, and T. Zwick. *Performance of an ultra wideband radar for detection of water accumulation in the human bladder.* In *Radar Conference (EuRAD), 2010 European*, pp. 212–215 (2010). 36

[66] J. Sill and E. Fear. *Tissue sensing adaptive for breast cancer detection - experimental investigation of simple tumor models.* Microwave Theory and Techniques, IEEE Transactions on **53**(11), 3312 (2005).

[67] M. Jalilvand, X. Li, and T. Zwick. *A model approach to the analytical analysis of stroke detection using UWB radar.* In *Antennas and Propagation (EuCAP), 2013 7th European Conference on*, pp. 1555–1559 (2013). 36

[68] G. Curry. *Radar System Performance Modeling, Second Edition* (Artech House Publishers, 2004), second ed. 36, 39, 80

[69] *Radar cross-section.* URL http://en.wikipedia.org/wiki/Radar-cross-section. 39

[70] J. A. Richards. *Radio Wave Propagation An Introduction for the Non-Specialist* (Springer, 2008). 39, 101

[71] C. Liolios, C. Doukas, G. Fourlas, and I. Maglogiannis. *An overview of body sensor networks in enabling pervasive healthcare and assistive environments.* Proceedings of the 3rd International Conference on Pervasive Technologies Related to Assistive Environments pp. 43:1–43:10 (2010). 43

[72] *In the matter of revision of part 15 of the commissions rules regarding ultra-wideband transmission systems.* FCC02-48, Federal Communications Commission (FCC) (2002). 43, 44

[73] H. Xu and L. Yang. *Ultra-wideband technology: Yesterday, today, and tomorrow.* IEEE Radio and Wireless Symposium pp. 715 –718 (2008). 43, 44

[74] J. D. Taylor. *Ultrawideband Radar: Applications and Design* (CRC Press, 2012). 44

[75] S. Mukhopadhyay and A. Lay-Ekuakille. *Advances in Biomedical Sensing, Measurements, Instrumentation and Systems.* Lecture Notes in Electrical Engineering (Springer, 2010). 44

[76] ICNIRP. *Guidelines for limiting exposure to time-varying electric, magnetic, and electromagnetic fields (up to 300GHz).* Health Physics **74**(4), 494 (1998). 44

[77] M. Cavagnaro, S. Pisa, and E. Pittella. *Safety aspects of people exposed to ultra wideband radar fields.* International Journal of Antennas and Propagation (2013). 44

[78] A. Boulis, D. Smith, D. Miniutti, L. Libman, and Y. Tselishchev. *Challenges in Body Area Networks for Healthcare: The MAC.* IEEE Communications Magazine (May) (2012). 44

[79] W. Scanlon, B. Burns, and N. Evans. *Radiowave propagation from a tissue-implanted source at 418 MHz and 916.5 MHz.* Biomedical Engineering, IEEE Transactions on **47**(4), 527 (2000). 48, 116

[80] A. Khaleghi and I. Balasingham. *On the ultra wideband propagation channel characterizations of the biomedical implants.* In *Vehicular Technology Conference, 2009. VTC Spring 2009. IEEE 69th* (2009). 48

[81] D. Kurup, W. Joseph, G. Vermeeren, and L. Martens. *In-body path loss model for homogeneous human muscle, brain, fat and skin.* In *Antennas and Propagation (EuCAP), 2010 Proceedings of the Fourth European Conference on*, pp. 1–4 (2010). 48, 116

[82] D. Kurup, W. Joseph, G. Vermeeren, and L. Martens. *Path loss model for in-body communication in homogeneous human muscle tissue.* Electronics Letters **45**(9), 453 (2009). 48

[83] D. Kurup, G. Vermeeren, E. Tanghe, W. Joseph, and L. Martens. *In-to-out body antenna-independent path loss model for multilayered tissues and heterogeneous medium.* Sensors **15**(1), 408 (2014). 48

[84] D. Kurup, W. Joseph, G. Vermeeren, and L. Martens. *Specific absorption rate and path loss in specific body location in heterogeneous human model.* IET Microwaves, Antennas & Propagation **7**(1), 35 (2013). 48

[85] P. Stavroulakis. *Third Generation Mobile Telecommunication Systems:UMTS and IMT-2000* (Springer Science and Business Media, 2012). 49, 55, 60

[86] K. Sayrafian-Pour, W.-B. Yang, J. Hagedorn, J. Terrill, and K. Yazdandoost. *A statistical path loss model for medical implant communication channels.* In *Personal, Indoor and Mobile Radio Communications, 2009 IEEE 20th International Symposium on*, pp. 2995–2999 (2009). 49, 50, 66, 104, 116

[87] D. Kurup, M. Scarpello, G. Vermeeren, W. Joseph, K. Dhaenens, F. Axisa, L. Martens, D. Vande Ginste, H. Rogier, and J. Vanfleteren. *In-body path loss models for implants in heterogeneous human tissues using implantable slot dipole conformal flexible antennas.* EURASIP Journal on Wireless Communications and Networking **2011**, 1 (2011). URL http://dx.doi.org/10.1186/1687-1499-2011-51. 50, 51, 66, 116

[88] T. Aoyagi, K. Takizawa, T. Kobayashi, J.-i. Takada, and R. Kohno. *Development of a WBAN channel model for capsule endoscopy.* In *Antennas and Propagation Society International Symposium, 2009. APSURSI '09. IEEE*, pp. 1–4 (2009). 51, 66

[89] S. Stoa, R. Chavez-Santiago, and I. Balasingham. *An ultra wideband communication channel model for capsule endoscopy.* In *Applied Sciences in Biomedical and Communication Technologies (ISABEL), 2010 3rd International Symposium on*, pp. 1 –5 (2010). 52, 54, 66, 116

[90] Y. Liu and R. D. Gitlin. *A phenomenological path loss model of the in vivo wireless channel.* In *IEEE 16th Wireless and Microwave Technology Conference (WAMICON), 2015 IEEE* (2015). 54, 60, 66

[91] L. Wang, C. Hu, L. Tian, M. Li, and M.-H. Meng. *A novel radio propagation radiation model for location of the capsule in GI tract.* In *Robotics and Biomimetics (ROBIO), 2009 IEEE International Conference on*, pp. 2332 –2337 (2009). 56, 66

[92] L. Wang, L. Liu, C. Hu, and M.-H. Meng. *A novel RF-based propagation model with tissue absorption for location of the GI tract.* In *Engineering in Medicine and Biology Society (EMBC), 2010 Annual International Conference of the IEEE*, pp. 654–657 (2010). 57, 66

[93] M. Ramezani, V. Blanes-Vidal, and E. S. Nadimi. *An adaptive path loss channel model for wave propagation in multilayer transmission medium.* Progress in Electromagnetics Research (P I E R) **150**, 1 (2015). 59, 66

[94] Y. Liu, T. Ketterl, G. Arrobo, and R. Gitlin. *Modeling the wireless in vivo path loss.* In *RF and Wireless Technologies for Biomedical and Healthcare Applications (IMWS-Bio), 2014 IEEE MTT-S International Microwave Workshop Series on*, pp. 1–3 (2014). 59, 66

[95] X. Chu, D. Lpez-Prez, Y. Yang, and F. Gunnarsson. *Heterogeneous Cellular Networks: Theory, Simulation and Deployment* (Cambridge University Press, 2013). 60

[96] K. Takizawa, H. Hagiwara, and K. Hamaguchi. *Path-loss estimation of wireless channels in capsule endoscopy from X-ray CT images.* In *Engineering in Medicine*

and Biology Society, EMBC, 2011 Annual International Conference of the IEEE, pp. 2242–2245 (2011). 61, 66, 104

[97] K.-L. Roman, G. Vermeeren, A. Thielens, W. Joseph, and L. Martens. *Characterization of path loss and absorption for a wireless radio frequency link between an in-body endoscopy capsule and a receiver outside the body.* EURASIP Journal on Wireless Communications and Networking **2014**(1), 1 (2014). 62, 66

[98] E. Reusens, W. Joseph, B. Latré, B. Braem, G. Vermeeren, E. Tanghe, L. Martens, I. Moerman, and C. Blondia. *Characterization of on-body communication channel and energy efficient topology design for wireless body area networks.* Information Technology in Biomedicine, IEEE Transactions on **13**(6), 933 (2009). 63

[99] A. Alomainy and Y. Hao. *Modeling and characterization of biotelemetric radio channel from ingested implants considering organ contents.* Antennas and Propagation, IEEE Transactions on **57**(4), 999 (2009). 63, 66

[100] *Report of the unlicensed devices and experimental licenses working group* (2002). URL http://www.fcc.gov/sptf/files. 71

[101] G. Valerio, N. Chahat, M. Zhadobov, and R. Sauleau. *Theoretical and experimental characterization of on-body propagation at 60 GHz.* In *Antennas and Propagation (EuCAP), 2013 7th European Conference on*, pp. 583–585 (2013). 71

[102] N. Chahat, M. Zhadobov, L. Le Coq, S. Alekseev, and R. Sauleau. *Characterization of the interactions between a 60-GHz antenna and the human body in an off-body scenario.* Antennas and Propagation, IEEE Transactions on **60**(12), 5958 (2012). 71

[103] Y. Nechayev, X. Wu, C. Constantinou, and P. Hall. *Effect of body motion on propagation path gain at 60 GHz.* In *Antennas and Propagation (EUCAP), 2012 6th European Conference on*, pp. 3397–3401 (2012). 71

[104] Y. Nechayev, C. Constantinou, S. Swaisaenyakorn, O. Rakibet, J. Batchelor, P. Hall, C. Parini, and J. Hunt. *Use of motion capture for path gain modelling of millimetre-wave on-body communication links.* In *Antennas and Propagation (ISAP), 2012 International Symposium on*, pp. 987–990 (2012). 71

[105] X. Y. Wu, Y. Nechayev, and P. S. Hall. *Antenna design and channel measurements for on-body communications at 60 GHz*. In *General Assembly and Scientific Symposium, 2011 XXXth URSI*, pp. 1–4 (2011). 71

[106] T. Mavridis, L. Petrillo, J. Sarrazin, D. Lautru, A. Benlarbi-Delai, and P. De Doncker. *Theoretical and experimental investigation of a 60-GHz off-body propagation model*. Antennas and Propagation, IEEE Transactions on **62**(1), 393 (2014). 71

[107] L. Petrillo, T. Mavridis, J. Sarrazin, D. Lautru, A. Benlarbi-Delai, and P. De Doncker. *Analytical creeping wave model and measurements for 60 GHz body area networks*. Antennas and Propagation, IEEE Transactions on **62**(8), 4352 (2014). 71

[108] N. Chahat, M. Zhadobov, S. Alekseev, and R. Sauleau. *Human skin-equivalent phantom for on-body antenna measurements in 60 GHz band*. Electronics Letters **48**(2), 67 (2012). 72

[109] S. K. Kim, H. J. Kim, K. Y. Hur, S. H. Choi, C. W. Ahn, S. K. Lim, K. R. Kim, H. C. Lee, K. B. Huh, and B. S. Cha. *Visceral fat thickness measured by ultrasonography can estimate not only visceral obesity but also risks of cardiovascular and metabolic diseases*. The American Journal of Clinical Nutrition **79**(4), 593 (2004). 74

[110] C. W. Kim and T. S. P. See. *RF transmission power loss variation with abdominal tissues thicknesses for ingestible source*. In *e-Health Networking Applications and Services (Healthcom), 2011 13th IEEE International Conference on*, pp. 282 –287 (2011).

[111] Y. Lee and K. Hwang. *Skin thickness of Korean adults*. Surgical and Radiologic Anatomy **24**, 183 (2002).

[112] H. Kanehisa, M. Miyatani, K. Azuma, S. Kuno, and T. Fukunaga. *Influences of age and sex on abdominal muscle and subcutaneous fat thickness*. European Journal of Applied Physiology **91**, 534 (2004). 74

[113] *Dielectric properties of body tissue* (2012). URL http://niremf.ifac.cnr.it/tissprop/. 74, 75, 107

[114] *Sirfloc client*. URL http://www.csr.com/products/28/sirfloc-client. 79

[115] J. Zhang, B. Li, A. G. Dempster, and C. Rizos. *Evaluation of high sensitivity GPS receivers*. URL http://mycoordinates.org/evaluation-of-high-sensitivity-gps-receivers/all/1. 79

[116] A. Arriola, J. Sancho, S. Brebels, M. Gonzalez, and W. De Raedt. *Stretchable dipole antenna for body area networks at 2.45 GHz*. Microwaves, Antennas Propagation, IET **5**(7), 852 (2011). 84

[117] J. Kim and Y. Rahmat-Samii. *Implanted antennas inside a human body: simulations, designs, and characterizations*. Microwave Theory and Techniques, IEEE Transactions on **52**(8), 1934 (2004). 84

[118] K. Y. Yazdandoost and R. Kohno. *13th International Conference on Biomedical Engineering: ICBME 2008 3–6 December 2008 Singapore*, chap. Health Care and Medical Implanted Communications Service, pp. 1158–1161 (Springer Berlin Heidelberg, Berlin, Heidelberg, 2009). URL http://dx.doi.org/10.1007/978-3-540-92841-6_284. 84

[119] K. Y. Yazdandoost and K. sayrafian Pour. *Channel model for Body Area Network (BAN)*. Networks p. 91 (2009). 84

[120] R. Salvado, C. Loss, R. Gonalves, and P. Pinho. *Textile materials for the design of wearable antennas: A survey*. Sensors **12**(11), 15841 (2012). 85

[121] K. L. Wong. *Planar Antennas for Wireless Communications* (Wiley, 2003), illustrated ed. 90

[122] C. A. Balanis. *Antenna Theory: Analysis Design* (John Wiley and Sons, Inc, 2005), third ed. 96, 102

[123] C. A. Balanis. *Engineering Electromagnetics* (Wiley, 1989), first ed. 101

[124] C. G. Christodoulou and P. F. Vahid. *Fundamental of Antennas: Concepts and Applications* (Spie Press, 2001). 102

[125] Y. Houang and K. Boyle. *Antennas: From Theory to Practice* (John Wiley and Sons, Inc., 2008), first ed. 103

[126] *IEEE standard for definitions of terms for antennas*. IEEE Std 145-2013 (Revision of IEEE Std 145-1993) pp. 1–50 (2014). 103

[127] K. Slattery and H. Skinner. *Platform Interference in Wireless Systems Models, Measurement, and Mitigation* (Elsevier Inc., 2008). 103

[128] J. I. Agbinya. *Principles of Inductive Near Field Communications for Internet of Things* (River Publishers, 2011). 103

[129] D. D. Coleman and D. A.Westcott. *CWNA Certified Wireless Network Administrator Official Deluxe Study Guide: Exam CWNA-106* (John Wiley and Sons, Inc., 2015). 104

[130] C. J. Weisman. *The Essential Guide to RF and Wireless* (Pearson Education, 2002), second ed. 104

[131] B. Moussakhani, J. Flam, S. Sta, I. Balasingham, and T. Ramstad. *On localisation accuracy inside the human abdomen region.* Wireless Sensor Systems, IET **2**(1), 9 (2012). 104

[132] C. R. Paul and S. A. Nasar. *Introduction to electromagnetic fields* (McGraw-Hill, 1982), second ed. 105

[133] T. Nagaoka, S. Watanabe, K. Sakurai, E. Kunieda, S. Watanabe, M. Taki, and Y. Yamanaka. *Development of realistic high-resolution whole-body voxel models of japanese adult males and females of average height and weight, and application of models to radio-frequency electromagnetic-field dosimetry.* Physics in Medicine and Biology **49**(1) (2004). 115

[134] T. Nagaoka, E. Kunieda, and S. Watanabe. *Proportion-corrected scaled voxel models for japanese children and their application to the numerical dosimetry of specific absorption rate for frequencies from 30 MHz to 3 GHz.* Physics in Medicine and Biology **53**(23), 6695 (2008).

[135] T. Nagaoka, T. Togashi, K. Saito, M. Takahashi, K. Ito, and S. Watanabe. *An anatomically realistic whole-body pregnant-woman model and specific absorption rates for pregnant-woman exposure to electromagnetic plane waves from 10 MHz to 2 GHz.* Physics in Medicine and Biology **52**(22), 6731 (2007).

[136] T. Nagaoka, K. Saito, M. Takahashi, K. Ito, and S. Watanabe. *Anatomically realistic reference models of pregnant women for gestation ages of 13, 18, and 26 weeks.* In *Engineering in Medicine and Biology Society, 2008. EMBS 2008. 30th Annual International Conference of the IEEE*, pp. 2817–2820 (2008).

[137] A. Christ, W. Kainz, E. G. Hahn, K. Honegger, M. Zefferer, E. Neufeld, W. Rascher, R. Janka, W. Bautz, J. Chen, B. Kiefer, P. Schmitt, H.-P. Hollenbach, J. Shen, M. Oberle, D. Szczerba, A. Kam, J. W. Guag, and N. Kuster. *The Virtual Family-development of surface-based anatomical models of two adults and two children for dosimetric simulations.* Physics in Medicine and Biology **55** (2010). 115, 117, 133

[138] Schmid and Partner Engineering AG. *Semcad Reference Guide* (2012). 120

[139] *Body Mass Index*. URL http://www.cdc.gov/healthyweight/assessing/bmi/Index.htm. 140

[140] L. A. Ferrera. *Focus on Body Mass Index and Health Research* (Nova Science Publishers, Inc, 2006). 140

[141] B. Zhen, K. Takizawa, T. Aoyagi, and R. Kohno. *A body surface coordinator for implanted biosensor networks.* In *Communications, 2009. ICC '09. IEEE International Conference on*, pp. 1–5 (2009). 141

[142] S. A. Newfield, M. D. Hinz, and D. Scott-Tilley. *Cox's Clinical Application of Nursing Diagnosis: Adult, Child, Women's, Mental Health, Gerontic, and Home Health Consideration* (F. A. Davis Company, 2007), fifth ed. 141

[143] P. Ara, M. Heimlich, and E. Dutkiewicz. *Investigation of radar approach for localization of gastro intestinal endoscopic capsule.* In *Wireless Communications and Networking Conference, 2014. WCNC 2014. IEEE* (2014). 147

[144] D. H. Staelin, A. W. Morgenthaler, and J. A. Kong. *Electromagnetic Waves* (Upper Saddle River, NJ: Prentice Hall, 1993), first ed. 147

[145] K. Yu, I. Sharp, and Y. Guo. *Ground-Based Wireless Positioning* (Wiley-IEEE Press, 2009). 156

[146] S. Kay. *Fundamentals of Statistical Signal Processing: Estimation Theory*, vol. 1 (Prentice Hall PTR, 1993). 157

[147] S. Stoa, R. Chavez-Santiago, and I. Balasingham. *An ultra wideband communication channel model for the human abdominal region.* In *GLOBECOM Workshops (GC Wkshps), 2010 IEEE*, pp. 246–250 (2010). 161

[148] J. H. Lee and R. M. Buehrer. *Location estimation using differential RSS with spatially correlated shadowing.* In *Global Telecommunications Conference, 2009. GLOBECOM 2009. IEEE*, pp. 1–6 (2009). 164

[149] F. R. P. Cavalcanti and S. Andersson. *Optimizing Wireless Communication Systems* (Springer, 2009). 164

[150] R. Vaghefi and R. Buehrer. *Received signal strength-based sensor localization in spatially correlated shadowing.* In *Acoustics, Speech and Signal Processing (ICASSP), 2013 IEEE International Conference on*, pp. 4076–4080 (2013). 166

[151] B. Clerckx and C. Oestges. *MIMO Wireless Networks* (Academic Press Elsevier, 2013), 2nd ed. 166

[152] M. Gudmundson. *Correlation model for shadow fading in mobile radio systems.* Electronics Letters **27**, 2145 (1991). 166

[153] Z. Wang, E. Tameh, and A. Nix. *Simulating correlated shadowing in mobile multihop relay/ad-hoc networks* (2006). IEEE 802.16 Broadband Wireless Access Working Group. 166

[154] P. Agrawal and N. Patwari. *Correlated link shadow fading in multi-hop wireless networks.* Wireless Communications, IEEE Transactions on **8**, 4024 (2009). 166

[155] E. K. Tameh and A. Nix. *Project IEEE 802.16 broadband wireless access working group: Simulating correlated shadowing in mobile multihop relay/ad-hoc networks* (2006). 166

[156] D. M. Sears, A. Avots-Avotins, K. Culp, and M. W. Gavin. *Frequency and clinical outcome of capsule retention during capsule endoscopy for GI bleeding of obscure origin.* Gastrointestinal Endoscopy **60**(5), 822 (2004). 171

[157] A. W. Guy. *Analyses of electromagnetic fields induced in biological tissues by thermographic studies on equivalent phantom models.* IEEE Transactions on Microwave Theory and Techniques **19**(2), 205 (1971). 182

[158] P. S. Hall and Y. Hao. *Antennas and Propagation for Body-Centric Wireless Communications, Second Edition* (Artech House, Inc. Norwood, MA, USA, 2012), 2nd ed. 182

[159] K. Ito and etal. *Development and charachteristics of a biological tissue-equivalent phantom for microwaves.* Electronics and Communications in Japan (Part I: Communications) **84**(4), 67 (2001). 182

[160] Y. Nikawa, M. Chino, and K. Kikuchi. *Soft and dry phantom modeling material using silicone rubber with carbon fiber.* IEEE Transactions on Microwave Theory and Techniques **44**(10), 1949 (1996). 182

[161] H. Tamura, Y. Ishikawa, T. Kobayashi, and T. Nojima. *A dry phantom material composed of ceramic and graphite powder.* IEEE Transactions on Electromagnetic Compatibility **39**(2), 132 (1997). 182

[162] J. T. Chang, M. W. Fanning, P. M. Meaney, and K. D. Paulsen. *A conductive plastic for simulating biological tissue at microwave frequencies.* IEEE Transactions on Electromagnetic Compatibility **42**(1), 76 (2000). 182

[163] P. Dimbylow. *The development of realistic voxel phantoms for electromagnetic field dosimetry.* in Proceedings of the Workshop on Voxel Phantom Development, Chilton, United Kingdom pp. 1–7 (1996). 184

[164] P. Dimbylow. *Development of the female voxel phantom, naomi, and its application to calculations of induced current densities and electric fields from applied low frequency magnetic and electric fields.* Physics in Medicine and Biology **50**(6), 1047 (2005). URL http://stacks.iop.org/0031-9155/50/i=6/a=002. 184

[165] T. Nagaoka, S. Watanabe, K. Sakurai, E. Kunieda, S. Watanabe, M. Taki, and Y. Yamanaka. *Development of realistic high-resolution whole-body voxel models of Japanese adult males and females of average height and weight, and application of models to radio-frequency electromagnetic-field dosimetry.* Physics in Medicine and Biology **49**(1), 1 (2004). URL http://stacks.iop.org/0031-9155/49/i=1/a=001. 184

[166] T. Xu, X.G. and A. Bozkurt. *Vip-man: An image-based whole-body adult male model constructed from color photographs of the visible human project for multi-particle monte carlo calculations.* Health Phys., **78**, 476 (2000). 184

[167] M. C. Gosselin, E. Neufeld, H. Moser, E. Huber, S. Farcito, L. Gerber, M. Jedenso, I. Hilber, F. D. Gennaro, B. Lloyd, E. Cherubini, D. Szczerba, W. Kainz, and N. Kuster. *Development of a new generation of high-resolution anatomical models for medical device evaluation: the virtual population 3.0.* Physics

in Medicine and Biology **59**(18), 5287 (2014). URL http://stacks.iop.org/0031-9155/59/i=18/a=5287. 184